Targeting a Mars science orbit from Earth

using Dual Chemical-Electric Propulsion and Ballistic Capture

Jose Angel Gutierrez Ahumada

Delft University of Technology

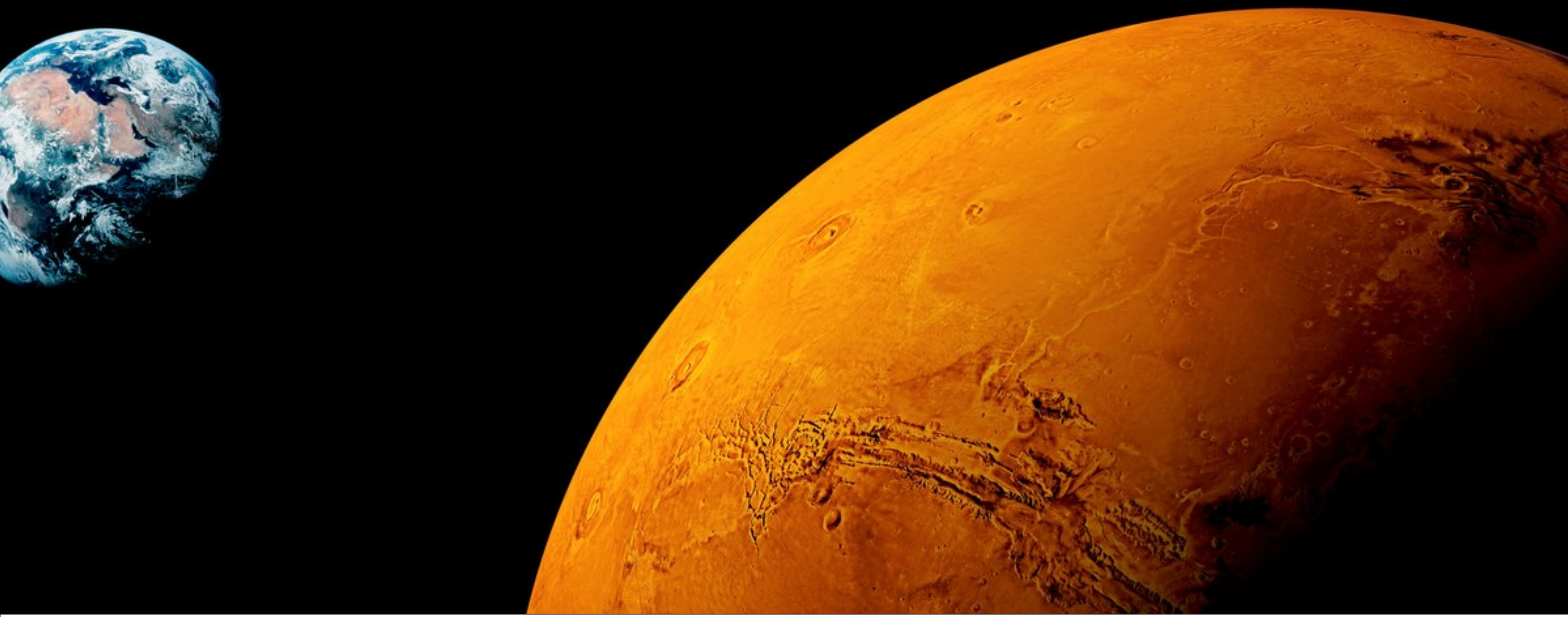

TU Delft Delft University of Technology

Challenge the future

TARGETING A MARS SCIENCE ORBIT FROM EARTH

USING DUAL CHEMICAL-ELECTRIC PROPULSION AND BALLISTIC CAPTURE

by

Jose Angel Gutierrez Ahumada

MSc Thesis

in partial fulfillment of the requirements for the degree of

Master of Science

in Aerospace Engineering

at the Delft University of Technology,

to be defended publicly on Wednesday May 8, 2019.

Supervisor:	Dr. Francesco Topputo,	TU Delft/Politecnico di Milano
	Dr. Ryan Russell,	The University of Texas at Austin
Thesis committee:	Dr. Francesco Topputo,	TU Delft/Politecnico di Milano
	Prof. dr. ir. Pieter N.A.M. Visser,	TU Delft
	ir. Ron Noomen,	TU Delft
	Dr. Angelo Cervone,	TU Delft

This thesis is confidential and cannot be made public until December 31, 2020.

An electronic version of this thesis is available at `http://repository.tudelft.nl/`.

Cover picture adapted from https://steemitimages.com/p/2gs...QbQvi

EXECUTIVE SUMMARY

Ballistic capture is a relatively novel concept in interplanetary mission design with the potential to make Mars and other targets in the Solar System more accessible. A complete end-to-end interplanetary mission from an Earth-bound orbit to a stable science orbit around Mars (in this case, an areostationary orbit) has been conducted using this concept.

Sets of initial conditions leading to ballistic capture are generated for different epochs. The influence of the dynamical model on the capture is also explored briefly. Specific capture trajectories are then selected based on a study of their stabilization into an areostationary orbit. This stabilization uses a combination of a brief high-thrust maneuver at periapsis and a low-thrust control law that spirals down to the final orbit.

The captures selected are then targeted from the sphere of influence of the Earth with a low-thrust heliocentric transfer that is optimized using direct transcription and non-linear programming theory. An arrival-departure date grid is constructed with fuel-optimal transfers obtained for all epochs considered.

Finally, a simple study of the escape from Earth is performed for completion. A strategy to quickly escape Earth and avoid radiation damage in the Van Allen belts is defined using high-thrust chemical propulsion, including the computation of gravity losses due to the use of finite burn maneuvers.

The result is the preliminary mission design of a mission concept to Mars using a 16-Unit CubeSat that employs ballistic capture and dual chemical-electric propulsion to reach an areostationary orbit. Estimations of the time of flight and fuel consumption for each stage of the mission are obtained.

PREFACE

This document is the result of the work carried out by Jose Angel Gutierrez Ahumada and supported by the University of Texas at Austin and TU Delft. The supervision of Dr. Ryan Russell and Dr. Francesco Topputo has been inestimable and has made this work possible. I would like to thank them for their patience and support.

Jose Angel Gutierrez Ahumada
Delft, April 2019

CONTENTS

Executive Summary iii

Preface v

Table of Contents ix

List of Figures xi

List of Tables xiii

List of Symbols xv

List of Abbreviations xix

I Introduction 1

1 Introduction 3
- 1.1 Context . . . 3
- 1.2 Objective . . . 4
- 1.3 Structure . . . 5

II Theoretical Background 7

2 Theoretical Background 9
- 2.1 Introduction . . . 9
- 2.2 Ballistic Capture . . . 9
- 2.3 Low-thrust Optimization . . . 15
- 2.4 High-thrust Propulsion . . . 17

III Ballistic Capture 21

3 Methodology 23
- 3.1 Introduction . . . 23
- 3.2 Problem Statement . . . 23
- 3.3 Reference Frames . . . 24
- 3.4 Spacecraft Dynamics and Equations of Motion . . . 25
- 3.5 Classification Algorithm . . . 27
- 3.6 Computational Implementation . . . 29

4 Verification and Results 31
- 4.1 Introduction . . . 31
- 4.2 Verification . . . 31
- 4.3 Influence of the Dynamics in the Capture Sets . . . 32

4.4 Capture Sets to Target 34

IV Escape from Earth **47**

5 Methodology **49**
5.1 Introduction 49
5.2 Problem Statement 49
5.3 Reference Frames 50
5.4 Spacecraft Dynamics and Equations of Motion 50
5.5 Escape Strategy 50
5.6 Computational Implementation 51

6 Results **53**
6.1 Introduction 53
6.2 Effect of the Burn Time 53
6.3 Parametric Study 57

V Stabilization around Mars **59**

7 Methodology **61**
7.1 Introduction 61
7.2 Problem Statement 61
7.3 Reference Frames 62
7.4 Spacecraft Dynamics and Equations of Motion 62
7.5 Low-Thrust Control Laws 63
7.6 Computational Implementation 66

8 Verification and Results **67**
8.1 Introduction 67
8.2 Verification 67
8.3 Control Laws 67
8.4 Effect of the Dynamics 71
8.5 Parametric Study 74
8.6 Stabilization of the Capture Sets 79

VI Heliocentric Low-Thrust Transfer **87**

9 Methodology **89**
9.1 Introduction 89
9.2 Problem Statement 89
9.3 Reference Frames 90
9.4 Spacecraft Dynamics and Equations of Motion 90
9.5 Constraints and Performance Index of the Optimal Control Problem 92
9.6 Transcribed NLP Problem 93
9.7 Computational Implementation 94

10 Verification and Results **95**
10.1 Introduction 95

10.2 Verification 95
10.3 Targeting the Captures at Mars 96
10.4 Real Solar System Dynamics 100
10.5 Effect of the Hyperbolic Excess Velocity at Earth 100

VII Conclusions and Recommendations **103**

11 Conclusions and Recommendations **105**
11.1 Conclusions. 105
11.2 Recommendations 107

Bibliography **109**

LIST OF FIGURES

1.1 Summary of the computational tools used in the different stages of the mission. 6

2.1 Variation of the capture ratio and stability index for i_0 and Ω_0 at Mars. 11
2.2 Capture set $\mathscr{C}^6_{-1}$ at Mercury. 12
2.3 Planetary true anomalies for max. capture ratio and min. stability index. 12
2.4 Position error between the ERTBP and the ephemeris model for a capture. 13
2.5 Capture sets at Mars with point mass gravity and NSG up to degree $n = 2$. 14
2.6 Capture sets at Mars with and without a SRP cannonball model. 14
2.7 Geometry of the ascent trajectory, coasting phase and escape hyperbola. 18

3.1 MARIO structure and configuration in its orbit around Mars. 24
3.2 Geometry of the EME2000 and RTN@Epoch reference frames. 25
3.3 Geometry of the intersection plane used to define three-dimensional captures. 28

4.1 Trajectory of the capture set with min. stability index in the verification set. 32
4.2 Capture sets at Mars for the different dynamical models. 34
4.3 Trajectory of the capture with lowest stability index for the different models. 35
4.4 Orientation of the equatorial and ecliptic planes, and definition of i_0 and Ω_0. 36
4.5 Longitude of the ascending node and inclination of an areostationary orbit. 36
4.6 Capture set and orbit with minimum stability index for epoch 08/May/2024. 38
4.7 Capture sets at Mars for the remaining epochs (I). 39
4.8 Capture sets at Mars for the remaining epochs (II). 40
4.9 Capture with minimum stability index for the remaining epochs (I). 41
4.10 Capture with minimum stability index for the remaining epochs (II). 42
4.11 Evolution of capture set characteristics for the different epochs. 44
4.12 Periapsis location and backwards propagation of captures from L_1 and L_2. 45
4.13 Position at different epochs of backwards propagation of the captures of a set. 45

6.1 Effect of burn time and thrust on the escape using mono-propellant. 54
6.2 Effect of burn time and thrust on the escape using bi-propellant. 55
6.3 Orbits with minimum TOF for the escape from Earth with both engines. 55
6.4 Effect of burn time on the characteristics of escape using mono-propellant. 56
6.5 Effect of burn time on the characteristics of escape using bi-propellant. 56
6.6 Parametric study of escape for variations of initial perigee altitude. 57
6.7 Parametric study of escape for variations of initial apogee altitude. 58
6.8 Parametric study of escape for variations of initial spacecraft mass. 58

8.1 Position error in the orbit propagation with *AREO* w.r.t. GRATIS. 68
8.2 Trajectory of the nominal capture used to study its stabilization. 69
8.3 Stabilized trajectory using control law 1. 70

8.4 Stabilized trajectory using control law 2. 71
8.5 Stabilized trajectory using control law 3. 72
8.6 Stabilized trajectory using control law 4. 73
8.7 Stabilized trajectory using Q-law and different dynamical models. 74
8.8 Variation of the TOF as a function of the spacecraft initial mass. 75
8.9 Variation of the TOF with the specific impulse and thrust level. 75
8.10 Variation of the fuel mass with the specific impulse and thrust level. 76
8.11 Variation of the TOF with the target eccentricity. 76
8.12 Variation of the TOF with the target semi-major axis. 77
8.13 Variation of the TOF with high-thrust ΔV applied at first periapsis. 77
8.14 Comparison of the trajectory with and without a 40 m/s ΔV at periapsis. 78
8.15 Capture set and trajectory with lowest TOF for epoch 08/May/2024. 79
8.16 Capture set by stabilization TOF for all remaining epochs (I). 80
8.17 Capture set by stabilization TOF for all remaining epochs (II). 81
8.18 Capture with lowest stabilization TOF for all remaining epochs (I). 82
8.19 Capture with lowest stabilization TOF for all remaining epochs (II). 83
8.20 Evolution over time of the total and stabilization TOF. 85

9.1 Definition of HEO@Epoch and SRAE ref. frames and spherical coordinates. 90

10.1 Fuel consumption for grid of fuel-optimal heliocentric transfers. 97
10.2 $\theta(t_f)$ for grid of fuel-optimal heliocentric transfers. 97
10.3 $\Delta r = r(t_f) - r(t_d)$ for grid of fuel-optimal heliocentric transfers. 97
10.4 Ballistic TOF for grid of fuel-optimal heliocentric transfers. 97
10.5 Trajectories of example fuel-optimal heliocentric transfers. 98
10.6 Control history of example fuel-optimal heliocentric transfers. 99
10.7 Trajectory and control history of heliocentric transfer with ephemeris model. 100
10.8 Trajectories of heliocentric transfers with larger excess velocity. 101
10.9 Control history of heliocentric transfers with larger excess velocity. 102

LIST OF TABLES

2.1 Capture ratios and stability indices for different planetary systems and models. 13

4.1 Initial conditions for the verification of a capture set at Mars. 31
4.2 Comparison of the capture sets obtained in this work and in [19]. 32
4.3 Initial conditions for the study of the influence of the dynamics on capture. 33
4.4 Characteristics of the sets obtained with the different dynamical models. 33
4.5 Initial conditions for the capture sets to be targeted. 37
4.6 Characteristics of the capture sets at Mars for different epochs. 43

8.1 Initial conditions for verification of the orbit propagation with *AREO*. 68
8.2 Characteristics of the stabilized trajectory with different dynamical models. 74
8.3 Characteristics of the stabilization of the capture sets for all epochs. 84

10.1 Verification of heliocentric transfer with different number of nodes. 96
10.2 Fuel used and transfer time of transfers with different excess velocity. 102

11.1 Summary of TOF and fuel mass for each stage of the mission. 107

LIST OF SYMBOLS

μ Mass parameter of the restricted three-body problem

m_1 Mass of the first primary

m_2 Mass of the second primary

r_1 Distance to the first primary

r_2 Distance to the second primary

Ω Potential of the circular restricted three-body problem

J Jacobi constant of the circular restricted three-body problem

L_i Lagrange point i

C_i Jacobi constant associated to the Lagrange point i

e_p Eccentricity of the primaries

f True anomaly of the primaries

ω Potential of the elliptic restricted three-body problem

J_E Jacobi constant of the elliptic restricted three-body problem

H_k Kepler energy

θ Angle between the primaries line and the spacecraft

$l(\theta)$ Line from the target primary to the spacecraft

e Eccentricity of the spacecraft

h Altitude of pericenter of the spacecraft

f_0 True anomaly of the system at pericenter

W Stable set

∂W Weak Stability Boundary (WSB)

R_S Radius of the sphere of influence of the primary

n Number of revolutions around the primary

W_n Stable set after n revolutions

$\bar{W}_n$ Complementary of the stable set after n revolutions

$\mathscr{C}^n_{-1}$ Capture set after n revolutions

$\mathscr{E}^1_{-m}$ Escape set after n revolutions

$\mathscr{X}_n$ Unstable set after n revolutions

$\mathscr{K}_n$	Crash set after n revolutions
$\mathscr{D}_n$	Acrobatic set after n revolutions
S	Stability index
R_c	Capture ratio
C_3	Injection energy
v_∞	Velocity at the planet Sphere of Influence (SOI)
α	Right ascension
δ	Declination
i	Inclination
Ω	Right Ascension of the Ascending Node (RAAN)
ω	Argument of periapsis
$\boldsymbol{h}$	Angular momentum of the spacecraft
$\mathbb{P}$	Set of perturbing bodies in the N-body problem
U_{NSG}	Non-spherical gravity (NSG) gravitational potential
f_{NSG}	Non-spherical gravity (NSG) force per unit mass
f_{SRP}	Solar Radiation Pressure (SRP) force per unit mass
Q	Solar Pressure Constant
z	Mass-to-area ratio of the spacecraft
L_S	Luminosity of the Sun
C_R	Reflection Coefficient of the spacecraft
c	Speed of Light
$\boldsymbol{x}$	State variables vector
$\boldsymbol{u}$	Control variables vector
$\boldsymbol{p}$	Control problem static parameters vector
J	Performance function of the optimal control problem
Φ	End-cost term of the performance function
L	Integral term of the performance function
Ψ	Boundary conditions of the optimal control problem
$\boldsymbol{\lambda}$	Adjoint variables vector
$\boldsymbol{\nu}$	Vector of multipliers of the boundary conditions
$\bar{J}$	Augmented performance function
H	Hamiltonian

U Domain of feasible controls

I_{sp} Specific impulse

T_{max} Maximum thrust

c_{eff} Thruster effective velocity

$\boldsymbol{\alpha}$ Thrust direction unit vector

ε Performance function smoothing factor

S Switching function

F Nonlinear Programming (NLP) problem performance function

$\boldsymbol{c}$ Nonlinear Programming (NLP) problem constraint vector

$\boldsymbol{G}$ Jacobian of the NLP constraint vector

$\boldsymbol{H}_L$ Hessian of the Lagrangian of the NLP problem

$\boldsymbol{\zeta}_k$ Defects constraints

t_b Burn time

$m_{p,b}$ Mass of propellant burned

$m_{i,b}$ Wet mass of the spacecraft before burning

$\Delta\Delta V$ Gravity losses

ψ Thrust-to-weight ratio

LIST OF ABBREVIATIONS

16U 16-Unit

6U 6-Unit

API Application Program Interface

BPR Barycentric Pulsating Rotating Frame

COI Center of Integration

CRTBP Circular Restricted Three-Body Problem

DIRETTO DIREct collocation Tool for Trajectory Optimization

EME2000 Earth Mean Equator and Equinox of J2000

EPHE Ephemeris Model

ERTBP Elliptic Restricted Three-Body Problem

GRATIS GRAvity TIdal Slide

GTO Geostationary Transfer Orbit

HEO@Epoch Heliocentric Earth Orbital frame at Epoch

IAU International Astronomical Union

JPL Jet Propulsion Laboratory

KKT Karush-Kuhn-Tucker

LEO Low Earth Orbit

MarCO Mars Cube One

MARIO Mars Atmospheric Radiation Imaging Orbiter

NAIF Navigation and Ancillary Information Facility

NLP Nonlinear Programming

NSG Non-Spherical Gravity

ODE Ordinary Differential Equation

RnBP Restricted n-Body Problem

RTN@Epoch Radial-Tangential-Normal reference frame at Epoch

SOI Sphere of Influence

SRAE Spacecraft Range-Azimuth-Elevation

SRP Solar Radiation Pressure

TOF	Time of Flight
TPBV	Two-Point Boundary Value

I

INTRODUCTION

1

INTRODUCTION

1.1. CONTEXT

During the last few decades, interplanetary missions have become an increasingly hot topic, with Mars in particular becoming a target for several upcoming manned missions [1]. Recent findings regarding the presence of water ice and erosion on Mars [2] suggest that liquid water was once common on the planet surface and it could therefore be or have been a habitable environment for life. This is undoubtedly one of the main drivers for the current scientific interest in the exploration of the Red Planet.

Another major trend in the space industry in the last few years has been the surge in the use of small satellites, particularly CubeSats, which have made Low Earth Orbit (LEO) accessible to small companies and Universities. Now, CubeSats are increasingly been considered for planetary missions within the Solar System, including missions to Mars like the twin CubeSat mission Mars Cube One (MarCO) [3] that performed a fly-by around the Red Planet on November 2018. Like MarCO, CubeSats involved in these missions, due to their small size and limited capabilities (regarding power generation, propulsion systems, etc.), are typically restricted to perform fly-bys without completing any revolution around the target body [4]. However, they have the potential to become a differential factor in the exploration of Mars and democratize the access to translunar space in a similar manner to LEO.

In this context, ballistic captures are a relatively novel concept that uses gravitational perturbations to make a spacecraft reach another body and remain captured temporarily inside its sphere of influence without the need to spend any fuel. This concept was first used by Japanese spacecraft Hiten in 1991 [5] to reach the Moon using a fraction of the fuel that would have been used with a conventional transfer, and has since been applied and suggested for other missions [6]. Apart from the potential fuel savings, trajectories employing ballistic capture can have further advantages, like more flexibility for launch and arrival dates and a safer approach for arrival strategies, avoiding the associated dangers of single-point injections [7]. For these reasons, the use of ballistic capture along with low-thrust or high-thrust propulsion systems can be a revolutionary approach for the design of missions towards Mars and other interplanetary targets, and particularly for small satellites with limited capabilities. CubeSats missions like MarCO could perform multiple revolutions around an interplanetary target without the need of any propulsive maneuver, or follow a stand-alone end-to-end mission to Mars like the ones that will be studied in this Thesis.

The concept of targeting a ballistic capture trajectory around Mars from Earth has already been explored several times in literature, either using the invariant manifolds of the Circular Restricted Three-Body Problem (CRTBP) [8] or an algorithmic generation of capture sets based on simple definitions of stability and revolutions [7]. The latter will be the approach used in this work. The studies found in literature have however used high-thrust impulsive maneuvers to target the capture state, leading to transfers that are often less fuel- and time-efficient than conventional Hohmann transfers. The required maneuvers to target the capture state take place at great distances away from Mars when the spacecraft is traveling at small velocities, thus not making use of the so-called *Oberth effect*. Low-thrust propulsion, which considers a continuous thrust profile rather than single-point maneuvers, should be a much more efficient option for these transfers. This conclusion is shared by Moral et al. [9], and Cruz Chambel de Aguiar [10] used an optimizer to target several captures at Mars for different arrival dates using low-thrust propulsion.

1.2. OBJECTIVE

The present Thesis serves as an extension to Cruz Chambel de Aguiar's work [10] and as an application to a particular science mission to Mars. The main objective will thus be to study the mission concept of a small satellite traveling to a science orbit around Mars while using ballistic capture and dual low/high-thrust propulsion, as well as to determine whether such a concept introduces any significant advantages with respect to a more traditional mission design. One of the main innovations of the current project will be the study of the complete end-to-end mission. To the author's best knowledge, it is the first time that a complete mission design from Earth to a science orbit around Mars is studied using ballistic capture and dual chemical-electric propulsion.

The mission concept in this research project will consider a 16-Unit (16U) CubeSat and will start with a highly elliptical orbit around Earth, like a Geostationary Transfer Orbit (GTO), which are frequently used for telecommunications satellites on Earth and offer a much greater number of launches per year than hyperbolic escape trajectories, therefore adding much more flexibility for piggyback options. A high-thrust chemical propulsion system will be used to raise the orbit and escape Earth quickly, in order to limit the radiation damage within the Van Allen belts. The spacecraft will then start a low-thrust deep-space cruise towards Mars, where it will become ballistically captured. Finally, the orbit will be circularized to reach the final science orbit where the nominal mission operations will take place.

In the present study, the science orbit considered will be an areostationary orbit. These are equatorial orbits with the same orbital period as the rotation of Mars and analogous to geostationary orbits on Earth. A spacecraft in such an orbit will remain stationary in a reference frame rotating with the planet, if perturbations like Mars' non-spherical gravity and the presence of Phobos and Deimos are neglected. The station-keeping required to maintain the spacecraft in this orbit is out of the scope of the present Thesis. For the purpose of this study, the target orbit will be assumed to be a circular equatorial orbit around Mars with a radius of 20,428 km [11].

The study and optimization of the characteristics of the ballistic capture, as well as the high-thrust and low-thrust sections of the transfer, will be studied separately and in conjunction, and will lead to a complete mission trajectory from launcher injection to the science orbit around Mars. Therefore, the main research question that the project will aim to answer is the following:

What is the optimal mission profile from Earth orbit to a specific science orbit around Mars combining dual chemical-electric propulsion and ballistic capture?

1.3. STRUCTURE

This Section will describe the structure of the present report. After this introduction, Chapter 2 will present a theoretical background of all the concepts necessary for the study of interplanetary missions including ballistic capture and dual chemical-electric propulsion. The following Chapters will introduce the study of the different legs of the trajectory. Fig. 1.1 shows a graphical layout of this structure, with the names of the different tools that will be employed to study the problem.

For each stage of the mission, one chapter will show the methodology followed to study the problem and the next chapter will present the verification of said methodology and the results obtained. Part III will study the ballistic capture around Mars, including the generation and selection of the capture sets. A tool named GRATIS will be used to obtain capture sets constructed from a grid of initial orbital elements. Part IV will study the first part of the trajectory, that is, the escape from Earth using high-thrust, using a simple tool known as *TERRA*. The stabilization of the capture trajectories around Mars in order to reach a stable science orbit around the planet will be the subject of Part V, which will use a tool named *AREO*. A specific capture will be selected based on the characteristics of the stabilization process. Then, the heliocentric transfer from the escape conditions from Earth targeting the selected captures will be studied and optimized in Part VI using DIRETTO. With all these tools, it will be possible to obtain an estimation of the total time of flight and fuel consumption of the complete mission. Finally, Chapter 11 will introduce some conclusions and recommendations for the interested reader.

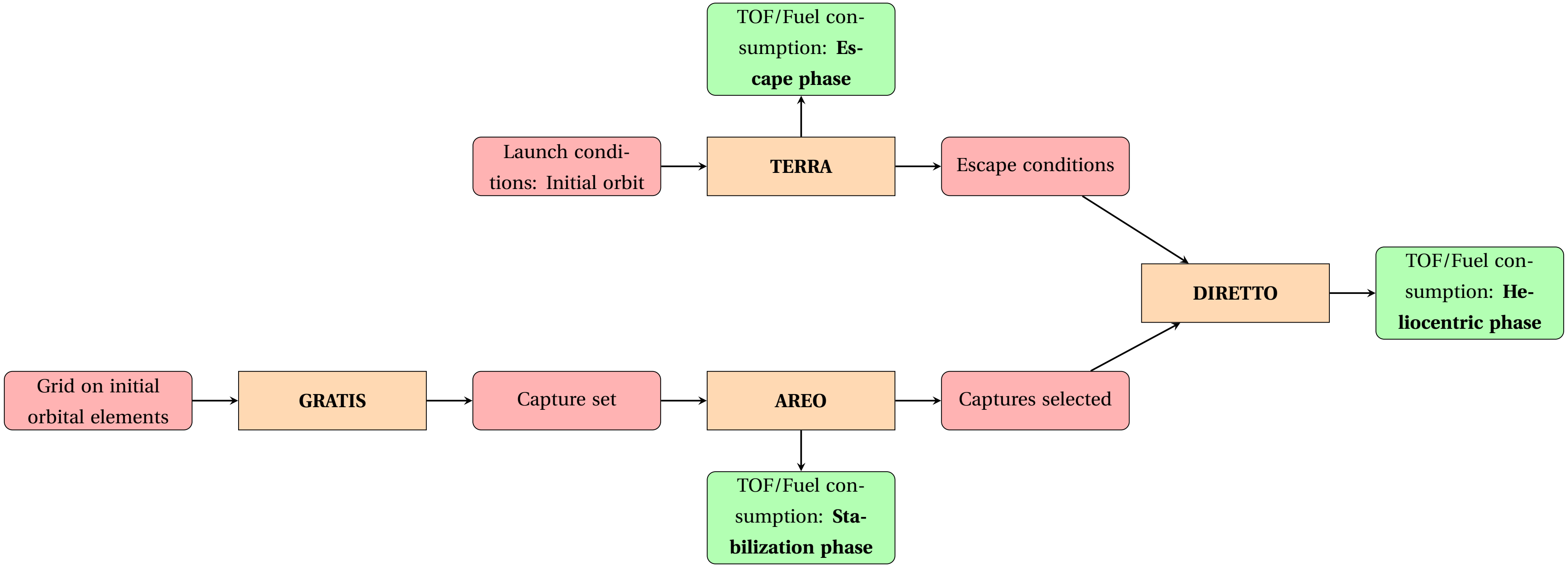
TOF/Fuel consumption: **Escape phase**
Launch conditions: Initial orbit
TERRA
Escape conditions
DIRETTO
TOF/Fuel consumption: **Heliocentric phase**
Grid on initial orbital elements
GRATIS
Capture set
AREO
Captures selected
TOF/Fuel consumption: **Stabilization phase**

Figure 1.1: Summary of the computational tools that will be used to study the different stages of an Earth-to-Mars mission with ballistic capture and dual chemical/electric propulsion.

II

THEORETICAL BACKGROUND

2

THEORETICAL BACKGROUND

2.1. INTRODUCTION

The present Chapter will introduce a theoretical background of the different concepts required to study an interplanetary mission that employs ballistic capture and dual low/high-thrust propulsion. Section 2.2 will include the definition of terms necessary to describe ballistic capture, as well as the effect of the dynamics of the problem and the state of the spacecraft on the capture. Section 2.3 will introduce the optimization problem describing the interplanetary low-thrust trajectory of the spacecraft, including the Nonlinear Programming (NLP) concepts that will be employed in the present study. Finally, the dynamics of the high-thrust problem will be presented on Section 2.4, paying particular attention to the modeling of the gravity losses associated with finite burns.

2.2. BALLISTIC CAPTURE

DEFINITIONS AND ALGORITHMIC METHOD

Ballistic captures are, as stated before, a phenomenon by which a spacecraft approaches a body and starts orbiting it solely by the means of gravitational and dynamical perturbations, without the need of any propulsive maneuver. The problem indeed requires the introduction of the gravity field of at least two bodies, hence making the CRTBP a logical starting point for studying the problem. A study of the Lagrangian equilibrium points in the CRTBP and the associated invariant manifold has been used in literature to study ballistic capture to Earth's Moon [12, 13] and to other planets in the Inner Solar System [8]. This approach uses the invariant manifolds of two coupled three-body problems to generate trajectories that travel from one system to the other either ballistically or using high- or low-thrust [14]. An important drawback with this approach is that the characteristics of the captures generated are not known a priori, what is particularly problematic when targeting a specific orbit around the primary like is the case in most mission design problems. Besides, it is not straight-forward to extend the method above to more complex dynamical set-ups like an ephemeris model, requiring the definition of new structures analogous to the invariant manifolds of the CRTBP [15].

For these reasons, a different approach will be the one employed in this work, based solely on simple definitions of stability, energy and revolutions around the primary. This algorithmic method, introduced in [16] and updated in several other articles since, requires the construction of a computational grid of initial conditions from which the trajectories will be generated. These initial conditions will be expressed as the orbital parameters of an osculating ellipse around the target body. It will be assumed that at the initial epoch the spacecraft is located at the periapsis of this osculating ellipse. The set of orbital parameters and the initial epoch will thus define the state of the spacecraft:

$$\boldsymbol{x_0} = \boldsymbol{x}(t_0) = \{r_p, e, i, \Omega, \omega, M\}(t_0) = \{r_{p_0}, e_0, i_0, \Omega_0, \omega_0, 0\} \tag{2.1}$$

where r_p is the radius of periapsis, e is the eccentricity, i is the inclination, Ω is the longitude of the ascending node, ω is the argument of periapsis and M is the mean anomaly. The condition $M = 0$ implies that the spacecraft is located at the periapsis of the osculating ellipse.

The initial conditions are then integrated and classified depending on their behavior. The criteria for classifying these trajectories has varied in different versions in the literature of this method. In this work, the conditions will be classified into the following sets [17]:

- **Weakly stable set** $\mathscr{W}_n$, when the spacecraft performs n revolutions around the primary without escaping it or colliding with any body.
- **Unstable set** $\mathscr{X}_n$, if the spacecraft performs $n-1$ revolutions around the primary and then escapes it.
- **Crash set** $\mathscr{K}_n$, if the spacecraft performs $n-1$ revolutions around the target and then collides with it.
- **Acrobatic set** $\mathscr{D}_n$, if the spacecraft does not fulfill any of the conditions above before the end of the maximum time of integration.

These concepts can easily be extended for backwards motion of the spacecraft ($\mathscr{W}_{-n}$, $\mathscr{X}_{-n}$, $\mathscr{K}_{-n}$, $\mathscr{D}_{-n}$). This allows to define the ballistic capture set as follows:

$$\mathscr{C}_{-1}^{n} = \mathscr{W}_n \cap \mathscr{X}_{-1} \tag{2.2}$$

This set will contain the trajectories where the spacecraft approaches the primary and performs n revolutions around it. Due to their predictability, ideal orbits belonging to this set will be those that have a stable, quasi-Keplerian post-capture behavior. A performance index called *stability index* is introduced to select these captures, defined as follows:

$$S = \frac{t_n - t_0}{n} \tag{2.3}$$

where n is the number of revolutions around the primary and t_0 and t_n are the epochs at the beginning of the integration and the n-th revolution, respectively. In practice, S acts as a sort of orbital period of the capture trajectory, and low values of S (close to the value a Keplerian orbit would have) correlate well with the so-called ideal orbits [17].

EFFECT OF THE SPACECRAFT STATE ON THE CAPTURE

The osculating orbital elements, as well as the initial epoch for the capture, will determine whether the spacecraft reaches capture and the characteristics of the resulting trajectory. Literature shows that a very high value of the osculating eccentricity e_0 is required for capture to occur, typically between 0.9 and 1. An analytical derivation of the minimum value required can be followed in [18].

An study of the effect of the osculating inclination i_0 and longitude of the ascending node Ω_0 on the capture sets was conducted in [19] for several Sun-planet systems. The minimum stability index of the capture set as defined above is used to characterize the sets, as well as the so-called capture ratio:

$$R_c = \frac{N_{\mathscr{C}^n_{-1}}}{N_{ic}} \tag{2.4}$$

where $N_{\mathscr{C}^n_{-1}}$ is the number of capture trajectories and N_{ic} is the total number of initial conditions.

The results for Mars are shown in Fig. 2.1. Surprisingly, the greatest number of captures does not happen on the Sun-Mars plane, but at a certain non-negligible inclination. There are in fact two peaks, around $i_0 \approx 40-70°$ for prograde motion and $i_0 \approx 150-160°$ for retrograde motion, and the capture ratio also depends on the values of Ω_0. Meanwhile, the most stable orbits seem to correspond with polar orbits ($i_0 \approx 90°$) for specific values of Ω_0. These results are similar for other planet-Sun systems in the Solar System. The physical reasons behind these variations of the capture process with the orbital plane orientation are however not clear [19].

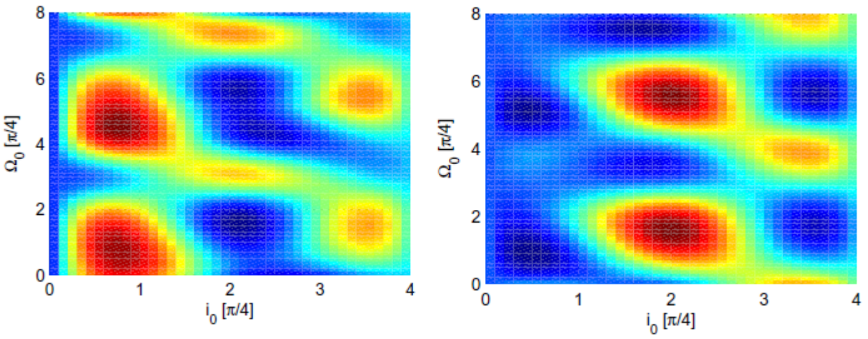

Figure 2.1: Variation of the capture ratio R_c (left) and minimum stability index S_{min} (right) as a function of i_0 and Ω_0 for the Sun-Mars case, with $e_0 = 0.95$ and Mars at its periapsis around the Sun [19].

The remaining two orbital elements, the argument of periapsis ω_0 and the radius of periapsis r_{p_0}, are usually the ones that make up the grid, with a fixed value for e_0, i_0 and Ω_0. Fig. 2.2 shows a sample capture set around Mercury with a grid on r_{p_0} and ω_0.

Finally, the epoch t_0 has a great influence on the capture, when the eccentricity of the smaller primary is considered in the model (e.g. in the Elliptic Restricted Three-Body Problem (ERTBP) or an ephemeris model). Mars has a non-negligible eccentricity in its orbit around the Sun, as will be explored later, and this has an important effect on the capture sets around the planet. Fig. 2.3 shows the values of the planetary true anomaly that lead to a higher capture ratio or lower stability index for all planets in the Solar System and for prograde and retrograde motion [19]. For the case of prograde motion around Mars, the greatest number of capture trajectories will occur around $f_0 = -135°$, and the most regular orbits take place around $f_0 = 45°$.

EFFECT OF THE PROBLEM DYNAMICS ON THE CAPTURE

Like stated before, ballistic capture requires the gravitational attraction of at least two bodies, hence the CRTBP can be considered the most basic model for the study of the problem. Already in Makó & Szenkovits [20], the ERTBP was proposed as an improved alternative. In the ERTBP, the forbidden and accessible regions

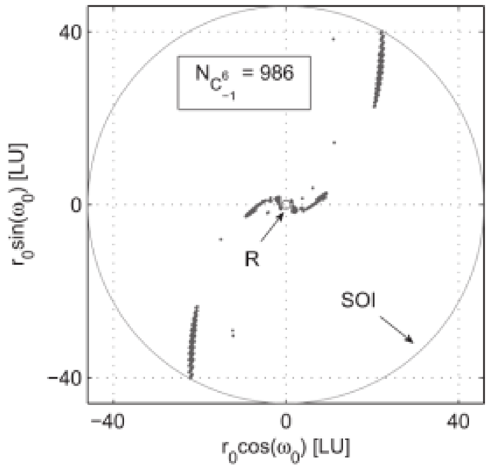

Figure 2.2: Points in the capture set $\mathscr{C}^6_{-1}$ around Mercury with $e_0 = 0.95$, $i_0 = 45°$, $\Omega_0 = 135°$, and $t_0 = 2458891.7$JD. The Sphere of Influence (SOI) and radius (R) of Mercury are also represented [19].

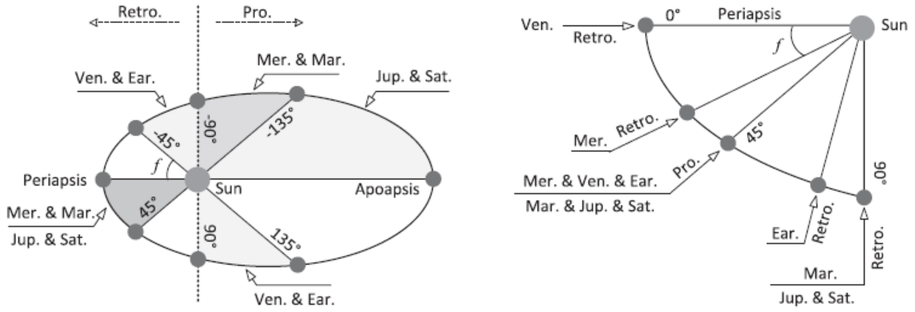

Figure 2.3: Planetary true anomalies of maximum capture ratio (left) and minimum stability index (right) for all planets in the Solar System and prograde and retrograde motion [19].

of the system vary with time. This can benefit capture if the spacecraft is trapped within a region around the target when the planetary true anomaly evolves. Mars has a significant planetary eccentricity of 0.0934, thus the CRTBP may be too simplified for the study of capture at Mars. Table 2.1 shows a comparison between the $\mathscr{C}^6_{-1}$ capture sets for different planetary systems using the CRTBP, ERTBP and full Ephemeris Model (EPHE). It can be seen how a significant difference is introduced between the CRTBP and the ERTBP, with the ephemeris model being much closer to the latter. This reinforces the hypothesis that the eccentricity of Mars represents the most important perturbation with respect to the CRTBP.

On the other hand, Moral et al. [9] also employ the N-Body problem with real planetary ephemeris to model the capture sets. They propagate the same initial conditions with both the ERTBP and the full ephemeris model and compute the position error between them, shown on Fig. 2.4. The error reaches just above a million kilometers after 1.5 years of integration, suggesting that the ephemeris model does indeed introduce very significant perturbations, at least when considering the detailed trajectory of a specific orbit during a long integration time. This, along with the fact that the ephemeris model on Table 2.1 leads to a higher capture ratio for the case of Mars, is the main reason why an N-body ephemeris model will be used in this work to model the ballistic capture process. However, other dynamic models will be employed and used for comparison in Chapter 4.

The effect of introducing natural satellites in the model on the characteristics of the captures is explored in

Table 2.1: Capture ratios and minimum stability indices for $\mathscr{C}^6_{-1}$ capture sets for different planetary systems and models. Orbits corresponding to the minimum stability index are shown in the Barycentric Pulsating Rotating Frame (BPR) frame [19].

System	Model	Mercury	Venus	Earth	Mars	Jupiter	Saturn
$\mathcal{R}_c$ (‰)	CRTBP	0.020	0.118	0.148	0.203	0.311	0.182
	ERTBP	0.907	0.128	0.161	0.295	0.207	0.223
	EPHE	0.907	0.128	0.160	0.315	0.225	0.264
$\mathcal{S}_{\min}$ (TU)	CRTBP	3,037	7,367	9,277	15,180	56,809	77,823
	ERTBP	1248	7321	7837	10,143	38,421	71,065
	EPHE	1248	7229	7837	10,143	38,748	70,991
Orbit ($\mathcal{S}_{\min}$)	CRTBP	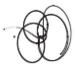	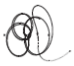	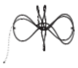	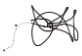	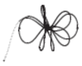	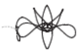
	ERTBP	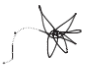	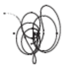	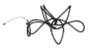	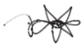	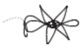	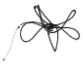
	EPHE	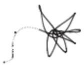	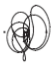	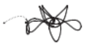	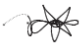	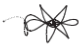	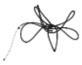

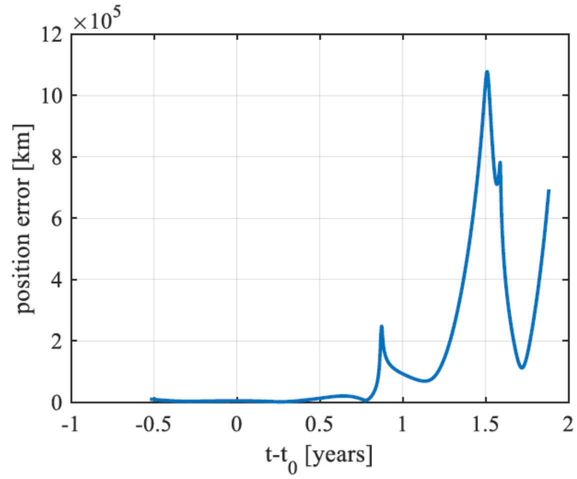

Figure 2.4: Position error between the ERTBP and the ephemeris model as a function of time for a specific capture trajectory [9].

[21], where captures at the Earth were compared including or not the effect of the Moon. It is determined that the presence of the Moon increases the number of captures, improves their regularity and for some cases increases the pre-capture energy of the trajectories. This is the case particularly for those initial conditions from which the spacecraft performs a flyby around the natural satellite before reaching the target. Similar results are obtained for the case of Jupiter and the Galilean moons.

However, further work including the Martian satellites on the generation of the capture sets did not introduce any significant difference with respect to the nominal case [10]. Phobos and Deimos are indeed extremely small when compared with Earth's Moon or the Galilean satellites. Furthermore, it is suggested that the natural satellites only have a significant impact on the qualities of the capture when they are targeted for a flyby. For this reason, the Martian moons will be neglected in the ephemeris model used in this work.

Finally, Non-Spherical Gravity (NSG) at Mars and Solar Radiation Pressure (SRP) can also be included as additional perturbations in the model. This was done in [10], with the results shown in Figs. 2.5 and 2.6. It can be seen how the minimum radius of periapsis increases slightly when NSG is included. However, the number of captures with a low stability index increases significantly. In that sense, it can be argued that including NSG as an additional perturbation can facilitate capture. Similarly, and although the effect is not very large, adding a simple cannonball SRP model can increase the capture ratio and decrease the stability index of the capture sets, thus also favoring capture in the system. These conclusions will be studied in Chapter 4, where a comparison of two ephemeris models including or not NSG and SRP will be conducted.

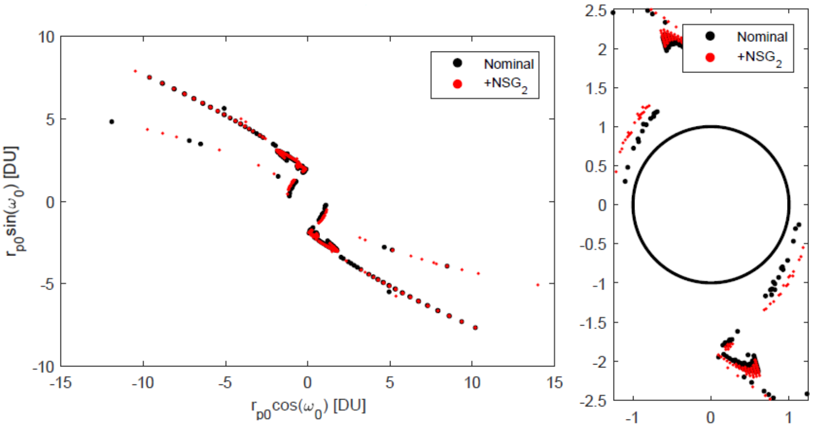

Figure 2.5: Sets of ballistic captures in $\mathscr{C}^6_{-1}$ for captures at Mars with point mass gravity and Non-Spherical Gravity up to degree $n = 2$. On the right, central part of the set is zoomed in with the circle representing the surface of Mars [10].

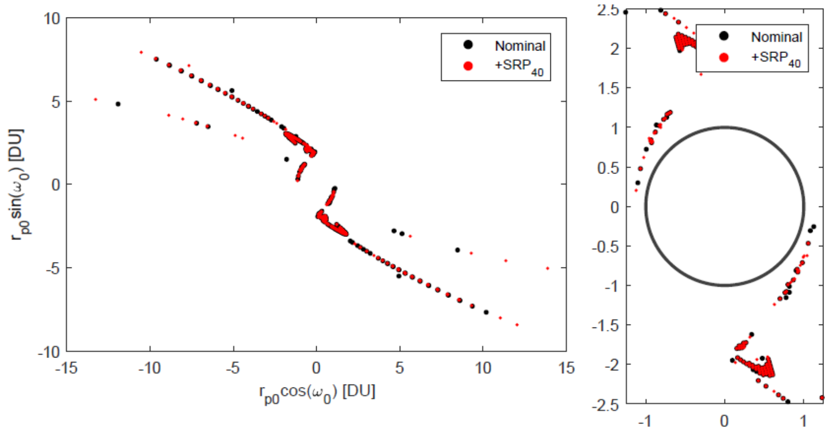

Figure 2.6: Sets of ballistic captures in $\mathscr{C}^6_{-1}$ for captures at Mars with and without a Solar Radiation Pressure cannonball model. On the right, central part of the set is zoomed in with the circle representing the surface of Mars [10].

2.3. LOW-THRUST OPTIMIZATION

Low-thrust space trajectories are typically studied as an optimal control problem. Such a problem consists of four main elements: a dynamical model, path constraints, a performance criterion and a task description (boundary conditions).

The dynamics of the problem are expressed with a mathematical model, which typically takes the form of a vectorial Ordinary Differential Equation (ODE) written in explicit form and known as the state or system equations:

$$\frac{\mathrm{d}\boldsymbol{x}}{\mathrm{d}t} = \boldsymbol{f}(\boldsymbol{x}, \boldsymbol{u}, t, \boldsymbol{p}) \tag{2.5}$$

where $\boldsymbol{x}(t) \in \mathbb{R}^n$ and $\boldsymbol{u}(t) \in \mathbb{R}^m$ are the n state variables and m control variables, respectively. Finally, $\boldsymbol{p} \in \mathbb{R}^q$ is a vector of static parameters describing the problem.

Path constraints define the allowable values of the state and control variables and are in practice expressed as inequalities. An evolution of the state and control variables that complies with the constraints is known as an *admissible control* and *admissible trajectory*, respectively [22].

In general, no constraints are set in practice on the state variables, and the control variables are limited by a simple inequality of the form $\boldsymbol{u}_{min} < \boldsymbol{u} < \boldsymbol{u}_{max}$. However, algebraic path equality constraints of the form

$$\boldsymbol{0} = \boldsymbol{g}(\boldsymbol{x}(t), \boldsymbol{u}(t), t, \boldsymbol{p})) \tag{2.6}$$

or algebraic inequality constraints of the form

$$0 \leq \boldsymbol{g}(\boldsymbol{x}(t), \boldsymbol{u}(t), t, \boldsymbol{p})) \tag{2.7}$$

could also be imposed [23].

On the other hand, the performance of the system is measured with a certain performance function, and the optimal control is then defined as the one that minimizes this index. Performance functions that immediately come to mind in the case of spacecraft trajectory design are the time of flight or fuel consumption. In any case, the performance function will be a scalar expression of the form

$$J = \Phi(\boldsymbol{x}(t_f), t_f, \boldsymbol{p}) + \int_{t_0}^{t_f} L(\boldsymbol{x}, \boldsymbol{u}, t, \boldsymbol{p})\mathrm{d}t \tag{2.8}$$

that indeed depends in its more general form not only on the final state of the system but also on its evolution over time. In particular, if the performance function includes only the end-cost term Φ, only the integral term L or both, the problem is named a *Mayer* problem, *Lagrange* problem or *Bolza* problem, respectively [23]. It should be noted that the terminal time t_f could be fixed or not depending on the nature of the problem. Of course, the performance index can be maximized by simply minimizing its negative.

Finally, the task description is expressed through initial and final boundary conditions. The final state is usually included, by requiring the system to reach a state within a certain *target set* S, which in its most constrained form will be a specific point. The initial and final boundary conditions will follow expressions of the form [23]

$$\begin{aligned} \boldsymbol{\Psi}_{0l} \le \boldsymbol{\Psi}(\boldsymbol{x}(t_0), \boldsymbol{u}(t_0), t_0, \boldsymbol{p}) \le \boldsymbol{\Psi}_{0u} \\ \boldsymbol{\Psi}_{fl} \le \boldsymbol{\Psi}(\boldsymbol{x}(t_f), \boldsymbol{u}(t_f), t_f, \boldsymbol{p}) \le \boldsymbol{\Psi}_{fu} \end{aligned} \tag{2.9}$$

where $\boldsymbol{\Psi} \in \mathbb{R}^q$ represents the q boundary conditions.

To sum up, the *optimal control function* $\boldsymbol{u}^\star$ will be the one that minimizes the performance index J while satisfying the initial and terminal boundary conditions, the path constraints and the dynamic constraints (differential equations). The corresponding evolution of the state variables $\boldsymbol{x}^\star$ will be the *optimal trajectory* [22, 24]. Optimal control problems can be solved with direct or indirect methods.

OPTIMAL CONTROL THEORY

Indirect methods employ calculus of variations. If $\boldsymbol{\nu} \in \mathbb{R}^q$ is the constant vector of multipliers of the boundary conditions and $\boldsymbol{\lambda} \in \mathbb{R}^n$ is the variable vector of adjoint or co-state multipliers of the dynamics, an augmented performance function can be defined as follows:

$$\bar{J} = \Phi(\boldsymbol{x}(t_f), t_f, \boldsymbol{p}) + \boldsymbol{\nu}^T \Psi(\boldsymbol{x}(t_f), \boldsymbol{u}(t_f), t_f, \boldsymbol{p}) + \int_{t_i}^{t_f} \left[L(\boldsymbol{x}, \boldsymbol{u}, t, \boldsymbol{p}) + \boldsymbol{\lambda}^T (\boldsymbol{f}(\boldsymbol{x}, \boldsymbol{u}, t, \boldsymbol{p}) - \dot{\boldsymbol{x}}) \right] \mathrm{d}t \tag{2.10}$$

where both the dynamics and the boundary conditions are included. The stationary points of $\bar{J}$, i.e. those that fulfill $\delta \bar{J} = 0$, are possible solutions of the optimal control problem [22, 23, 25]. Introducing the *Hamiltonian*:

$$H(\boldsymbol{x}, \boldsymbol{\lambda}, \boldsymbol{u}, t, \boldsymbol{p}) = L(\boldsymbol{x}, \boldsymbol{u}, t, \boldsymbol{p}) + \boldsymbol{\lambda}^T \boldsymbol{f}(\boldsymbol{x}, \boldsymbol{u}, t, \boldsymbol{p}) \tag{2.11}$$

the following expression can be derived that represents the conditions for optimality:

$$\dot{\boldsymbol{x}} = \frac{\partial H}{\partial \boldsymbol{\lambda}} \qquad \dot{\boldsymbol{\lambda}} = -\frac{\partial H}{\partial \boldsymbol{x}} \qquad 0 = \frac{\partial H}{\partial \boldsymbol{u}} \tag{2.12}$$

These state, adjoint and control equations are known as the Euler-Lagrange equations [22, 25].

When the initial and final state of the system is given, the problem is essentially a Two-Point Boundary Value (TPBV) problem. If the problem contains algebraic inequality path constraints, it can become a multiple-point boundary value problem when constraints change from being active to inactive and vice-versa [23]. When the state is not specified for the initial and/or final time of the optimization, natural boundary conditions will arise to form the necessary *transversality conditions* [23]. In practice the following conditions will be enforced:

$$\begin{aligned} \left(\frac{\partial \Phi}{\partial x_i} + \boldsymbol{\nu}^T \frac{\partial \psi}{\partial x_i}\right)\bigg|_{t=t_f} = \lambda_i(t_f) \quad &\text{or} \quad x_i(t_0) \ \text{given} \\ 0 = \lambda_i(t_0) \quad &\text{or} \quad x_i(t_0) \ \text{given} \\ 0 = \left(\frac{\partial \Phi}{\partial t} + H\right)\bigg|_{t=t_f} \quad &\text{or} \quad t_f \ \text{given} \\ 0 = H\bigg|_{t=t_0} \quad &\text{or} \quad t_0 \ \text{given} \end{aligned} \tag{2.13}$$

NONLINEAR PROGRAMMING

A Nonlinear Programming (NLP) problem is a problem where a certain scalar performance function $F(\boldsymbol{x})$, depending on the n variables $\boldsymbol{x}$, is minimized, possibly subject to a series of constraints. For now, it will be assumed that these are m equality constraints of the form $\boldsymbol{c}(\boldsymbol{x}) = 0$. The Lagrangian of this problem is [25]

$$L(\boldsymbol{x}, \boldsymbol{\lambda}) = F(\boldsymbol{x}) - \boldsymbol{\lambda}^T \boldsymbol{c}(\boldsymbol{x}) \tag{2.14}$$

where $\boldsymbol{\lambda}$ are the m Lagrange multipliers. This function leads to the following set of conditions for optimality [23]:

$$\begin{aligned} \nabla_x L &= \boldsymbol{g}(\boldsymbol{x}) - \boldsymbol{G}^T(\boldsymbol{x})\boldsymbol{\lambda} = 0 \\ \nabla_\lambda L &= -\boldsymbol{c}(\boldsymbol{x}) = 0 \end{aligned} \tag{2.15}$$

where $\boldsymbol{g}(\boldsymbol{x}) = \nabla_x F$ and $\boldsymbol{G}$ is the Jacobian of the constraint vector. The system (2.15) can be solved with a Newton method, starting from an initial guess $(\boldsymbol{x}, \boldsymbol{\lambda})$ and applying corrections $(\Delta\boldsymbol{x}, \Delta\boldsymbol{\lambda})$ by solving the linear system known as the *Karush-Kuhn-Tucker (KKT) system* [25]:

$$\begin{bmatrix} \boldsymbol{H}_L & -\boldsymbol{G}^T \\ \boldsymbol{G} & 0 \end{bmatrix} \begin{pmatrix} \Delta\boldsymbol{x} \\ \Delta\boldsymbol{\lambda} \end{pmatrix} = \begin{pmatrix} -\boldsymbol{g} \\ -\boldsymbol{c} \end{pmatrix} \tag{2.16}$$

where $\boldsymbol{H}_L$ is the Hessian of the Lagrangian in x, that is:

$$\boldsymbol{H}_L = \nabla_x^2 F - \sum_{i=1}^{m} \lambda_i \nabla_x^2 c_i \tag{2.17}$$

In the general case of having inequality constraints of the form $\boldsymbol{c}(\boldsymbol{x}) \geq 0$ instead of equality constraints as considered above, constraints that are satisfied strictly (i.e. $c_i(\boldsymbol{x}) > 0$) are called inactive and can be neglected, while the rest are treated as equality constraints in their bounds, that is, $c_i(\boldsymbol{x}) = 0$ [23]. However, this is typically not known a priori, and therefore assumptions need to be made and confirmed in an iterative fashion. Direct methods make use of discretization to transform the infinite-dimensional optimization problem into a finite-dimensional optimization problem that can be solved with NLP theory [24].

It can be demonstrated that, as the number of variables grows with a finer time discretization, the KKT problem approaches the underlying optimal control problem related by direct transcription [23].

2.4. HIGH-THRUST PROPULSION

Unlike low-thrust propulsion, high-thrust chemical propulsion has a very short burn time, sometimes modeled even as instantaneous burns. In reality, and especially for the case of small satellites whose propulsion systems have more limited thrust values, maneuvers are not purely impulsive and a certain burn time is required for each maneuver. This leads to the generation of gravity losses. In practice, there will be a trade-off between how fast the escape shall be reached and the gravity losses due to this finite thrust.

Fig. 2.7 shows the typical geometry of a hyperbolic escape with high-thrust propulsion. The direction of the departure hyperbola, $\boldsymbol{V}_{\infty_e}$, with respect to the velocity vector of the Earth relative to the Sun, $\boldsymbol{V_e}$, will depend on the position in the parking orbit at which the impulsive maneuver takes place [26]. The spacecraft leaves the sphere of influence of the Earth with velocity $\boldsymbol{V_1}$ relative to the Sun, with

$$\boldsymbol{V_1} = \boldsymbol{V_e} + \boldsymbol{V_{\infty_e}} \tag{2.18}$$

The magnitude and direction of this velocity, along with the position at which the spacecraft leaves the sphere of influence, will determine the heliocentric transfer towards Mars.

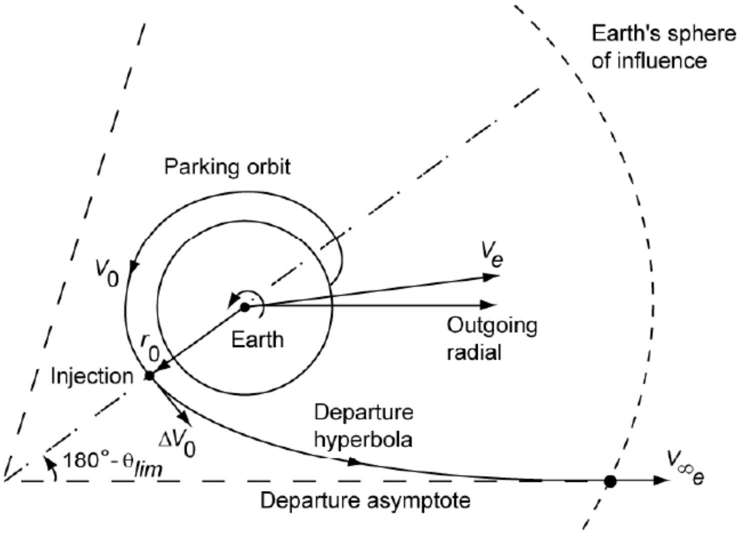

Figure 2.7: Geometry of the ascent trajectory, coasting phase and escape hyperbola of a typical interplanetary flight [26].

It can be easily demonstrated that maneuvers are most efficient when performed at the location of highest spacecraft velocity, that is, the periapsis of the orbit. This is known as the *Oberth effect*. If the initial orbit has perigee and apogee altitudes of r_{p_0} and r_{a_0}, respectively, the impulsive ΔV that has to be applied at perigee to reach a hyperbolic orbit with excess velocity V_∞ is [27]

$$\Delta V = \sqrt{\left(\frac{2\mu}{r_{p_0}} + V_\infty^2\right)} - \sqrt{2\mu\left(\frac{1}{r_{p_0}} - \frac{1}{r_{p_0} + r_{a_0}}\right)} \tag{2.19}$$

The global escape strategy will be very similar when considering a finite-thrust burn or set of burns. These will be now characterized by a specific burn time t_b and a thrust level T. The combination of $t_b - T$ will vary depending on the number of burns as well as the specific impulse I_{sp}. The amount of propellant that is spent in each burn can then be computed as

$$m_{p,b} = \frac{T \cdot t_b}{I_{sp} \cdot g} \tag{2.20}$$

where g is the gravitational acceleration, which can be assumed to be 9.81 m/s^2.

The ΔV for each burn can then be computed using Tsiolkovsky rocket equation [28]:

$$\Delta V_b = -I_{sp}\, g \ln\left(1 - \frac{m_{p,b}}{m_{i,b}}\right) \tag{2.21}$$

where $m_{i,b}$ is the wet mass of the spacecraft before each burn.

Depending on the thrust levels and specific impulse, as well as the burn time for each maneuver, there will be a trade-off between the total time of the escape and the amount of propellant used.

Gravity losses occur when maneuvers are modeled as burns with non-zero thrusting time instead of impulses, and the thrust vector is not continuously pointed perpendicular to the position vector. The gravity losses can be expressed as the relative difference between the actual ΔV and the one that would be obtained with an impulsive burn, $(\Delta V)_i$, as follows [26]:

$$\Delta\Delta V = \left(\frac{\Delta V - (\Delta V)_i}{(\Delta V)_i}\right) \cdot 100\% \tag{2.22}$$

The value of $\Delta\Delta V$ is not immediate to compute, and depends on a series of factors, like the orbital energy before and after the burn, the evolution of the thrust angle δ, the effective exhaust velocity or the *thrust-to-weight ratio* $\psi = \frac{T}{g_0 m_{i,b}}$. Typically, the gravity losses are relatively small when the spacecraft is already in a stable parking orbit, of just a few percentage points [26, 28].

In general, it can be assumed that any burn that does not take place at perigee will result in inefficiency and will infer a certain gravity loss. The loss will be higher the farther the spacecraft is from perigee when burning. Maneuvers that require a large ΔV can imply a long burning time and consequently a significant loss of efficiency. Some strategies can be employed to alleviate this problem. An obvious one is an increase in the thrust-to-weight ratio, the specific impulse or both. It is however difficult in practice to increase the value of these parameters, particularly for small satellites that have important sizing and control limitations.

An strategy that does not involve any change in the actual propulsion system is to divide the escape phase into several apogee-raising maneuvers. These intermediate high-apogee orbits are generally used up to an apogee altitude between 100,000 and 300,000 km. After that, the orbital period can be quite long, increasing significantly the time of flight, and the Sun gravity field becomes a strong perturbation. Hence, when an altitude in this range is reached, a final perigee burn injects the spacecraft into an escape orbit. This maneuver will typically experience a greater loss and can reach values of 10 to 20% [27]. It is readily apparent that there will be a trade-off between the number and size of the apogee-raising maneuvers and the total time from launch to escape.

III

BALLISTIC CAPTURE

3

METHODOLOGY

3.1. INTRODUCTION

The present Chapter will describe the methodology used to generate capture sets around Mars, and the tools employed that implement this methodology. Section 3.2 will describe the problem statement, from the characteristics of the spacecraft to the mission objective. Section 3.3 will introduce the reference frames used to study the problem. The dynamics of the problem, along with the equations of motion that need to be integrated, will be outlined in Section 3.4. A description of the classification algorithm used to generate the different sets is given in Section 3.5. Finally, Section 3.6 will introduce some aspects regarding the actual implementation of the algorithm, like the numerical integrator employed or the use of the SPICE Toolkit and parallel computing.

3.2. PROBLEM STATEMENT

Like stated in previous Chapters, the present Thesis aims to study the design of a small satellite mission targeting an areostationary orbit around Mars. In particular, the spacecraft will be a 16U CubeSat, inspired by the design of Sanz Casado [4] for MARIO shown in Fig. 3.1. For comparison, the MarCO probes that recently performed a fly-by around Mars were 6-Unit (6U) CubeSats, but they did not require the propulsion systems necessary to reach a stable orbit around Mars and also did not include conventional scientific payloads. A 16U is considered therefore a more logical option to accommodate the necessary subsystems for a science mission to Mars.

MARIO is conceived with a 2x2x4U structure. The solar panels have a surface of 6x4U each. It will be assumed that the two panels and the 2x2U base conform the largest cross-sectional area of the spacecraft. Assuming a size of 10 cm x 10 cm for each unit, the surface area of the spacecraft will thus be $0.52\,\mathrm{m}^2$. The estimated mass for MARIO is 26.47 kg, or 29.9 kg including a 20% system margin [4]. A mass of 21 kg will be assumed for the spacecraft after the escape from Earth and heliocentric low-thrust transfer. A new iteration of the capture process with an updated mass figure could be used if necessary. The mass-to-area ratio of the spacecraft will be rounded to $z = 40\,\mathrm{kg/m}^2$.

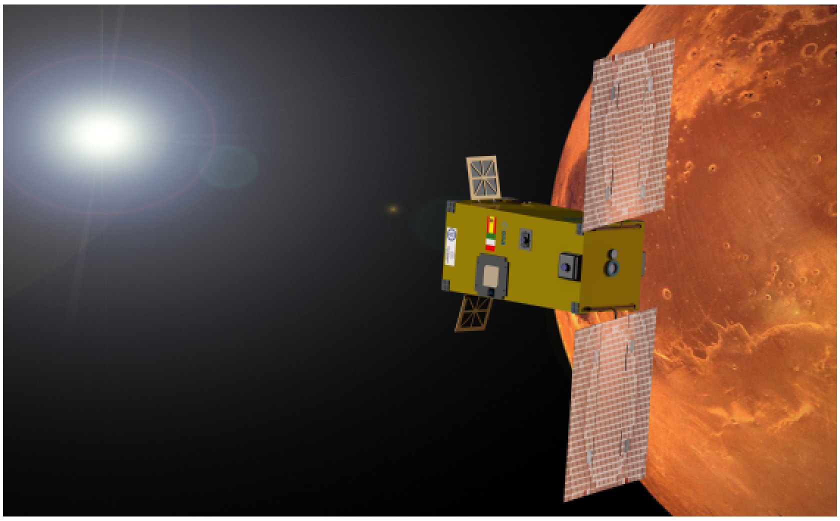

Figure 3.1: Mars Atmospheric Radiation Imaging Orbiter (MARIO) structure and configuration in its orbit around Mars [4].

To be consistent with Cruz Chambel de Aguiar's results [10], a reflectivity of $C_R = 1.1$ will be used, derived from the solar absorptance of the solar cells that comprise most of the cross-sectional area of the spacecraft and which are assumed to be Spectrolab's NeXt Triple Junction (XTJ) Prime [1]. The reflectivity coefficient and the mass-to-area ratio will be the two spacecraft parameters used if SRP is included in the model.

The science objective of the mission is not fixed since it a priori does not affect the characteristics of the mission. However, an areostationary orbit where the spacecraft remains stationary over a location on the Martian surface is a very convenient option for a great number of applications. Robotic devices already present on the surface of Mars and potential human settlings in the future will likely require constant communication with Earth as well as monitoring of the Martian weather, in particular dust storms which can pose a threat to systems operating on the Red Planet. These are two of the most apparent applications for satellites located in an areostationary orbit. As it was introduced in Section 1.2, for the purpose of this study the target orbit will be assumed to be a circular equatorial orbit with a radius of 20,428 km.

3.3. REFERENCE FRAMES

This Section will introduce the reference frames employed to study the ballistic capture problem. Planetary ephemeris from SPICE, which are used to model the N-body problem, can be retrieved in the Earth Mean Equator and Equinox of J2000 (EME2000) (x_e, y_e, z_e) [29]. In this frame, the XY plane coincides with the mean equator of J2000 and the X-axis points towards the intersection of the mean equator of J2000 with the mean ecliptic plane. The Earth Mean Equator and Equinox of J2000 (EME2000) can be centered at the Earth or any other planetary body. Fig. 3.2 shows the geometry of this reference frame.

However, ballistic capture has traditionally been studied using a non-rotating reference frame that considers the orbital plane of the target body. In particular, the Radial-Tangential-Normal reference frame at Epoch (RTN@Epoch) will be used. This frame is also centered at the target, with z_r perpendicular to the Sun orbital plane and x_r aligned with the Sun-planet line. The transformation to EME2000 can be obtained through the orbital parameters of the Sun at epoch t_0 in the EME2000 frame: inclination i, longitude of the ascending node Ω, argument of periapsis ω and true anomaly f. Considering $\theta = \omega + f$, the transformation matrix is:

---

[1] See `https://www.spectrolab.com/DataSheets/cells/XTJ_Prime_Data_Sheet_7-28-2016.pdf` (accessed 13/03/2019)

$$\begin{pmatrix} x_e \\ y_e \\ z_e \end{pmatrix} = \begin{bmatrix} \sin\theta\sin\Omega\cos i - \cos\theta\cos\Omega & \sin\theta\cos\Omega + \cos\theta\sin\Omega\cos i & \sin\Omega\sin i \\ -\cos\theta\sin\Omega - \sin\theta\cos\Omega\cos i & \sin\theta\sin\Omega - \cos\theta\cos\Omega\cos i & -\cos\Omega\sin i \\ -\sin\theta\sin i & -\cos\theta\sin i & \cos i \end{bmatrix} \begin{pmatrix} x_r \\ y_r \\ z_r \end{pmatrix} \tag{3.1}$$

However, the resulting trajectories can be better analyzed on the Barycentric Pulsating Rotating Frame (BPR) (x, y, z)). This reference frame is centered at the system barycenter, the x-axis rotates with the Sun-planet line and the z-axis is aligned with the system angular momentum. The Sun-planet distance is scaled to one, and, when planetary eccentricity is considered, the reference frame indeed pulsates as this distance varies [17].

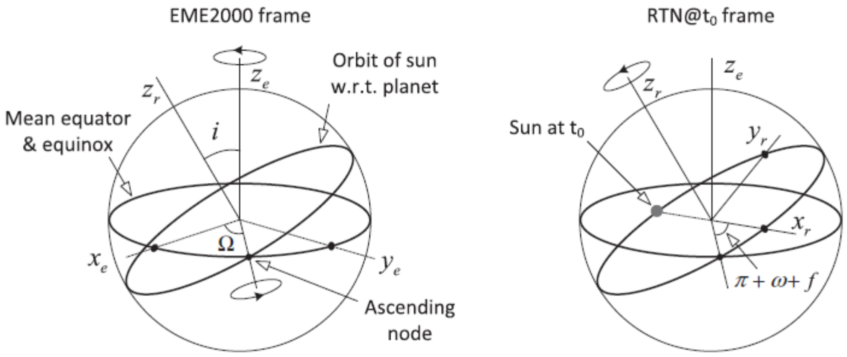

Figure 3.2: Geometry of the EME2000 (left) and Radial-Tangential-Normal reference frame at Epoch (RTN@Epoch) (right) reference frames [19].

Finally, a Mars-fixed rotating frame should be defined in case NSG is included in the dynamics of the problem. The one used will be known as the IAU-Mars frame, after the International Astronomical Union (IAU), and is already available in SPICE. The Z axis will be aligned with Mars rotational axis and will point towards the North, and the X axis will point to Mars' prime meridian.

3.4. SPACECRAFT DYNAMICS AND EQUATIONS OF MOTION

As stated on Section 2.2, an N-body ephemeris model will be used to model the dynamics of the ballistic capture process. The eccentricity of Mars in its orbit around the Sun introduces a very important perturbation, and the gravitational attraction of other planetary bodies seems to favor capture according to literature [19]. However, simpler models will also be explored, in particular the Circular Restricted Three-Body Problem (CRTBP) and Elliptic Restricted Three-Body Problem (ERTBP).

The equations of motion of both the CRTBP and ERTBP are as follow:

$$\ddot{\boldsymbol{r}} = -\frac{\mu_t}{r^3}\boldsymbol{r} - \mu_S\left(\frac{\boldsymbol{r_S}}{r_S^3} + \frac{\boldsymbol{r} - \boldsymbol{r_S}}{||\boldsymbol{r} - \boldsymbol{r_S}||^3}\right) \tag{3.2}$$

where $\boldsymbol{r}$ and $\boldsymbol{r_S}$ are the position vectors of the spacecraft and the second primary (the Sun) with respect to the target, and μ_t and μ_S are the gravitational parameters of the target and the Sun, respectively. The position of the Sun in the RTN@Epoch frame is computed with the following expression, with $e_M = 0$ when using the CRTBP model.

$$\boldsymbol{r_S} = \left[-\frac{a_M(1-e_M^2)}{1+e_M\cos f_M}\cos f_M, -\frac{a_M(1-e_M^2)}{1+e_M\cos f_M}\sin f_M, 0\right] \tag{3.3}$$

where a_M, e_M and f_M are respectively the semi-major axis, eccentricity and true anomaly of Mars in its orbit around the Sun.

The computation of Mars' true anomaly will depend on the model used. For the CRTBP, it is quite straightforward as it is equal to the mean anomaly M_M:

$$\theta_M = M_M = M_{M_0} + n(t - t_0) \tag{3.4}$$

which is computed with the initial mean anomaly at t_0, M_{M_0}, and the mean motion of Mars in its orbit, n.

Meanwhile, for the ERTBP, it is necessary to first obtain the eccentric anomaly E_M from the mean anomaly by numerically solving Kepler's Equation:

$$M_M = E_M - e_M \sin E_M \tag{3.5}$$

From the eccentric anomaly, the true anomaly can be computed as follows:

$$f_M = \text{atan2}\left(\sqrt{1-e_M^2}\sin E_M,\, \cos E_M - e_M\right) \tag{3.6}$$

For the case of a Restricted n-Body Problem (RnBP), where a massless particle (the spacecraft) is under the gravitational attraction of $n-1$ massive bodies, the equations of motion are as follow:

$$\ddot{\boldsymbol{r}} = -\frac{\mu_t}{r^3}\boldsymbol{r} - \sum_{i\in\mathbb{P}} \mu_i \left(\frac{\boldsymbol{r}_i}{r_i^3} + \frac{\boldsymbol{r}-\boldsymbol{r}_i}{||\boldsymbol{r}-\boldsymbol{r}_i||^3}\right) \tag{3.7}$$

where $\boldsymbol{r}_i$ are the position vectors of the perturbing bodies with respect to the target primary, and μ_i are their gravity parameters. The precise states of all the planetary bodies are retrieved as ephemeris data, available in the EME2000 frame from SPICE [29]. In this work, the perturbing bodies included in the set $\mathbb{P}$ will include all the planetary systems except Mars as well as the Sun.

Finally, it is possible to add further perturbations such as Solar Radiation Pressure (SRP) and Non-Spherical Gravity (NSG). SRP can be modeled as follows [30]:

$$\boldsymbol{f_{SRP}} = \frac{Q}{z}\frac{\boldsymbol{r}-\boldsymbol{r_S}}{||\boldsymbol{r}-\boldsymbol{r_S}||^3} \tag{3.8}$$

where the solar pressure constant Q and mass-to-area ratio z are defined as follows:

$$Q = \frac{L_S C_R}{4\pi c} \qquad z = \frac{m}{A} \tag{3.9}$$

where L_S is the luminosity of the Sun, c is the speed of light and C_R, m and A are the reflectivity coefficient, mass and cross-sectional area of the spacecraft, respectively. A constant cross-sectional area will be considered, thus neglecting the orientation of the spacecraft with respect to the Sun. This is typically known as a cannonball model.

Meanwhile, modeling the Non-Spherical Gravity (NSG) of Mars instead of considering it a point mass can also benefit capture. The following equations model the deviations with respect to the single point model [26]:

$$\begin{aligned} \boldsymbol{f_{NSG}} &= -R \cdot \vec{\nabla} U_{NSG} \\ U_{NSG} &= -\frac{\mu_M}{r} \sum_{n=2}^{n_{max}} \sum_{m=0}^{n} (R_M)^n \bar{P}_{nm}(sin\phi) \left[\bar{C}_{nm} \cos(m\lambda) + \bar{S}_{nm} \sin(m\lambda) \right] \end{aligned} \tag{3.10}$$

where:

- R is a transformation matrix between the Mars-centered rotating frame and the EME2000 defined in Section 3.3.
- U_{NSG} is the non-spherical gravity potential function.
- R_M is the radius of Mars.
- r, ϕ, θ are the spherical coordinates of the spacecraft relative to the IAU-Mars rotating frame.
- $\bar{P}_{nm}$ is the normalized Legendre function of the first kind with degree n and order m. An expression for this function can be found in [26].
- $\bar{C}_{nm}$ and $\bar{C}_{nm}$ are the normalized coefficients of Mars non-spherical gravity field, retrieved from the MRO120D gravity model.

Both the SRP and NSG forces can then simply be added to the right-hand side of Equation (3.7) completing a high-fidelity ephemeris model.

3.5. CLASSIFICATION ALGORITHM

The classification algorithm is arguably the most important part of the methodology employed to generate capture sets. Once the initial conditions are integrated, it is necessary to have a robust algorithm that classifies them into the different sets outlined on Section 2.2. The algorithm used will be inherited from the work of Luo et al. [17]. First, the concept of escape, required to define the unstable set X_n, will be introduced.

Two terms have to be defined first:

- The specific Keplerian energy of the spacecraft with respect to Mars:

  $$\varepsilon \equiv \frac{v^2}{2} - \frac{\mu_m}{r} \tag{3.11}$$

  where r and v are the norm of the position and velocity of the spacecraft in a non-rotating reference frame at Mars.

- The radius of the SOI of Mars with respect to the Sun:

  $$R_{SOI_M} \equiv a_M \left(\frac{\mu_M}{\mu_S} \right)^{\frac{2}{5}} \tag{3.12}$$

  where a_M is the semi-major axis of the Martian orbit around the Sun.

A spacecraft is said to escape from the central body at time t_e if

$$\varepsilon(t_e) > 0 \quad \wedge \quad r(t_e) > R_{SOI_M} \tag{3.13}$$

that is, if both the following conditions occur at the same time:

- The spacecraft leaves the SOI of the target, and
- The spacecraft Keplerian energy with respect to the target is positive.

Impact with a planetary body, at time t_{crash} is modeled with the following condition:

$$||\boldsymbol{r} - \boldsymbol{r_i}|| < R_i \tag{3.14}$$

where $\boldsymbol{r_i}$ is the position of the planetary body and R_i is its radius.

A third required definition is that of a revolution around the target. In three-dimensional space, it is necessary to define a semi-plane to determine these revolutions. This intersection plane will be the one defined by the initial position and angular momentum of the spacecraft around the target, which can be seen on Fig. 3.3.

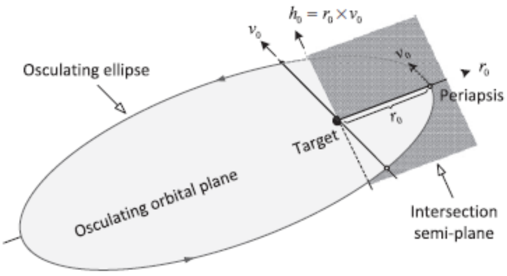

Figure 3.3: Geometry of the intersection plane used in the three-dimensional algorithmic definition of the stable sets [19].

The spacecraft will perform its k-th revolution around the target when the following three conditions are met simultaneously at time t_k:

- The particle returns to the intersection plane: $\boldsymbol{r}^{(k)}(t_k) \cdot (\boldsymbol{h}_0 \times \boldsymbol{r}_0) = 0$
- Only the relevant semi-plane, the one that includes the periapsis, is considered: $\boldsymbol{r}^{(k)}(t_k) \cdot \boldsymbol{r}_0 > 0$
- An additional condition is used to prune out cases when the spacecraft returns to the semi-plane without performing a complete revolution. A complete revolution takes place when the spacecraft crosses the semi-plane in the same direction of motion as it did the previous time: $(\boldsymbol{v}^{(k)}(t_k) \cdot \boldsymbol{v}_0)(\boldsymbol{v}^{(k-1)}(t_k) \cdot \boldsymbol{v}_0) > 0$

The following equation sums up the definition of a revolution:

$$\boldsymbol{r}^{(k)}(t_k) \cdot (\boldsymbol{h}_0 \times \boldsymbol{r}_0) = 0 \quad \wedge \quad \boldsymbol{r}^{(k)}(t_k) \cdot \boldsymbol{r}_0 > 0 \quad \wedge \quad (\boldsymbol{v}^{(k)}(t_k) \cdot \boldsymbol{v}_0)(\boldsymbol{v}^{(k-1)}(t_k) \cdot \boldsymbol{v}_0) > 0 \tag{3.15}$$

Finally, a maximum integration time Δt_{max} is defined as four periods of a circular orbit with a radius that of the SOI:

$$\Delta t_{max} = 4 \cdot 2\pi \sqrt{\frac{R^3_{SOI_M}}{\mu_M}} \tag{3.16}$$

With these four concepts, the weakly stable set $\mathscr{W}_n$, unstable set $\mathscr{X}_n$, crash set $\mathscr{K}_n$ and acrobatic set $\mathscr{D}_n$, as defined on Section 2.2, can be populated.

3.6. COMPUTATIONAL IMPLEMENTATION

This Section will discuss some aspects regarding the actual computational implementation of the methodology outlined during this Chapter. The ballistic capture leg of the trajectory will be studied with *MATLAB* tool GRAvity TIdal Slide (GRATIS). GRATIS was developed for the study conducted in [17] and has since been updated in several occasions [10, 21]. Without diving into details of the actual code conforming GRATIS, some aspects that are important for its performance will be introduced in this Section.

It is well-known that computers use finite-precision floating-point arithmetics, what leads to a loss of significance when performing arithmetic operations that escalates over time. It is important to minimize this error by using an adequate implementation of the dynamics of the problem. Perhaps one of the most important things to take into account in this sense is the selection of the Center of Integration (COI), which should be the body that offers a smoother evolution of the spacecraft trajectory [30]. This will typically be the dominant body, i.e. Mars in the case that is being studied in this Chapter since the spacecraft is generally within its SOI.

After selecting the target body as COI, it should be noted that the equations of motion of the Restricted n-Body Problem (RnBP) shown in (3.7) include for every perturbing body a difference of the form

$$\frac{\boldsymbol{r_i}}{r_i^3} - \frac{\boldsymbol{r_i} - \boldsymbol{r}}{||\boldsymbol{r_i} - \boldsymbol{r}||^3} = \frac{\boldsymbol{p}}{p^3} - \frac{\boldsymbol{d}}{d^3} \tag{3.17}$$

Both terms in this difference, the position of body i with respect to the central body and the position of body i with respect to the spacecraft, are very similar, since the spacecraft will always be in the vicinity of the central body in the context of ballistic capture. Subtracting two very similar values leads to a large rounding error and a loss of significance [30]. To avoid this, it is possible to replace (3.17) by the following expression [31]

$$\frac{1}{d^3}\left(q\frac{3+3q+q^2}{1+(1+q)^{\frac{3}{2}}}\boldsymbol{p} + \boldsymbol{b}\right) \qquad \boldsymbol{b} \equiv \boldsymbol{p} - \boldsymbol{d} \qquad q \equiv \frac{\boldsymbol{b}\cdot(\boldsymbol{b} - 2\boldsymbol{p})}{\boldsymbol{p}\cdot\boldsymbol{p}} \tag{3.18}$$

Indeed, this expression includes many more operations than (3.17), so an increased computational time will be the price to pay to avoid a loss of significance.

Numerical integration is performed with *MATLAB*'s built-in *ode113*, an explicit variable order integrator of the Adams schemes family particularly suitable for non-stiff ODE's. A trade-off between different *MATLAB* built-in ODE solvers was conducted in [10] where it was determined that *ode113* performs well during the study of ballistic capture with Restricted n-Body Problem (RnBP) dynamics. A study of this nature will not be repeated here and thus this integrator will still be used in GRATIS without diving into more detail.

Another important aspect of the computational implementation of ballistic capture in GRATIS is the use of dimensionless variables. The scaling variables are the following:

- **Length Unit:** $LU = R_M$ (radius of the central body)
- **Gravitational Parameter Unit:** $\frac{LU^3}{TU^2} = \mu_M$ (grav. parameter of the central body)
- **Time Unit:** $TU = \sqrt{\frac{LU^3}{\mu_M}}$ (approx. 16 min for the case of Mars)

Finally, there are two important computational tools used by GRATIS worth mentioning. The first one is the *SPICE* Toolkit developed by the Navigation and Ancillary Information Facility (NAIF) at the Jet Propulsion Laboratory (JPL). This Toolkit consists of a great number of Application Program Interfaces (API's) that will be used by GRATIS to define different reference frames and perform transformations between them, and to obtain ephemeris data of planetary bodies in the Solar System.

The other important tool that will be used by GRATIS is parallel computing, which is natively implemented in *MATLAB* with its Parallel Computing Toolbox. In GRATIS, it will be used in the construction of capture sets to integrate several initial conditions simultaneously, since they are completely independent from each other.

4

VERIFICATION AND RESULTS

4.1. INTRODUCTION

The goals of this Chapter are two-fold: first, the methodology described in Chapter 3 to generate capture sets will be verified in Section 4.2. Then, the results obtained will be presented in the following Sections. Section 4.3 will show the influence of the dynamical model in the capture sets generated. Once a decision on the dynamics to be used is made, Section 4.4 will present the capture sets at Mars generated for different epochs that will be targeted in Part VI and stabilized in Part V.

4.2. VERIFICATION

CONSTRUCTION OF CAPTURE SETS

The classification algorithm and the capture definitions described in Section 3.5 will be verified by testing the generation of a capture set and comparing it with results available in literature. In particular, the results obtained for Mars when using the ephemeris model in Table 2.1 will be reproduced. The initial grid used in Luo & Topputo [19] to generate this set is shown in Table 4.1.

Table 4.1: Initial conditions used for the verification of the construction of a capture set at Mars using a RnBP ephemeris model.

Orbital parameter	**Value**
Eccentricity	$e_0 = 0.95$
Longitude of the ascending node	$\Omega_0 = 0°$
Inclination	$i_0 = 0°$
Argument of periapsis	$\omega_0 = 0° : 1° : 359°$
Radius of periapsis	$r_{p_0} = 600$ points, from $R_M + 1\,\text{km}$ to R_{SOI}
Mean anomaly	$M_0 = 0°$
Initial epoch	$t_0 = 08/\text{May}/2024$ 12:36:08.640 UTC

The orbit with a minimum stability index, along with the value of this minimum stability index and of the capture ratio are compared with those provided in Table 2.1. Table 4.2 shows the comparison of the minimum stability index and capture ratio, which are both identical.

Table 4.2: Comparison of the characteristics of the $\mathscr{C}^6_{-1}$ capture sets obtained at Mars with the instance of GRATIS used in this work and in [19].

Parameter	**Luo & Topputo [19]**	**GRATIS**
Capture ratio	0.315‰	0.3148‰
Min. Stability Index	10,143 TU	10,143 TU

Fig. 4.1 shows the trajectory of the capture with minimum stability index, which can be compared with the one shown in Fig. 2.1 for the case of Mars. From a qualitative point of view, both orbits also look identical.

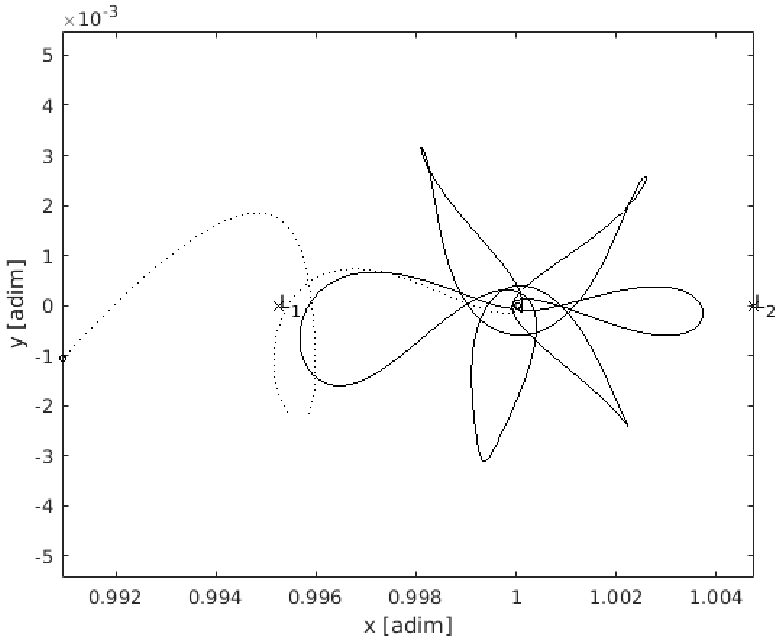

Figure 4.1: Trajectory of the capture with the minimum stability index in the verification capture set, in the BPR reference frame.

4.3. INFLUENCE OF THE DYNAMICS IN THE CAPTURE SETS

A specific capture set will be studied in this Section under the influence of several different dynamics models, in order to determine the influence of the dynamics in the capture process. The capture set in particular will be defined by the grid of initial conditions described in Table 4.3. The initial epoch t_0 corresponds to Mars being at the perihelion of its orbit. The capture grid employed includes 145,080 initial conditions to propagate.

Four different models will be used to generate this capture set:

- The Circular Restricted Three-Body Problem (CRTBP).
- The Elliptic Restricted Three-Body Problem (ERTBP), including Mars' planetary eccentricity of $e = 0.0935$.

Table 4.3: Initial conditions used for the study of the influence of the dynamics in the ballistic capture sets.

Orbital parameter	**Value**
Eccentricity	$e_0 = 0.99$
Longitude of the ascending node	$\Omega_0 = 0°$
Inclination	$i_0 = 0°$
Argument of periapsis	$\omega_0 = 0° : 1° : 359°$
Radius of periapsis	$r_{p_0} = R_M + 250\,\text{km} : 50\,\text{km} : 7R_M$
Mean anomaly	$M_0 = 0°$
Initial epoch	$t_0 = 08/\text{May}/2024$ 12:36:08.640 UTC

- A Restricted n-Body Problem (RnBP), including the gravitational acceleration of all planetary systems in the Solar System and the Sun. This will be referred to as *Ephemeris model 1*.
- An extension of the RnBP above, including Solar Radiation Pressure (SRP) and Non-Spherical Gravity (NSG) up to degree and order 5. This will be referred to as *Ephemeris model 2*.

An extensive study of the effect of SRP and NSG on the capture sets generated with GRATIS was conducted in [10]. This will not be repeated here, and NSG with degree and order 5 will be used as a compromise between accuracy and computational effort. Both SRP and NSG had a small but not negligible positive effect on the characteristics of the capture set, what will now be reproduced here.

Fig. 4.2 shows the capture sets generated with all four models described above. It can be seen how the CRTBP fails to find most of the captures present in the other three models, suggesting at a first glance that the circular model is probably too simplistic. On the other hand, Fig. 4.3 shows the capture in each capture set that presents a lower stability index and can therefore be considered the most regular one.

Finally, Table 4.4 shows a comparison of the different indexes used to characterize the capture sets, in particular the minimum stability index S_{min}, the capture ratio R_c and an interesting measure $N_{S_{th}}$, defined in [10] as the number of elements with a stability index lower than a certain threshold. For the sake of consistency, the threshold value considered will be $S_{th} = 15000\,\text{TU}$. This parameter will give a sense of how many regular ideal trajectories are present in the capture set. The computational time required to generate the sets is also presented, when using 12 workers for all simulations.

Table 4.4: Characteristics of the capture sets obtained with the four different dynamical models employed.

Model	**# captures**	R_c **[%]**	$S_{min}[TU]$	$N_{S_{th}}$	**Comp. time [hr]**
CRTBP	52	0.0358%	14060.22 TU	1	1.64 hr
ERTBP	243	0.1675%	12249.56 TU	5	5.07 hr
Ephem. 1	242	0.1668%	12200.77 TU	4	4.12 hr
Ephem. 2	241	0.1661%	11943.11 TU	5	17.7 hr

It can be seen how the capture set obtained when using the CRTBP is much smaller, confirming the hypothesis that introducing the eccentricity of Mars' orbit is necessary to study the problem. The differences between the other three models are not very large. The second ephemeris model, including SRP and NSG, leads to a slightly lower number of captures but a priori more stable, with a lower minimum stability index. However, the computational time is around four times longer than when only including third-body perturbations. These results do not agree completely with those found in [10], where NSG and SRP and the gravity of additional planets increased slightly the number of captures. The differences are in any case small, and for the

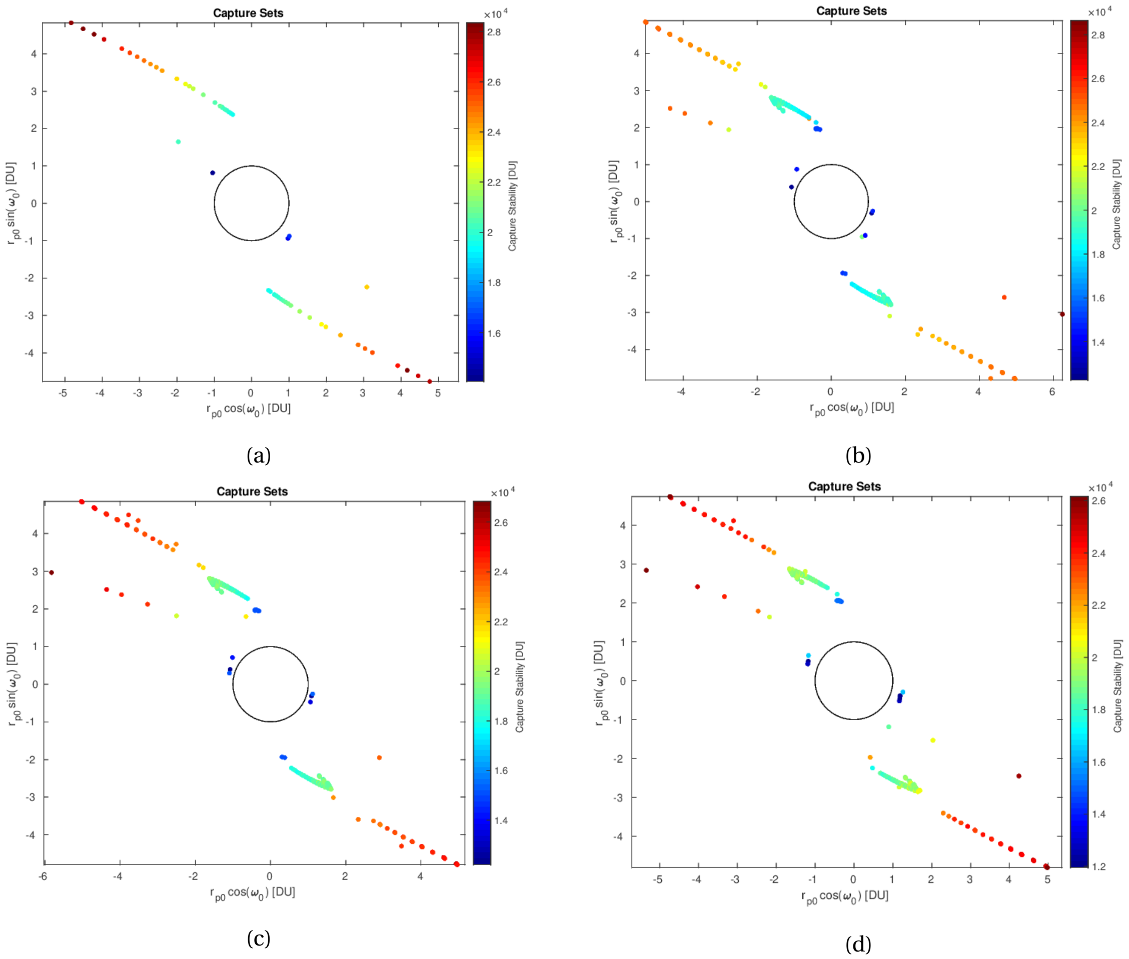

(a) (b) (c) (d)

Figure 4.2: Capture sets $\mathscr{C}^1_{-6}$ at Mars with initial conditions specified in Table 4.3, using the following dynamics models: a) CRTBP, b) ERTBP, c) Ephemeris model 1, d) Ephemeris model 2. The capture sets are colored by the capture stability index, and the black circle with radius 1 DU represents the surface of Mars.

remainder of this Chapter the first ephemeris model will be used, as a compromise between computational expenses and accuracy.

4.4. CAPTURE SETS TO TARGET

In this Section, and as stated before, the first ephemeris model described in the previous Section (*Ephemeris Model 1*) will be used to generate capture sets for different epochs at Mars.

Perhaps the most important aspect to take into account for the generation of the capture set is the choice of initial conditions to construct the grid. As described in Section 2.2, it is common to use a grid on the argument of periapsis and the radius of periapsis, leaving the remaining orbital elements fixed. This approach will also be followed in this work.

The eccentricity will be made equal to $e_0 = 0.99$. A very high value of the eccentricity is required for capture to occur, and higher values will lead to closer periapsis passages and generally more regular captured trajectories [19], as well as a faster stabilization of the orbit as will be explored in Chapter 8.

The target orbit is as stated before an areostationary orbit, that is, an equatorial orbit around Mars with a

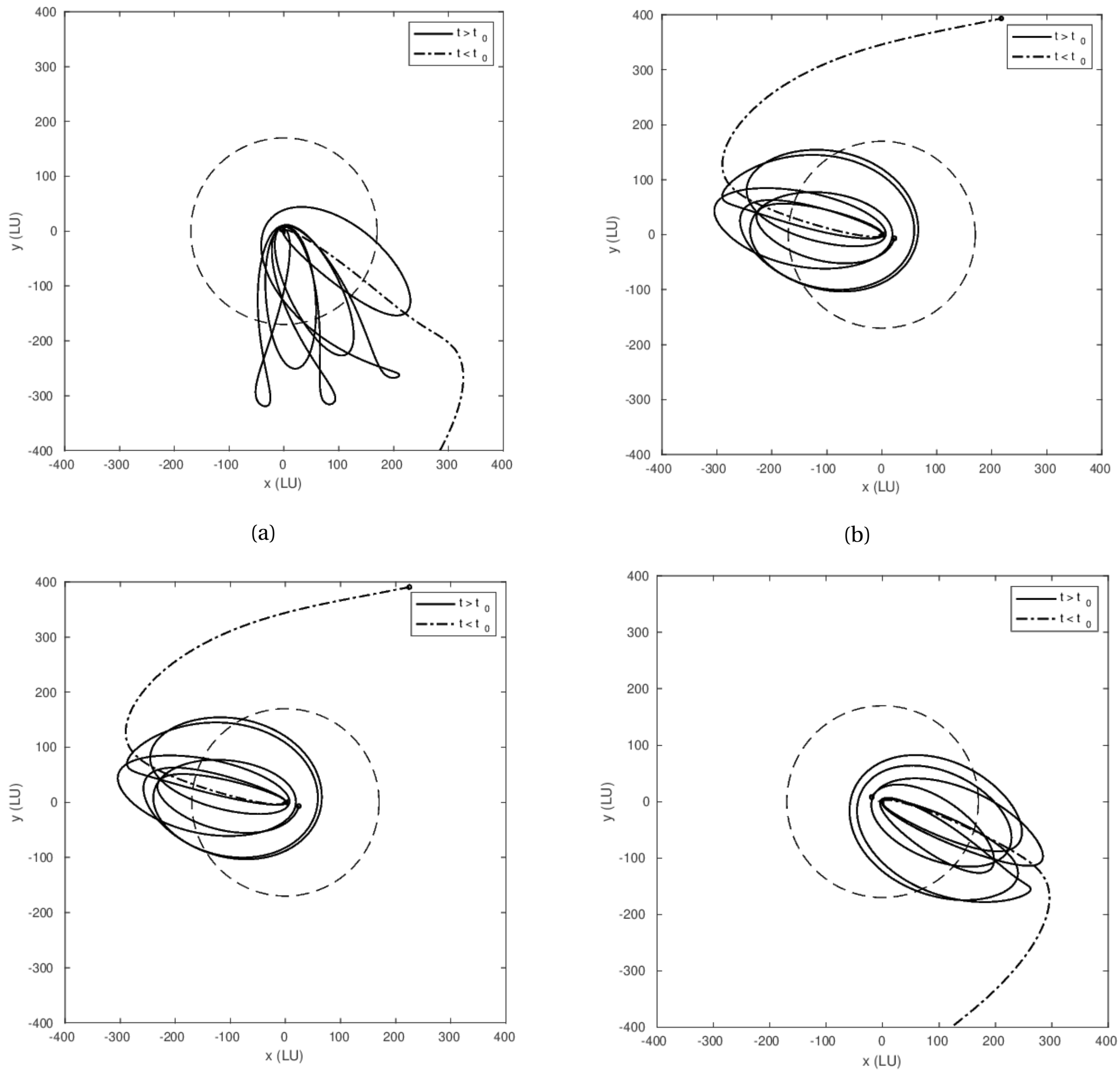

(a) (b)

(c) (d)

Figure 4.3: Trajectory in the RTN@Epoch reference frame of the capture with lower stability index of the capture sets in Fig. 4.2, for the following dynamics models: a) CRTBP, b) ERTBP, c) Ephemeris model 1, d) Ephemeris model 2. The dashed circle represents the SOI of Mars.

radius of 20,428 km. The osculating orbital elements defined in this Section that will describe the initial state of the captures are expressed in the RTN@Epoch reference frame, which has no relation with the equatorial plane of Mars. For this reason, it is interesting to determine the combination of longitude of ascending node Ω_0 and inclination i_0 in the RTN@Epoch frame that corresponds to an areostationary orbit.

Fig. 4.4 shows both the ecliptic plane, which corresponds with the x-y plane in the RTN@Epoch reference frame, and the equatorial plane, defined by the Equator of Mars and where an areostationary orbit would be contained. The longitude of ascending node and inclination define the relation between both planes at the initial epoch t_0.

The direction of the rotational axis of Mars at t_0 can be retrieved from SPICE and the inclination and longitude of the ascending node of an equatorial orbit can then be quickly computed using the definition of these orbital elements that can be seen in Fig. 4.4. Fig. 4.5 shows the value of i_0 and Ω_0 during the 800-days

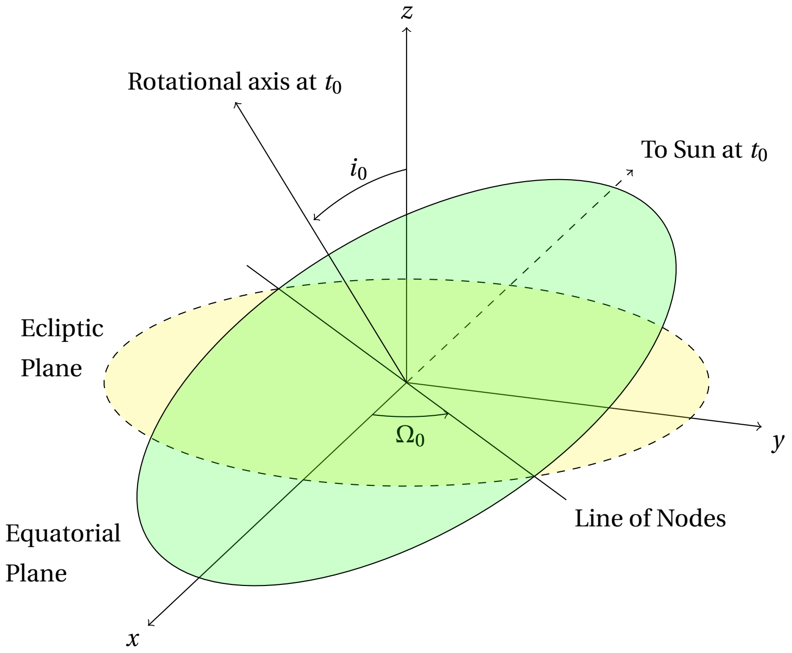

Figure 4.4: Orientation of the equatorial and ecliptic planes at the initial epoch, and relation between them with the inclination i_0 and longitude of the ascending node Ω_0.

period considered in this Section. As expected the inclination barely varies, with a change of only 0.0005° in the roughly two-year time span considered. The longitude of the ascending node on the other hand varies almost linearly (with deviations mostly due to the orbital eccentricity of Mars) completing a 360° cycle every 687 days, which is the orbital period of Mars around the Sun.

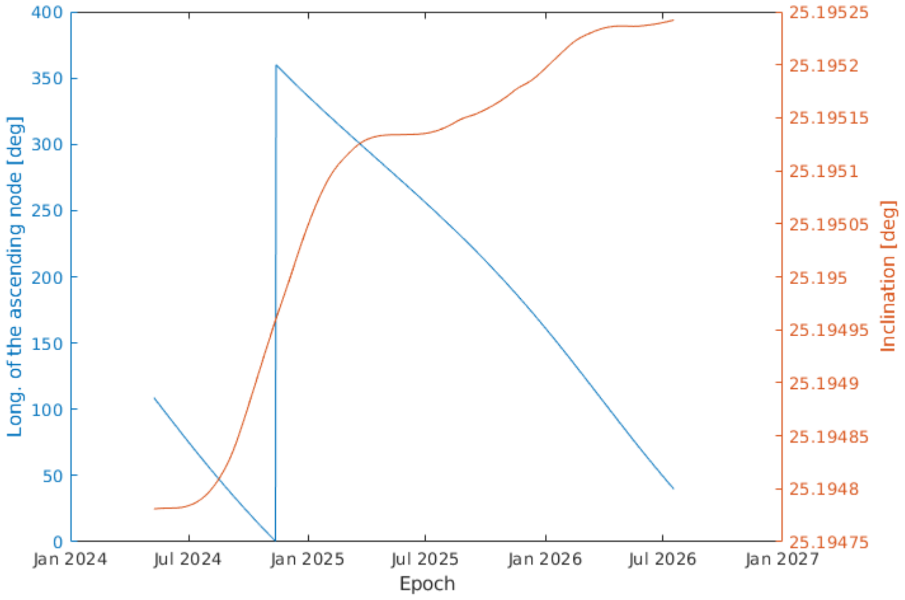

Figure 4.5: Longitude of the ascending node (left axis) and inclination (right axis) of an areostationary orbit in the RTN@Epoch reference frame for different epochs.

In order to make the stabilization of the capture into an areostationary orbit potentially easier, the combination of i_0 and Ω_0 generated above for each epoch will be used to characterize each capture set. As an interesting side effect, and according to Fig. 2.1, the inclination of approximately 25° that will be used corresponds to the inclination for prograde orbits where the capture ratio is highest [19].

The argument of periapsis will be surveyed in its entirety, with a one degree resolution from 0° to 359°. The radius of periapsis will take a lower bound of 250 kilometers above the surface of Mars (where the Martian atmosphere is negligible) and an upper bound of 7 times the radius of the planet. It is known that there are captures beyond this upper bound [7, 10], but the stability index of the capture is in general inversely proportional to the altitude at periapsis so only the captures close to the planet will be interesting a priori.

Finally, the epoch will be an important driver for the characteristics of the capture set. The Earth-Mars synodic period, i.e. the time between conjunctions of the Earth and Mars in their orbits around the Sun, is 779.9 days. For this reason, and although other planetary bodies can of course introduce perturbations, the characteristics of Earth-Mars transfers should be roughly periodic every 780 days [10, 26]. An 800-days interval, with a resolution of 50 days, will be used to study the problem. The beginning of this interval will be one of Mars' perihelions, in particular 08/May/2024 12:36:08.640 UTC as retrieved from SPICE.

In summary, the orbital parameters used in this Section are depicted in Table 4.5. This corresponds to 290,160 initial conditions per capture set.

Table 4.5: Initial conditions of the capture sets that will be generated for the mission design targeting an areostationary orbit.

Orbital parameter	**Value**
Eccentricity	$e_0 = 0.99$
Longitude of the ascending node	Varies with t_0: see Fig. 4.5
Inclination	Varies with t_0: see Fig. 4.5
Argument of periapsis	$\omega_0 = 0° : 1° : 359°$
Radius of periapsis	$r_{p_0} = R_M + 250\,\text{km} : 25\,\text{km} : 7R_M$
Mean anomaly	$M_0 = 0°$
Initial epoch	Every 50 days from 08/May/2024 12:36:08.640 UTC to 17/Jul/2026 12:36:08.640 UTC

Table 4.6 shows the characteristics of the capture sets obtained for the different epochs considered. Fig. 4.6 shows the capture set colored by stability index and the capture in this set with the lowest stability index for the first epoch considered, 08/May/2024.

In order to select the capture with the lowest stability index, two important factors should be taken into account. First, and as will be described later, only captures arriving at Mars through the L_1 Lagrangian point will be considered. Besides, the capture sets for some epochs have very long backwards propagation times, suggesting they spend a great amount of time orbiting Mars after entering the SOI and before reaching the first periapsis without completing a revolution as defined by the methodology used. Captures will be targeted in Part VI when they are outside the SOI of Mars and therefore these captures that take up to several hundred days orbiting the planet before the first periapsis would have an extremely long and undesirable ballistic stage after capture. For that reason, orbits with a backwards propagation time inside the SOI of Mars larger than a threshold of 50 days will not be considered in this Section. In Part V, the total time of flight for stabilization into the target science orbit will be the performance measure employed, and that includes the ballistic portion from the first entry into the SOI until the first periapsis.

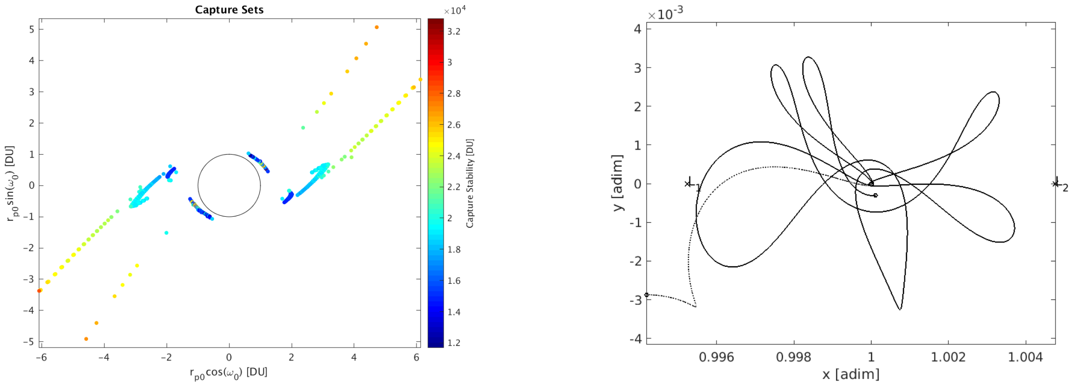

(a) (b)

Figure 4.6: a) Capture set, colored by stability index, and b) trajectory in the BPR reference frame of the capture with lowest stability index, for initial epoch 08/May/2024.

These results are then also shown for the rest of epochs considered in the survey. In particular, Figs. 4.7 and 4.8 show the capture sets, while Figs. 4.9 and 4.10 show the orbit in each capture set that presents a lower stability index.

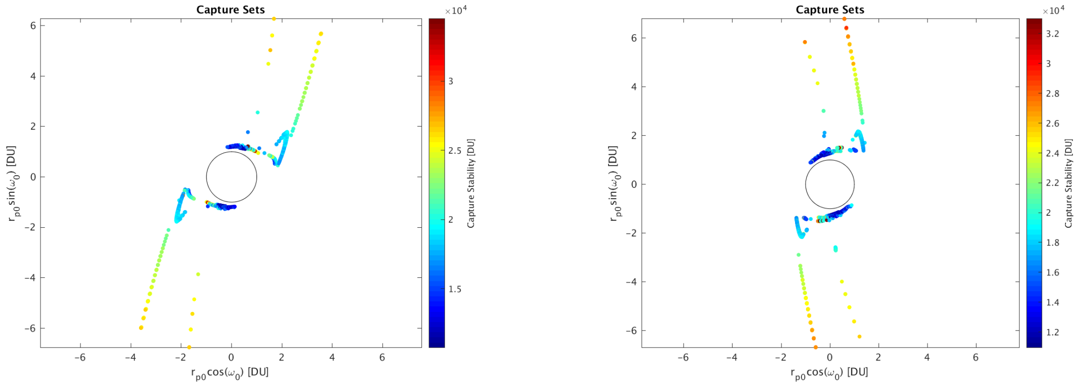

(a) 27/Jun/2024 (b) 16/Aug/2024

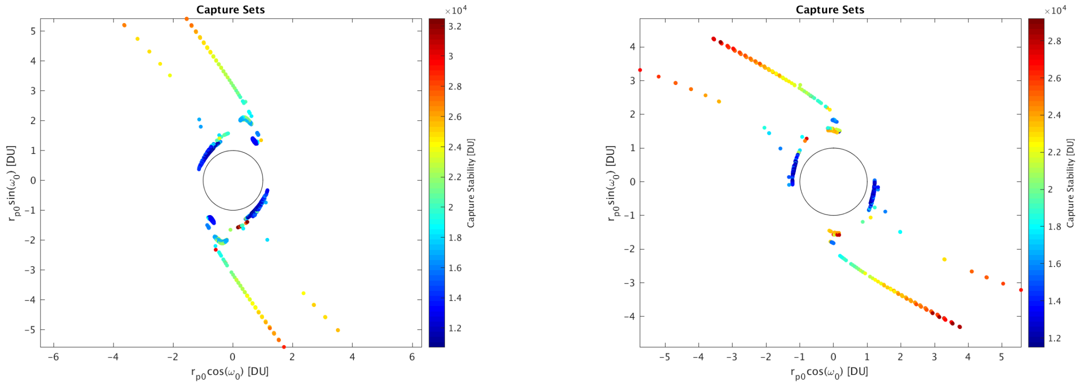

(c) 05/Oct/2024 (d) 24/Nov/2024

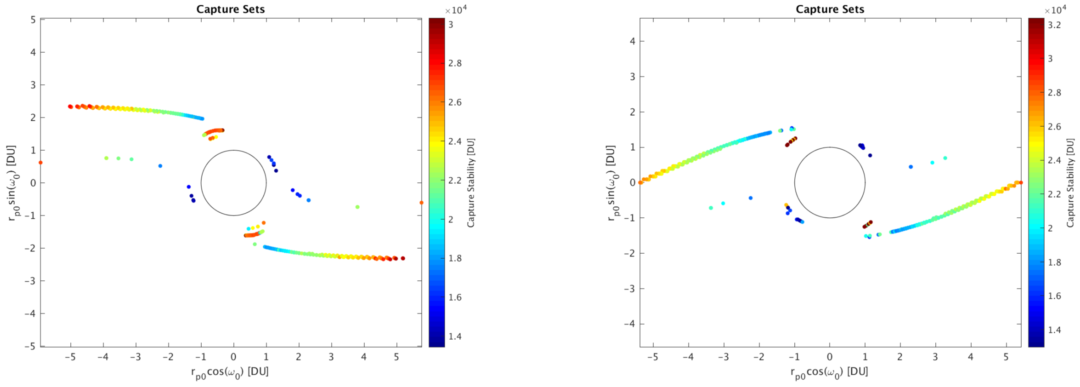

(e) 13/Jan/2025 (f) 04/Mar/2025

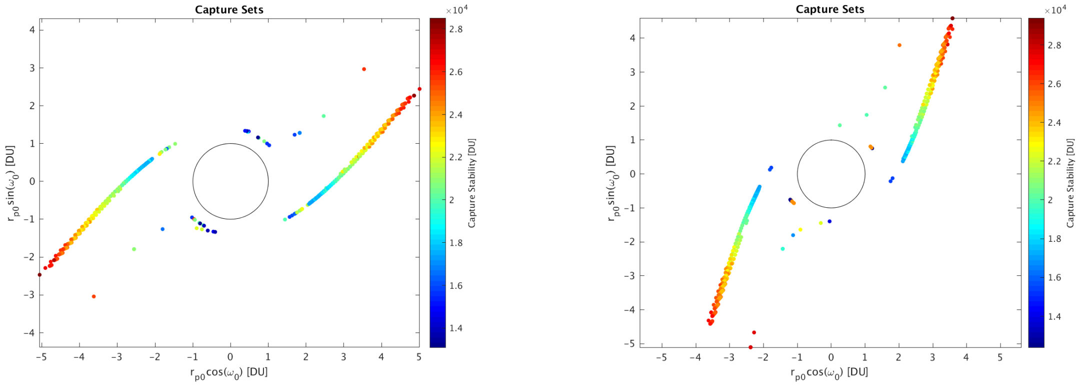

(g) 23/Apr/2025 (h) 12/Jun/2025

Figure 4.7: Capture sets $\mathscr{C}^1_{-6}$ at Mars with initial conditions specified in Table 4.5, for the specified epochs. The capture sets are colored by the capture stability index, and the black circle with radius 1 DU represents the surface of Mars. [Continues on next page]

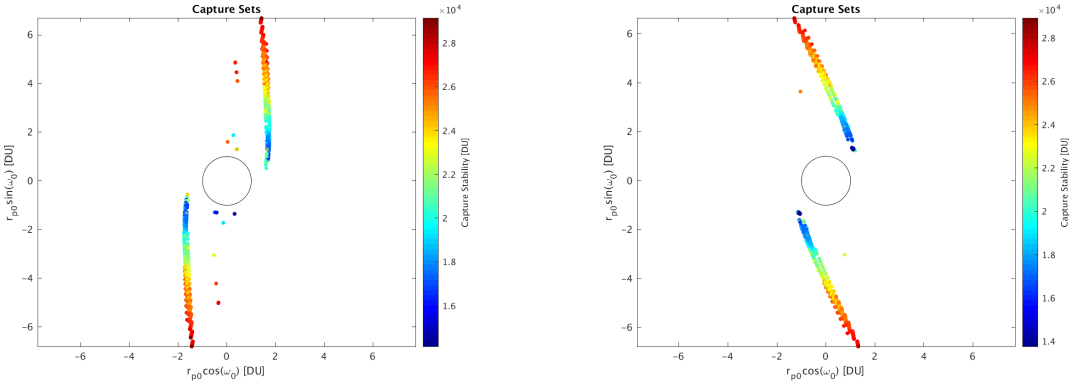

(a) 01/Aug/2025

(b) 20/Sep/2025

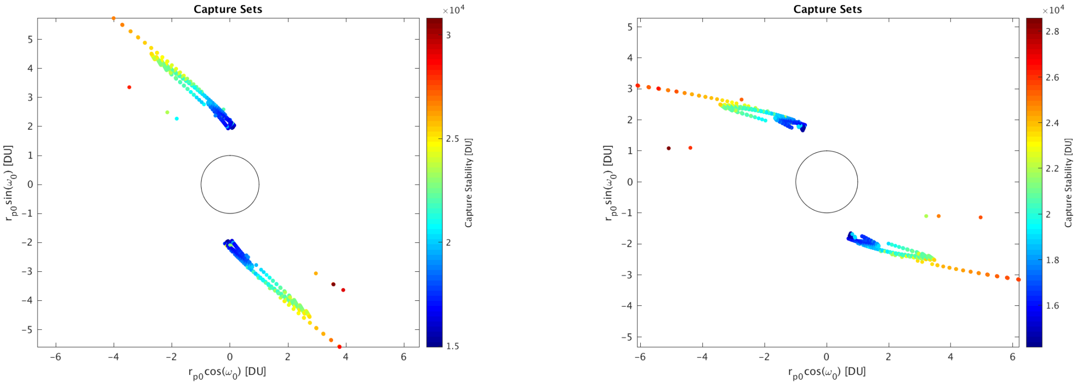

(c) 09/Nov/2025

(d) 29/Dec/2025

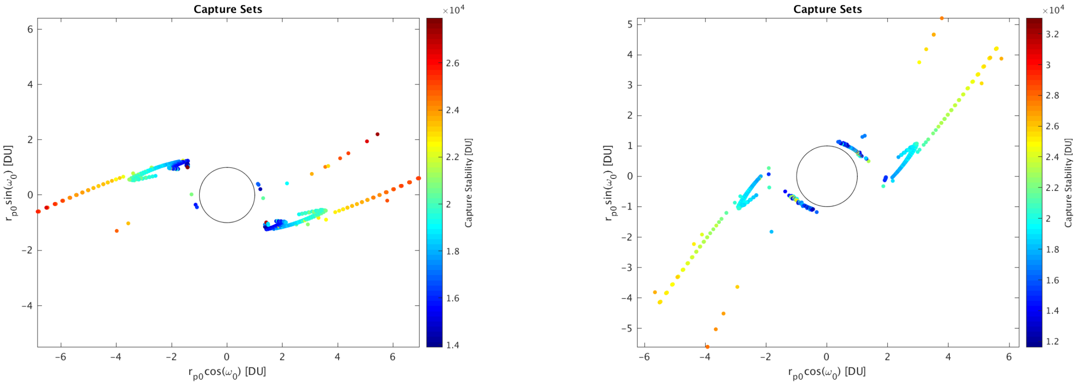

(e) 17/Feb/2026

(f) 08/Apr/2026

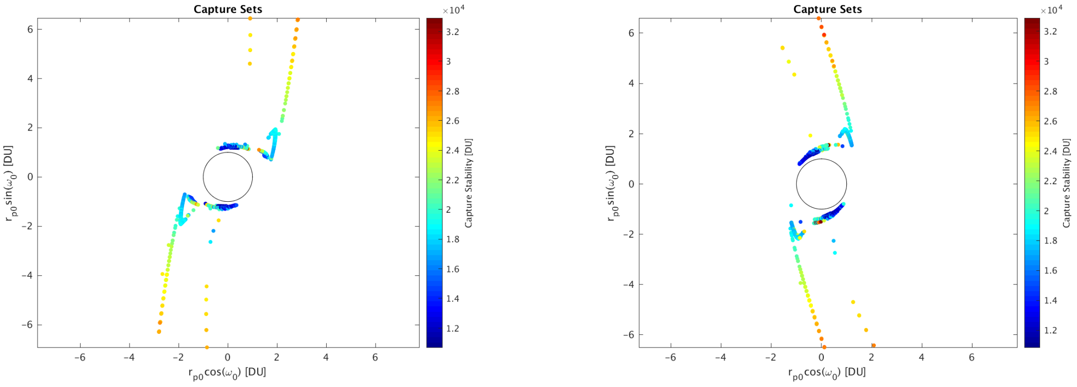

(g) 28/May/2026

(h) 17/Jul/2026

Figure 4.8: Capture sets $\mathscr{C}^1_{-6}$ at Mars with initial conditions specified in Table 4.5, for the specified epochs. The capture sets are colored by the capture stability index, and the black circle with radius 1 DU represents the surface of Mars. [Continues from previous page]

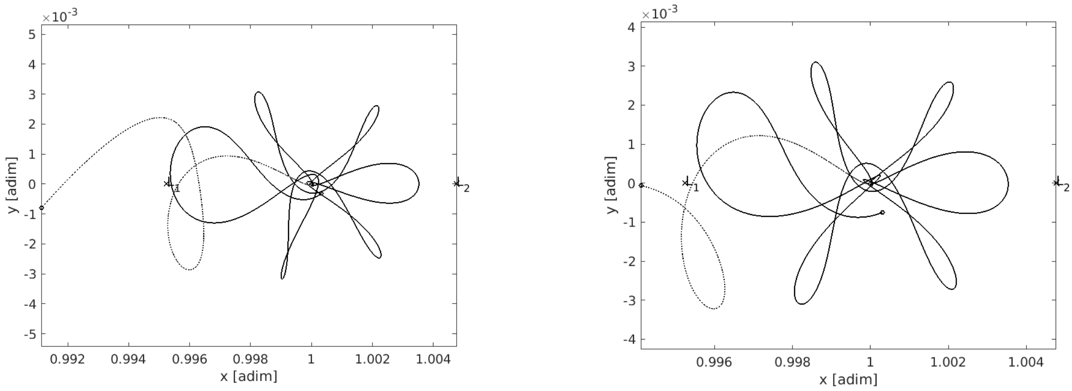

(a) 27/Jun/2024

(b) 16/Aug/2024

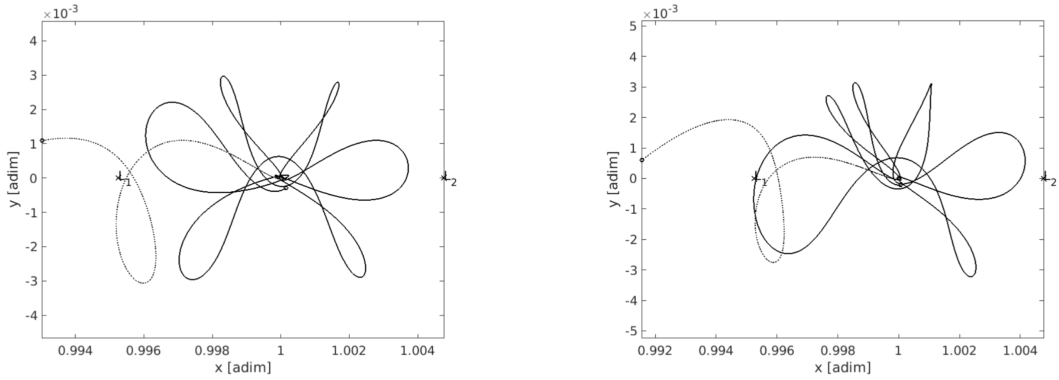

(c) 05/Oct/2024

(d) 24/Nov/2024

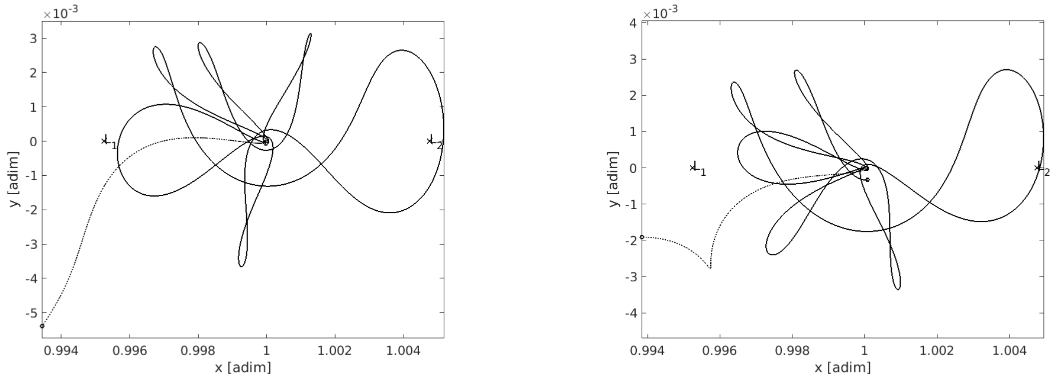

(e) 13/Jan/2025

(f) 04/Mar/2025

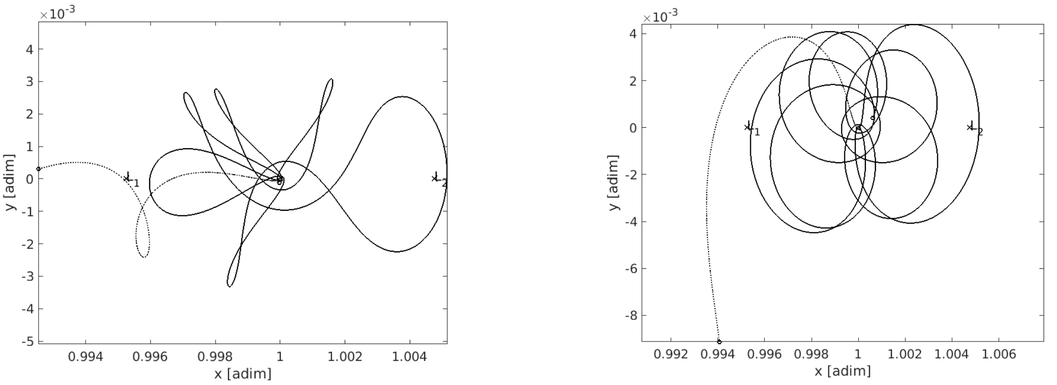

(g) 23/Apr/2025

(h) 12/Jun/2025

Figure 4.9: Trajectory in the BPR reference frame of the capture with lower stability index of the capture sets in Fig. 4.7, for the specified epochs. [Continues on next page]

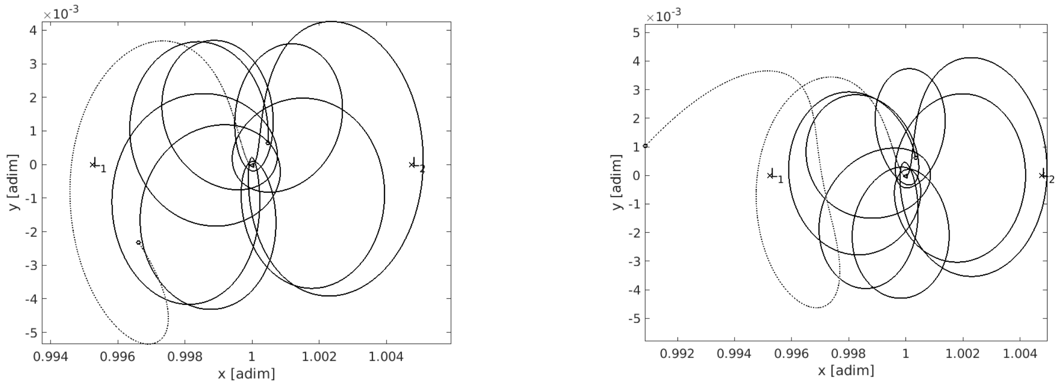

(a) 01/Aug/2025 (b) 20/Sep/2025

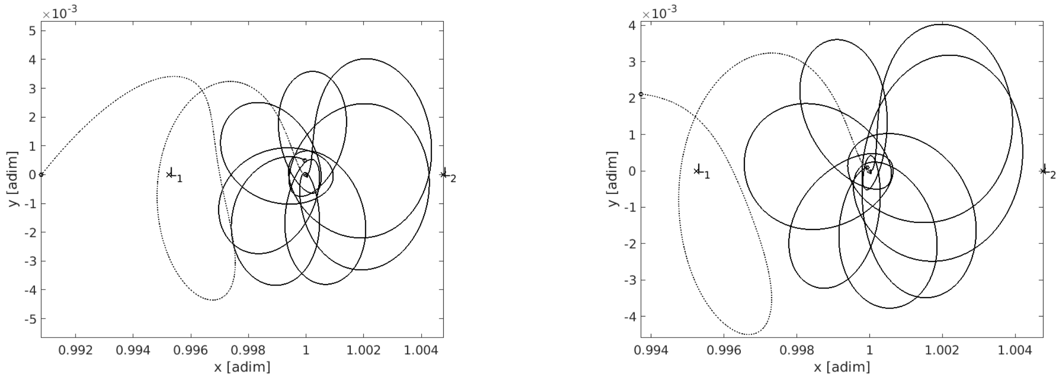

(c) 09/Nov/2025 (d) 29/Dec/2025

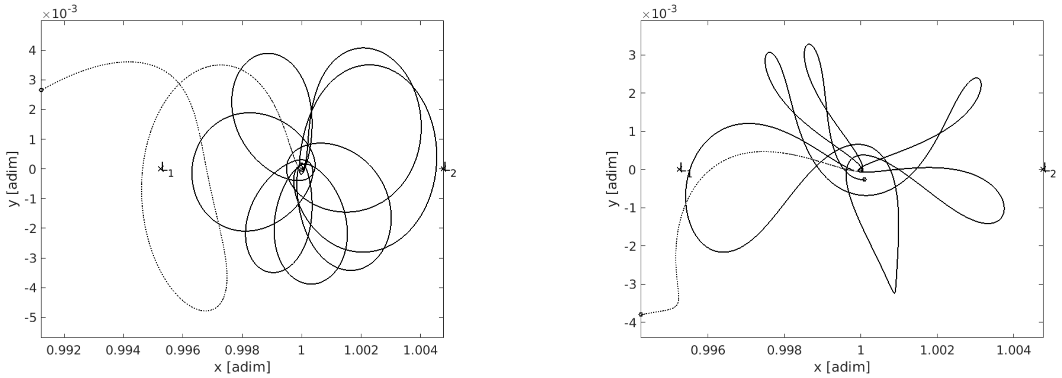

(e) 17/Feb/2026 (f) 08/Apr/2026

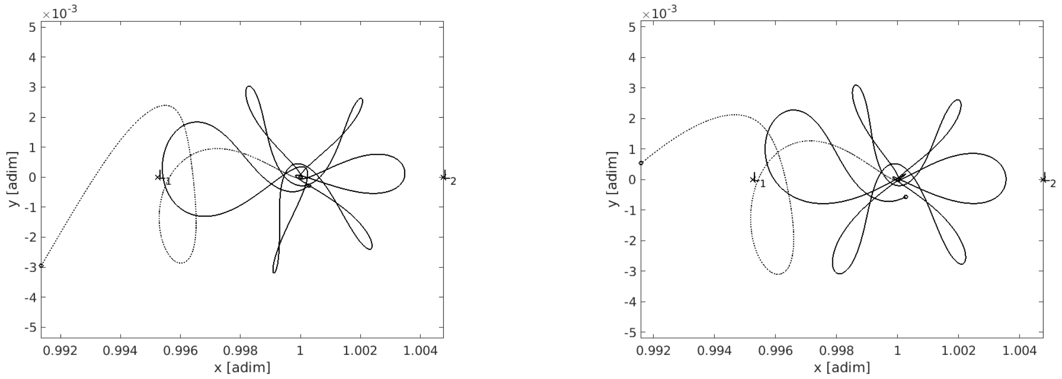

(g) 28/May/2026 (h) 17/Jul/2026

Figure 4.10: Trajectory in the BPR reference frame of the capture with lower stability index of the capture sets in Fig. 4.8, for the specified epochs. [Continues from previous page]

Table 4.6: Characteristics of the $\mathscr{C}^{1}_{-6}$ capture sets obtained for different epochs.

Epoch	e_0	i_0 [°]	Ω_0 [°]	M_0 [°]	N_C	R_c	$N_{S_{th}}$	$S_{min}[TU]$	$\omega_0[°]$	$r_{p_0}[km]$
08/May/2024	0.99	25.195°	108.79°	0°	685	2.361‰	15	11702 TU	229°	4046 km
27/Jun/2024	0.99	25.195°	77.32°	0°	727	2.506‰	70	10760 TU	248°	4121 km
16/Aug/2024	0.99	25.195°	47.31°	0°	829	2.857‰	134	11025 TU	270°	4321 km
05/Oct/2024	0.99	25.195°	19.52°	0°	880	3.033‰	139	10744 TU	299°	4321 km
24/Nov/2024	0.99	25.195°	354.00°	0°	503	1.734‰	70	11520 TU	335°	4221 km
13/Jan/2025	0.99	25.195°	330.32°	0°	483	1.665‰	3	13447 TU	16°	4596 km
04/Mar/2025	0.99	25.195°	307.86°	0°	534	1.840‰	8	12981 TU	51°	4621 km
23/Apr/2025	0.99	25.195°	285.97°	0°	659	2.271‰	3	13091 TU	58°	4646 km
12/Jun/2025	0.99	25.195°	263.99°	0°	830	2.861‰	0	17090 TU	12°	7496 km
01/Aug/2025	0.99	25.195°	241.27°	0°	1386	4.777‰	0	16777 TU	36°	7221 km
20/Sep/2025	0.99	25.195°	217.16°	0°	1762	6.073‰	0	16483 TU	61°	7071 km
09/Nov/2025	0.99	25.195°	191.07°	0°	1493	5.145‰	0	15038 TU	87°	6721 km
29/Dec/2025	0.99	25.195°	162.66°	0°	1270	4.377‰	37	14200 TU	114°	6321 km
17/Feb/2026	0.99	25.195°	132.14°	0°	1033	3.560‰	16	14008 TU	142°	6096 km
08/Apr/2026	0.99	25.195°	100.51°	0°	665	2.292‰	10	11702 TU	236°	4096 km
28/May/2026	0.99	25.195°	69.30°	0°	849	2.926‰	179	10702 TU	255°	4146 km
17/Jul/2026	0.99	25.195°	39.82°	0°	814	2.805‰	143	10856 TU	276°	4346 km

- e_0, i_0, Ω_0, M_0: Initial eccentricity, inclination, longitude of the ascending node and mean anomaly.
- N_C: Total number of captures in the capture set.
- R_c: Capture ratio of the capture set.
- $N_{S_{th}}$: Number of captures coming from L_1 with stability index lower than threshold $S_{th} = 15000\,\mathrm{TU}$.
- S_{min}: Minimum stability index for captures coming from L_1.
- ω_0, r_{p_0}: Argument of periapsis and radius of periapsis of the capture with minimum stability index S_{min}.

Finally, Fig. 4.11 shows the evolution of a series of parameters describing the capture sets for the different epochs considered in the study of the problem. All parameters seem to follow a somewhat cyclical evolution, driven by the rotation of Mars around the Sun and the variation of its planetary true anomaly. In Fig. 2.3 it was shown how a true anomaly of around $f_0 = 45°$ and $f_0 = -135°$ are the most favorable for a minimum stability index and maximum number of captures, respectively [19]. The initial epoch, 08/May/2024, corresponds to a Mars perihelium, that is, $f_0 = 0°$. It can be seen how the minimum stability index is found soon after this initial epoch, confirming the results of the existing literature. The number of captures with stability index lower than the threshold is also maximum during these epochs, despite the total number of captures is minimum. The number of captures peaks however in late 2025, soon after Mars aphelion, also agreeing with the expected behavior.

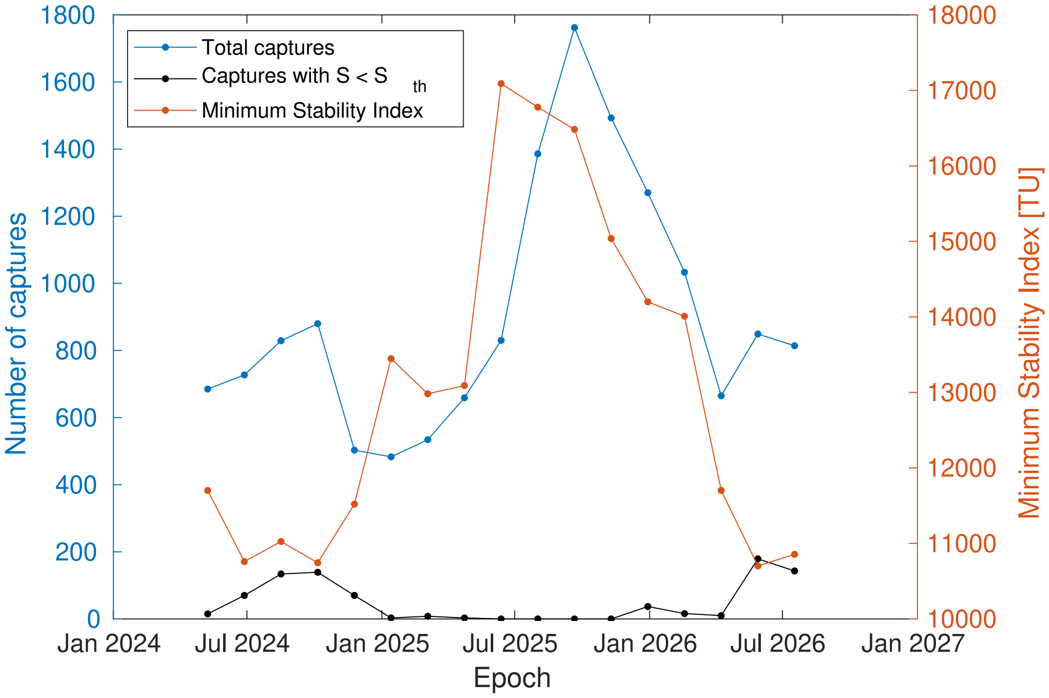

Figure 4.11: Evolution of the total number of captures, number of captures coming from L_1 with stability index lower than the threshold, and minimum stability index of the capture sets for all epochs considered.

For each epoch, a heliocentric transfer from Earth and a stabilization trajectory towards an areostationary orbit will be obtained. In the case of this work, one capture of each set will be selected based on the stabilization into an areostationary orbit. The transfer with lowest time of flight will be chosen as described in Part V. The heliocentric transfer will then be generated for that capture. However, it is first necessary to generate a spline of the ballistic trajectory towards Mars that can be targeted from Earth.

However, it has to be considered that only approximately half of the captures that belong to the set approach Mars from the L_1 Lagrange point, which is the one closer to Earth and the one that would be targeted in an actual mission design. For this reason, the captures will be classified depending on the Lagrange point gateway they use to approach the planet. Fig. 4.12 shows the capture set color-coded by the Lagrange point gateway used, along with a 1000-days backwards propagation that shows two clear manifold-like structures stemming out of the position of Mars. Fig. 4.13 shows the position for all captures at certain epochs when propagated backwards. The two different branches coming from both Lagrange points are clearly differentiated, particularly for long periods of integration. However, they both form somewhat regular structures and are reasonably close together, which is very positive for targeting the splines in the heliocentric phase. The results obtained in this phase for time of flight and propellant used should not vary much for the different orbits conforming a capture set. Besides, and even though it is outside the scope of this Thesis, once a solution for one capture is obtained, it could be used as an initial guess for neighboring ones, greatly alleviating the computational expenses of the heliocentric phase of the mission.

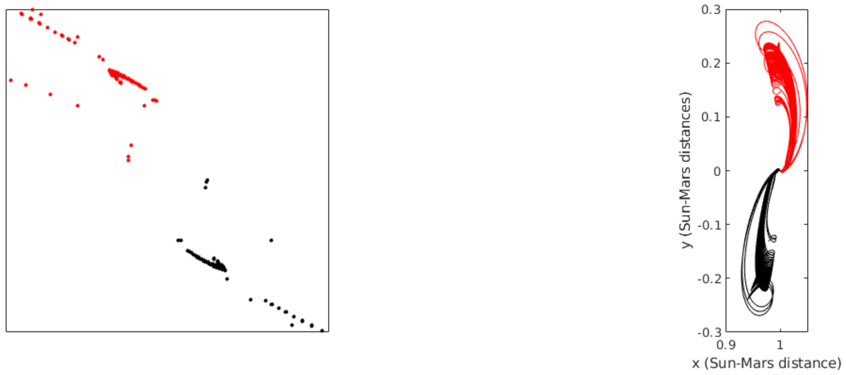

(a) (b)

Figure 4.12: a) Periapsis location of the capture set and b) backwards propagation of the captures for 1000 days in the Barycentric Pulsating Rotating Frame (BPR). Both refer to the capture set $\mathscr{C}^1_{-6}$ for t_0 and the black and red coloring represent captures approaching Mars from the L_1 and L_2 Lagrange points, respectively.

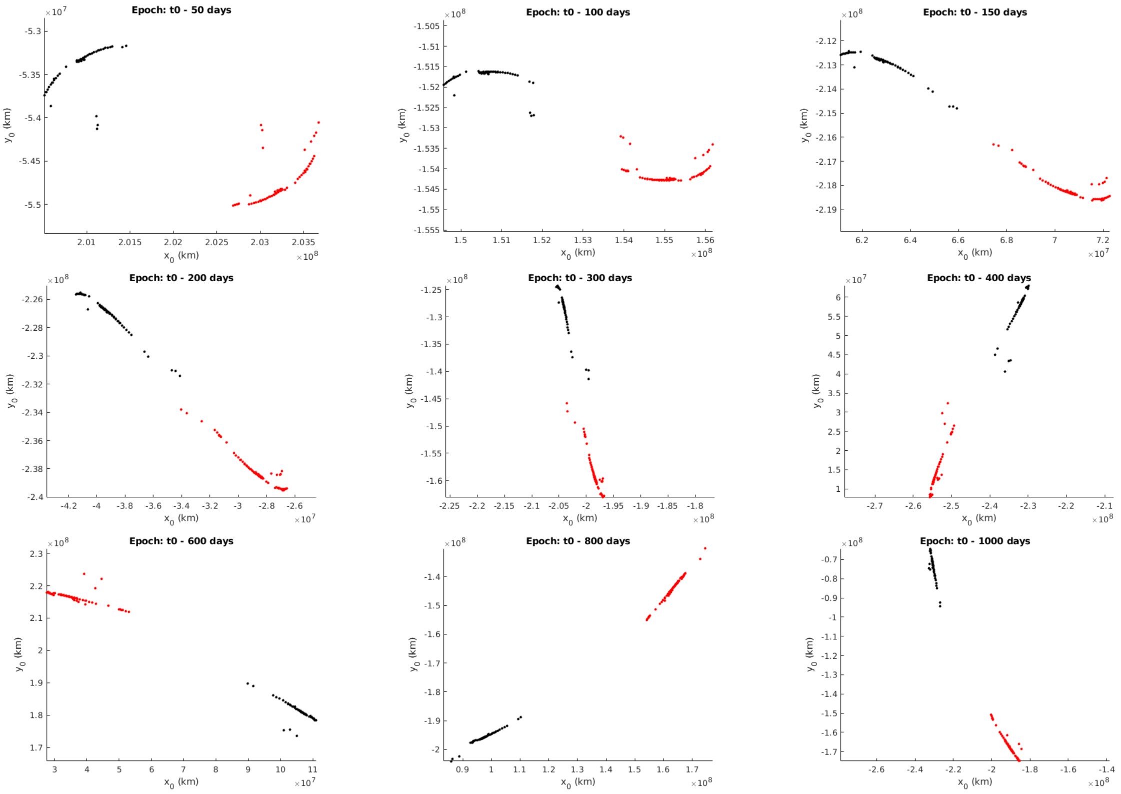

Figure 4.13: Position of the capture trajectories conforming the set $\mathscr{C}^1_{-6}$ at different epochs referred to the initial epoch t_0. All plots employ the Heliocentric Earth Orbital frame at Epoch (HEO@Epoch) which will be defined in Section 9. Black and red dots represent the captures approaching Mars from L_1 and L_2, respectively.

IV

ESCAPE FROM EARTH

5

METHODOLOGY

5.1. INTRODUCTION

This Chapter will introduce the methodology employed to generate the escape trajectory from the Earth-bound orbit the spacecraft is injected in to a hyperbolic escape state towards the interplanetary medium. Section 5.2 provides a description of the problem statement, particularly the characteristics of the chemical engine and the initial and final conditions of the transfer. Section 5.3 will introduce the reference frames employed, and Section 5.4 the equations of motion and dynamics model of the system. A description of the escape strategy employed will be given in Section 5.5. Finally, Section 5.6 will describe the computational implementation of this methodology.

5.2. PROBLEM STATEMENT

As introduced in Section 3.2, the estimated initial mass of the spacecraft when launched into orbit is 29.9 kg, including a 20% system margin [4].

Chemical propulsion will not be modeled as instantaneous burns but rather finite burns with a certain burn time. The specifications of the chemical propulsion system will depend on whether a mono-propellant or bi-propellant system is employed. The following values of the specific impulse and maximum thrust magnitude will be used in each case (retrieved from [32]):

- $T = 3.18$ N, $I_{sp} = 259.7$ s (mono-propellant thruster)
- $T = 2.91$ N, $I_{sp} = 303.15$ s (bi-propellant thruster)

The initial state of the spacecraft will be its injection orbit from the launcher, which for the reasons described in Section 1.2 will be a Geostationary Transfer Orbit (GTO). Geostationary orbits have a radius of 42,164 kilometers [33]. The apogee of the GTO will coincide with this altitude, and the perigee will be just a few hundred kilometers above the Earth's surface. Here, an altitude of 300 km, or a radius of 6671 km, will be assumed. Phasing will not be considered in this early stage of the mission design, and therefore the orientation of the orbit will not be considered important. In sum, the following orbital elements will define the initial state of the spacecraft:

$$[a, e, i, \Omega, \omega, M] = [24417\,\text{km}, 0.723, 0°, 0°, 0°, 0°]$$

The spacecraft will be assumed to escape the Earth once it reaches the Sphere of Influence (SOI), which has a radius of 924,660 kilometers when computed as in Eq. (3.12), with a certain excess velocity V_∞.

5.3. REFERENCE FRAMES

The integration of the escape trajectory will indeed be performed in an Earth-centered inertial reference frame, given the Earth is the main gravitational attraction (or only when studying the problem as a two-body problem) and therefore should be the center of integration. In particular, the Earth Mean Equator and Equinox of J2000 (EME2000) will be used. This reference frame was described in Section 3.3.

5.4. SPACECRAFT DYNAMICS AND EQUATIONS OF MOTION

The problem has been studied as a Two-Body Problem with the sole attraction of the Earth over the spacecraft. The equations of motion of this simple problem are as follow:

$$\ddot{\boldsymbol{r}} = -\frac{\mu_E}{r^3}\boldsymbol{r} + \boldsymbol{f_T} \tag{5.1}$$

where μ_E is the standard gravitational parameter of the Earth and $\boldsymbol{f_T}$ is the thrust force per unit mass. The thrust will always be assumed to be oriented in the direction of the spacecraft velocity, and in prograde motion, since that can be proven to be the most efficient way to accelerate the spacecraft and raise the apogee of its orbit.

The mass flow will be computed with the following expression:

$$\dot{m} = -\frac{T}{I_{sp}\, g_0} \tag{5.2}$$

5.5. ESCAPE STRATEGY

As stated before, burns will be modeled with a finite burn time instead of as instantaneous ΔV maneuvers. The burns will still take place around the perigee, but small gravity losses will occur due to the finite burn time. In order to avoid that these losses become very significant, a common strategy is to split the transfer into several apogee-raising maneuvers until the SOI is reached. The higher the number of maneuvers, the smaller the gravity losses will be, but the time of flight of the transfer will increase as well as the time spent in the Van Allen radiation belts which pose a threat to the spacecraft subsystems.

For each maneuver, the spacecraft state will be propagated from periapsis for a whole orbital period (computed by using the semi-major axis) minus half the burn time. Then the spacecraft will use its chemical propulsion for the specified burn time before starting another coasting period. This will be repeated until the last maneuver, where the spacecraft will stop using its thrust once the orbital energy allows for the spacecraft to reach the SOI with a certain hyperbolic excess velocity v_∞. Although this velocity could theoretically be zero (a parabolic escape), this leads to extremely long transfers where the spacecraft approaches the SOI asymptotically. Therefore, in the following Chapter an excess velocity of $v_\infty = 100$ m/s will be used. Once the spacecraft reaches the SOI the integration is terminated.

5.6. COMPUTATIONAL IMPLEMENTATION

Similar to *AREO*, which will be introduced and used in Part V, a new tool has been developed to implement the methodology described in this Section. This tool will be named *TERRA* and has also been coded using *MATLAB*. It is a very simple tool since it only implements two-body dynamics, and some simple event functions to determine when the spacecraft reaches a certain energy level or leaves the SOI. It is possible to use the tool to study one escape in particular or different types of grids.

6

RESULTS

6.1. INTRODUCTION

The results obtained for the study of the escape from Earth using the methodology described in the previous Chapter will be presented now. Section 6.2 will show the effect of the burn time on the escape trajectory and its performance. Section 6.3 will introduce a parametric study determining the effect of different parameters on this stage of the trajectory.

6.2. EFFECT OF THE BURN TIME

Both the mono-propellant and bi-propellant options described in Section 5.2 will be studied in this Section. First, and for reference, the ΔV necessary to reach the SOI of the Earth with the specified excess velocity $V_\infty = 100$ m/s is equal to $(\Delta V)_i = 740.52$ m/s. This value will be used to compute the gravity losses with equation (2.22).

A grid on both the burn time per orbit and thrust level will be considered. Thrust will be discretized from 2 to 3 N for the bi-propellant thruster and 2 to 3.2 N for the mono-propellant one. Meanwhile, burn times will be discretized from 300 to 1000 seconds per orbit.

Figs. 6.1 and 6.2 show the results obtained for the mono-propellant and bi-propellant engines, respectively. The fuel consumption is the main difference between both options, with the bi-propellant engine being considerably more efficient due to its higher specific impulse. This performance parameter increases for higher burn times, since these incur to gravity losses, but the effect is small. Fuel consumption is almost constant for different levels of the thrust.

Time of flight is as expected directly correlated with the number of burns (and therefore orbits) required to reach escape. Higher levels of thrust and longer burn times lead to much shorter transfers, with as little as 7 burns. The different specific impulse of the mono-propellant and bi-propellant engines does not seem to introduce much of a difference, although the slightly different maximum thrust could.

A very interesting parameter to analyze is the gravity losses in percentage points. For both engine options, they basically only depend on the burn time, ranging from around 0.3% for the minimum time burn considered to approximately 2.5% for the maximum. In any case, it can be seen how the gravity losses are very small when burning around periapsis for reasonable burn times, and the finite burns are similar in terms of performance with respect to impulsive maneuvers.

Finally, the orbits with minimum time of flight for both options are shown in Fig. 6.3. They are both almost identical from a trajectory point of view, with a difference of just four hours in total time of flight, but with the bi-propellant transfer requiring almost one kilogram less of fuel due to its higher specific impulse. The sequence of burns that progressively raise the apogee of the orbit can clearly be seen in the depiction of these orbits.

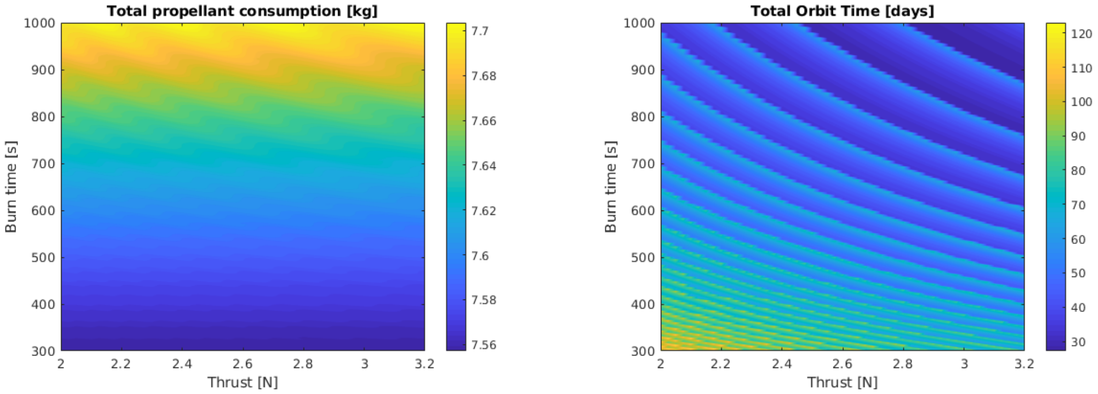

(a) Fuel consumption (b) Time of flight

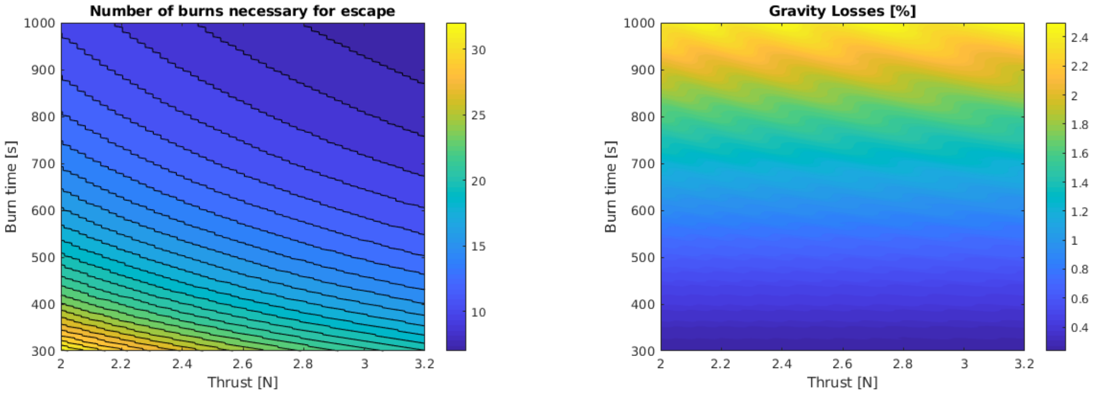

(c) Number of orbits (d) Gravity losses

Figure 6.1: Effect of the burn time t_b and thrust magnitude T on the fuel consumption, time of flight, gravity losses and number of burns necessary to reach escape, along with trajectory with the minimum TOF, for the engine with a mono-propellant thruster.

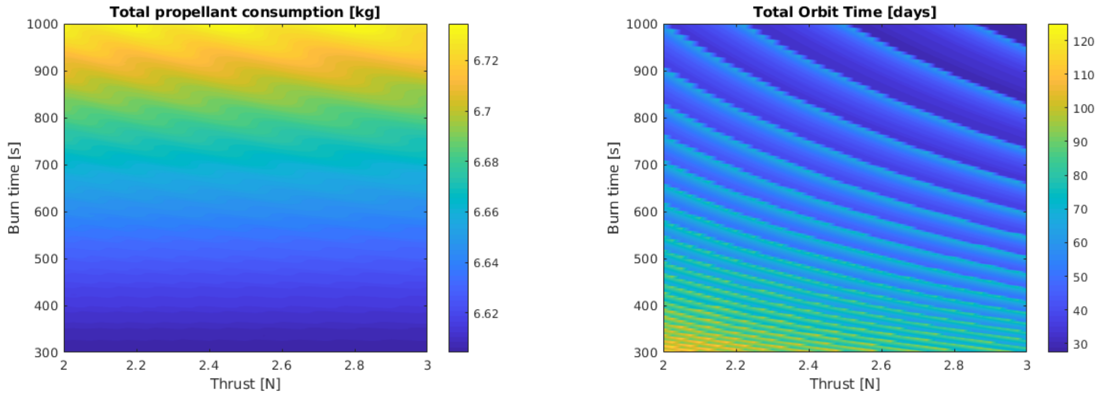

(a) Fuel consumption

(b) Time of flight

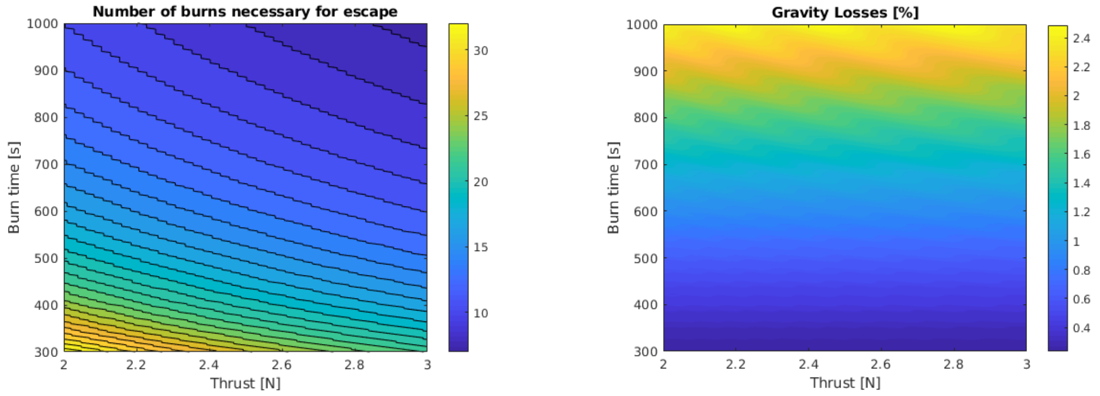

(c) Number of orbits

(d) Gravity losses

Figure 6.2: Effect of the burn time t_b and thrust magnitude T on the fuel consumption, time of flight, gravity losses and number of burns necessary to reach escape, for the engine with a bi-propellant thruster.

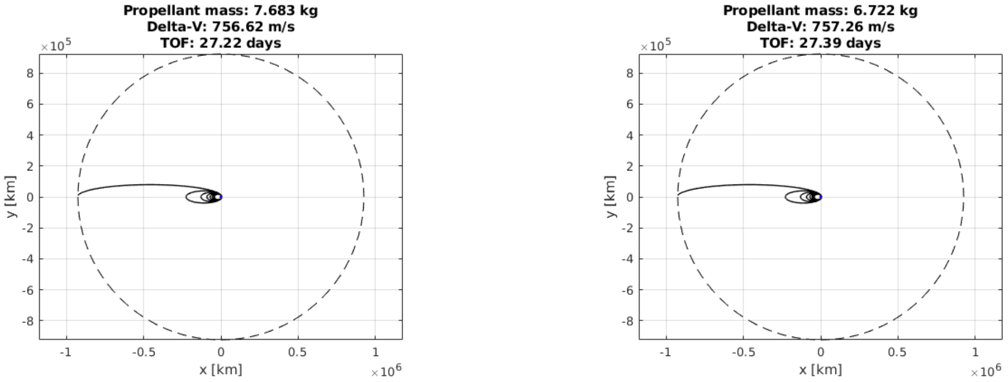

(a) Orbit with minimum TOF for the mono-propellant thruster ($t_b = 940$ s, $T = 2.975$ N)

(b) Orbit with minimum TOF for the bi-propellant thruster ($t_b = 960$ s, $T = 2.975$ N)

Figure 6.3: Trajectory of the escape from Earth with minimum time of flight for the engines with mono-propellant and bi-propellant thrusters.

Now, the thrust will be fixed to the maximum thrust magnitudes specified in Section 5.2 for each engine option. Figs. 6.4 and 6.5 show the effect of the burn time when fixing the thrust magnitude, this time with burn times considered up to 2000 seconds per orbit. The evolution of the time of flight and fuel consumption when increasing the burn time is interesting. The propellant consumption increases monotonically as expected, with longer burns leading to larger gravity losses since the spacecraft is thrusting farther from the perigee of the orbit. The gravity losses seem to grow more rapidly for longer burn times, and up to 500 grams of propellant could potentially be saved by using 300 seconds burns instead of 2000.

The time of flight on the other hand follows a slightly more complex dependence on the burn time employed. The time of flight is indeed lower for longer burn times, but it appears very important to employ a burn time that allows to reach the SOI in an efficient way, with a long last maneuver where the spacecraft reaches the energy necessary to escape. If the combination of maneuvers leads to a very small final burn, the final complete orbit of the spacecraft will have a very high apogee and a very long orbital period, causing the spikes in time of flight seen in Figs. 6.4 and 6.5. It can also be seen there how using 2000 seconds burns only four maneuvers are necessary to reach escape.

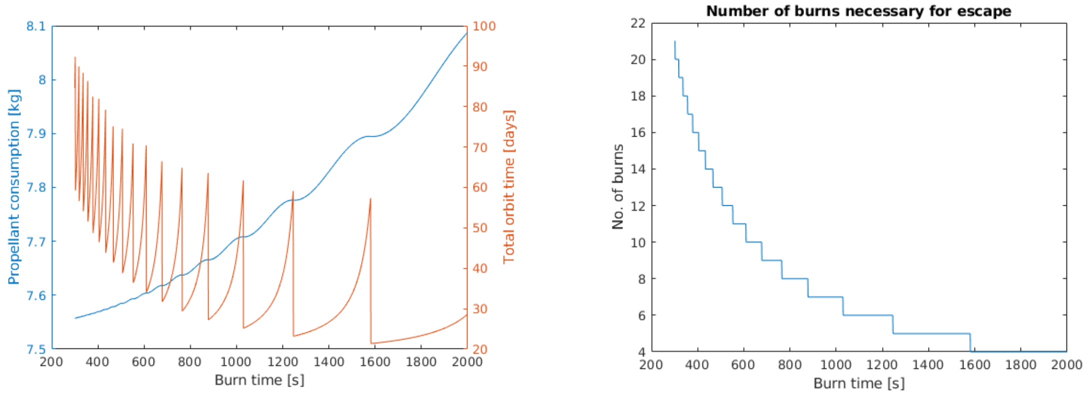

(a) Fuel consumption (left axis) and time of flight (right axis)

(b) Number of burns

Figure 6.4: Effect of the burn time t_b on the fuel consumption, time of flight and number of burns necessary to reach escape, for the engine with a mono-propellant thruster using its maximum thrust magnitude $T = 3.18$ N.

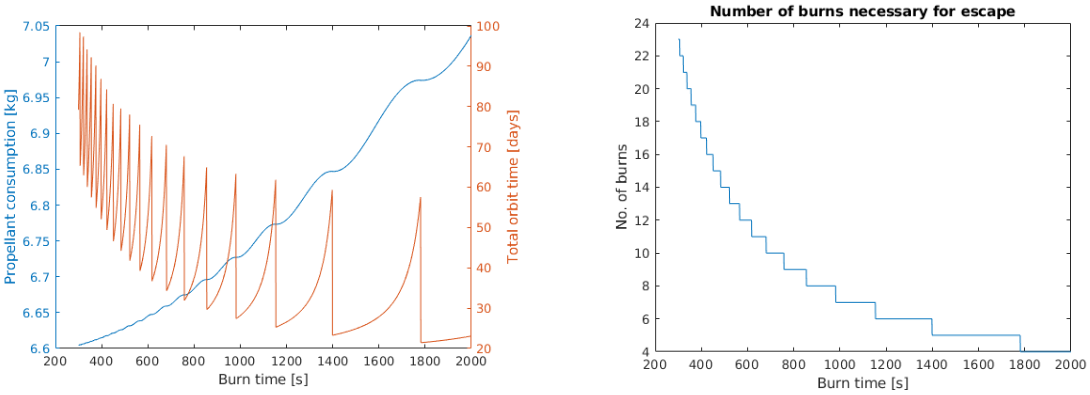

(a) Fuel consumption (left axis) and time of flight (right axis)

(b) Number of burns

Figure 6.5: Effect of the burn time t_b on the fuel consumption, time of flight and number of burns necessary to reach escape, for the engine with a bi-propellant thruster using its maximum thrust magnitude $T = 2.91$ N.

6.3. PARAMETRIC STUDY

The parametric study will try to determine the effect of several parameters defining the problem on the obtained trajectory. The parameters studied will be the characteristics of the initial injection orbit, in particular the radius of apogee and perigee, and the initial spacecraft mass. All simulations will employ the monopropellant engine introduced in Section 5.2 and a burn time of 1000 seconds.

Fig. 6.6 shows the effect of the altitude of perigee on the fuel consumption of the escape trajectory, ranging from 200 kilometers (considered a minimum feasible value due to Earth's atmosphere) to 1,000 kilometers. A higher perigee leads as expected to a larger propellant consumption, since the burns will take place at a higher altitude and therefore with a smaller spacecraft velocity, making less use of the Oberth effect. The difference can be of more than 200 grams for the range considered.

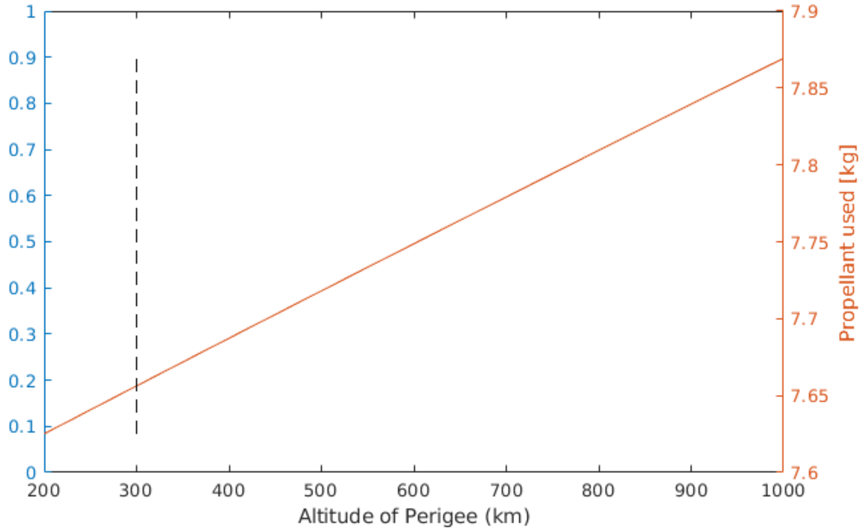

Figure 6.6: Effect of the initial altitude of perigee on the propellant consumption of the escape trajectory. The black dashed line represents the reference nominal value.

Fig. 6.7 shows the variation of the required number of burns and the fuel consumption with the initial radius of apogee of the orbit. The dashed black line represents the geostationary altitude. As could be expected, higher initial orbits lead to less required burns and a significantly smaller fuel consumption. Indeed, the launcher in turn needs to inject the spacecraft into a higher energy orbit. Super-synchronous GTO orbits are therefore a possible option to consider when looking for piggyback solutions for an actual mission.

Finally, Fig. 6.8 shows the effect of the initial spacecraft mass on the number of burns and the propellant consumption. A spacecraft that is 5 kilograms lighter at launch leads to one less revolution around the Earth and around 1.3 kilograms less of fuel spent.

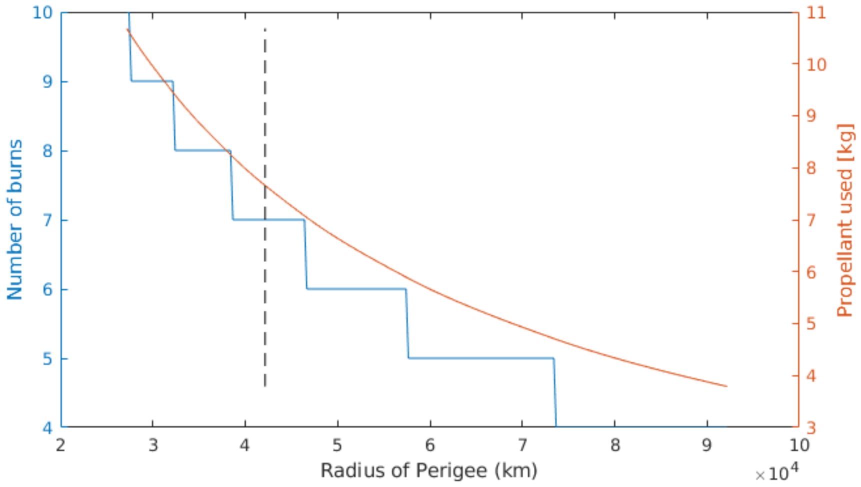

Figure 6.7: Effect of the initial radius of apogee on the propellant consumption and number of burns of the escape trajectory. The black dashed line represents the reference nominal value.

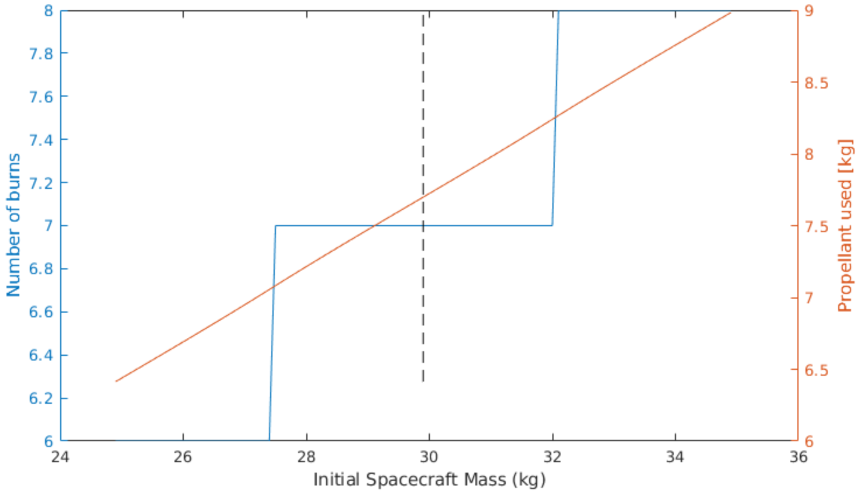

Figure 6.8: Effect of the initial spacecraft mass on the propellant consumption and number of burns of the escape trajectory. The black dashed line represents the reference nominal value.

V

STABILIZATION AROUND MARS

7

METHODOLOGY

7.1. INTRODUCTION

This Chapter will introduce the methodology employed to generate the stabilization trajectories of ballistic captures obtained in Part III into stable science orbits around Mars. Section 7.2 will describe the problem statement, particularly the initial and final states of the spacecraft and its characteristics. Like on the previous Chapter, Section 7.3 will introduce the reference frames used to study this part of the trajectory and Section 7.4 will explain the dynamics of the problem. The stabilization will be obtained with low-thrust propulsion that will employ control laws outlined in Section 7.5, or a combination of low-thrust and high-thrust. Finally, some aspects regarding the computational implementation of this methodology into a numerical tool will be described in Section 7.6

7.2. PROBLEM STATEMENT

Sections 3.2 already introduced some of the characteristics of the mission and the spacecraft design under study. The ballistic capture leg of the trajectory will not employ any fuel by definition, and therefore the same wet mass used at the beginning of the capture will be used again in this Chapter: 21 kg.

The spacecraft will start this stage of the trajectory at its first periapsis around Mars. After approaching the planet ballistically, its state at periapsis will be given by the osculating orbital parameters at t_0 forming the grid in Part III.

The target orbit on the other hand will be an areostationary orbit as stated before. However, and for operational reasons that will be described in the following Sections, the actual orbit that the algorithm will target will slightly deviate from a circular equatorial orbit.

Some other assumptions are now necessary for modeling this stage of the mission, in particular regarding the specifications of the low-thrust and high-thrust engines aboard the spacecraft. The high-thrust engine has already been described in Section 5.2.

A detailed analysis of options for low-thrust propulsion systems and electrical power systems is out of the scope of this Thesis, and therefore the following values will be used for the thrust and specific impulse profiles of the engine. These expressions are derived in [10] from the specifications suggested in [4].

$$T^* = 4.6264\left(\frac{r_{1AU}}{r}\right)^2 - 0.9833 \quad [\text{mN}] \qquad T_{max}(r) = \min(T^*, 1.24) \quad [\text{mN}] \tag{7.1}$$

$$I^*_{sp} = 9891.0\left(\frac{r_{1AU}}{r}\right)^2 - 2113.3 \quad [\text{s}] \qquad I_{sp_{max}}(r) = \min(I^*_{sp}, 2640) \quad [\text{s}] \tag{7.2}$$

7.3. REFERENCE FRAMES

As mentioned in the previous Section, the initial condition of the spacecraft after its ballistic trajectory is given by the osculating orbital elements at its first periapsis. These are expressed in the Radial-Tangential-Normal reference frame at Epoch (RTN@Epoch) described in Section 3.3. An important issue with this frame is that it refers to the Sun-Mars orbital plane instead of the planet's equatorial plane. It is thus hard to define a specific orbit around Mars such as an areostationary orbit. For this reason, a reference frame with a relation to the equatorial plane of Mars should be used. The IAU-Mars reference frame introduced in Section 3.3 is a rotating Mars-fixed frame. However, its orientation at epoch t_0 will be employed and hence it can be considered a non-rotating inertial frame. It will be referred to as IAU-Mars@Epoch. Finally, the Earth Mean Equator and Equinox of J2000 (EME2000) frame described in Section 3.3 is also used in this Chapter to retrieve planetary ephemeris from SPICE.

The position is then expressed in the IAU-Mars@Epoch frame using spherical coordinates (r, θ, ϕ). Velocity will be expressed in a spacecraft-centered frame, Spacecraft Range-Azimuth-Elevation (SRAE). The transformation matrix is matrix P defined as:

$$P \equiv \begin{bmatrix} \cos\phi\cos\theta & \cos\phi\sin\theta & \sin\phi \\ -\sin\theta & \cos\theta & 0 \\ -\sin\phi\cos\theta & -\sin\phi\sin\theta & \cos\phi \end{bmatrix} \tag{7.3}$$

7.4. SPACECRAFT DYNAMICS AND EQUATIONS OF MOTION

The dynamics and equations of motion do not vary much from the ones already described in Sections 3.4. The only important difference with respect to Equations (3.2) and (3.7) for the Three-Body and N-Body problems respectively, apart from the inclusion of thrust $\boldsymbol{f_T}$, is the different reference frame employed. Velocity is expressed in a spacecraft-centered rotating frame as described in the previous Section, what introduces an additional fictitious force:

$$\ddot{\boldsymbol{r}} = \boldsymbol{f_{2B}} + \boldsymbol{f_{TB}} + \boldsymbol{f_{SRP}} + \boldsymbol{f_{NSG}} + \boldsymbol{f_T} + S\begin{Bmatrix} v_r \\ v_\theta \\ v_\phi \end{Bmatrix} \tag{7.4}$$

where S is defined as:

$$S \equiv \begin{bmatrix} 0 & \dot\theta\cos\phi & \dot\phi \\ -\dot\theta\cos\phi & 0 & \dot\theta\sin\phi \\ -\dot\phi & -\dot\theta\sin\phi & 0 \end{bmatrix} \tag{7.5}$$

7.5. LOW-THRUST CONTROL LAWS

This Section will describe the control laws used to determine the low-thrust profile during the stabilization of the capture state. High-thrust may be used in the form of a short burn at the first periapsis, whose purpose is to quickly decrease the eccentricity of the capture trajectory and secure the orbit of the spacecraft around the planet. This burn will not have a magnitude larger than 50 meters per second, and Chapter 6 has already shown that finite burn maneuvers of this magnitude with the engine considered take place in only a few minutes around periapsis and with very small gravity losses, of only around 1%. For that reason, and without an important loss of significance, this initial maneuver at periapsis will be modeled as an instantaneous ΔV. Low-thrust propulsion will in any case be the responsible of reaching a stable science orbit around Mars.

Four different laws will be studied in increasing level of complexity. The first three are inspired by the work of Soler Lanagrán [34]. The first one is a very simple bang-bang control, that implements a prograde thrust when the current radius of the spacecraft is larger than its osculating semi-major axis, and a retrograde thrust when it is lower:

$$\boldsymbol{f_T} = \begin{cases} \frac{T}{m}\boldsymbol{u_t} & \text{if } r > a \\ -\frac{T}{m}\boldsymbol{u_t} & \text{if } r \leq a \end{cases} \tag{7.6}$$

where T is the available thrust, m is the current mass of the spacecraft and u_t is a unit vector tangential to the spacecraft trajectory.

Indeed, the only effect of this control will be to circularize the orbit, the eccentricity will decrease continuously but no specific value for the semi-major axis will be obtained.

The second control law is an extension of the previous thrust logic that enforces a zero thrust when the current radius of the spacecraft is larger than the osculating semi-major axis but the osculating radius of perigee is also larger than the radius of the target orbit r_t:

$$\boldsymbol{f_T} = \begin{cases} \frac{T}{m}\boldsymbol{u_t} & \text{if } r > a \text{ and } r_p < r_t \\ \boldsymbol{0} & \text{if } r > a \text{ and } r_p \geq r_t \\ -\frac{T}{m}\boldsymbol{u_t} & \text{if } r \leq a \end{cases} \tag{7.7}$$

In this case, the trajectory will converge towards the target radius of perigee and eccentricity. However, as will be shown later, the process will be slower due to the spacecraft not using any propulsion for a significant part of the orbit.

The third control law can be thought of as a combination of the previous two, and will be divided into three different stages. First, control law 1 (Equation (7.6)) is used to decrease the eccentricity until the target eccentricity is reached. Then, a constant retrograde acceleration is applied in order to decrease the semi-major axis as fast as possible. This however will increase the eccentricity of the orbit again, so a brief third stage uses control law 2 (Equation (7.7)) to finally reach the target semi-major axis and eccentricity, a priori much faster than when using control law 2 during the whole process.

It should be noted that the three control laws explored so far only accommodate the semi-major axis (control laws 2 and 3) and eccentricity (control laws 1, 2 and 3) of the orbit. The longitude of the ascending node and argument of periapsis are not really defined in an areostationary orbit in the reference frame employed and targeting a specific orientation of the orbit is out of the scope of this preliminary mission design. The inclination is however important. The captures generated in Section 4.4 already have zero inclination in order to make the stabilization into an areostationary orbit easier. However, a control law that also targets the inclination apart from the semi-major axis and eccentricity seems necessary. Instead of extending the definition of the previous control laws to target a specific inclination, a Q-law is implemented like the one described in the work of Petropoulos [35].

Q-Law

This law uses a so-called proximity quotient Q, which measures the similarity of the current osculating orbit and the target orbit:

$$Q = (1 + W_P P) \sum_{oe} W_{oe} S_{oe} \left[\frac{d(oe, oe_T)}{\tilde{\dot{oe}}_{xx}} \right]^2 \qquad \text{for } oe = a, e, i \tag{7.8}$$

where the only three orbital elements oe of interest will be the semi-major axis a, inclination i and eccentricity e. The equation above could indeed be extended to include the longitude of the ascending node and argument of periapsis. W_P and W_{oe} are scalar weights greater than zero, whose value will be discussed in Chapter 8. The remaining terms are functions that will now be discussed.

P is a penalty function that prevents the spacecraft from reaching values of the radius of periapsis that are not feasible (e.g. the spacecraft entering the Martian atmosphere):

$$P = \exp\left[k \left(1 - \frac{r_p}{r_{p_{min}}} \right) \right] \tag{7.9}$$

where k is a scalar and $r_{p_{min}}$ is the minimum value for the radius of periapsis.

S_{oe} is a scaling function to prevent discrepancies between the weight of the different orbital elements. Despite distances are normalized (see Section 7.6), the scaling function will make sure the semi-major axis has comparable values to the rest of orbital elements:

$$S_{oe} = \begin{cases} \left[1 + \left(\frac{a - a_T}{m a_T} \right)^n \right]^{\frac{1}{r}} & \text{for } oe = a \\ 1 & \text{for } oe = e, i \end{cases} \tag{7.10}$$

where $m = 3$, $n = 4$ and $r = 2$.

The distance function $d(oe, oe_T)$ will be defined as

$$d(oe, oe_T) = oe - oe_T \qquad \text{for } oe = a, e, i \tag{7.11}$$

Finally, $\tilde{\dot{oe}}_{xx}$ measures the maximum rate of change of the orbital element oe over thrust direction and true anomaly:

$$\tilde{\dot{oe}}_{xx} = \max_{\alpha, \beta, \theta} (\dot{oe}) \qquad \text{for } oe = a, e, i \tag{7.12}$$

where θ is the true anomaly and α and β define the direction of the thrust as follows:

$$\begin{aligned} f_r &= f\cos\beta\sin\alpha \\ f_\theta &= f\cos\beta\cos\alpha \\ f_h &= f\sin\alpha \end{aligned} \tag{7.13}$$

with f the magnitude of the thrust.

The expressions for $\tilde{\dot{oe}}_{xx}$ can be derived from the Gauss's form of the variational equations of motion of the spacecraft. The final expressions for the three orbital parameters under study are as follow [35]:

$$\dot{a}_{xx} = 2f\sqrt{\frac{a^3(1+e)}{\mu(1-e)}} \tag{7.14}$$

$$\dot{e}_{xx} = \frac{2pf}{h} \tag{7.15}$$

$$\dot{i}_{xx} = \frac{pf}{h(\sqrt{1-e^2\sin^2\omega}-e|\cos\omega|)} \tag{7.16}$$

where μ is the standard gravitational parameter of Mars, p is the semilatus rectum and h is the specific angular momentum of the spacecraft.

The way that Q has been constructed, it will take positive values always except at the target orbit where it will be zero, and it is a measure of how long the current thrust profile will take to reach that target orbit. For this reason, an optimal thrust profile will be the one that minimizes Q at each step. The time rate of change of Q is

$$\frac{\mathrm{d}Q}{\mathrm{d}t} = \sum_{oe}\frac{\partial Q}{\partial oe}\dot{oe} \tag{7.17}$$

The variation of the orbital elements with time is given by the Gauss's form of the orbital equations mentioned before:

$$\frac{\mathrm{d}a}{\mathrm{d}t} = \frac{2a^2}{h}\left(e\sin\theta f_r + \frac{p}{r}f_\theta\right) \tag{7.18}$$

$$\frac{\mathrm{d}e}{\mathrm{d}t} = \frac{1}{h}\{p\sin\theta f_r + [(p+r)\cos\theta + re]f_\theta\} \tag{7.19}$$

$$\frac{\mathrm{d}i}{\mathrm{d}t} = \frac{r\cos(\theta+\omega)}{h}f_h \tag{7.20}$$

Once all elements have been defined it is possible to obtain at each step the thrust angles α and β that minimize the rate of change in Equation (7.17). A minimization problem needs to be solved at every integration step, hence it is important to alleviate the computational expenses of computing these thrust angles. For this reason, an analytical expression of the derivative of Q is obtained as a function of both thrust angles and the current orbital elements, using *MATLAB*'s Symbolic Toolbox.

Once the thrust angles are obtained, the thrust force per unit mass is readily available by using Equation (7.13).

7.6. COMPUTATIONAL IMPLEMENTATION

Unlike GRATIS, used in Part III, and DIREct collocation Tool for Trajectory Optimization (DIRETTO), used in Part VI, no tool was already developed that implemented the methodology outlined in this Section. For this reason, a new tool named *AREO* after its main original purpose (studying the stabilization of ballistic captures at Mars), has been coded in *MATLAB*.

The tool also uses SPICE as well as some of the general structure of GRATIS, given that both tools use the same initial conditions and integrate a somewhat similar problem. Again, Mars is employed as the Center of Integration (COI), and the RnBP equations of motion are written in the form of Eq. (3.17) to avoid any loss of significance. The numerical integrator will again be *MATLAB*'s built-in *ode113*. A simple initialization function allows the user to select the dynamics employed, the control law and the type of engine. It is possible to stabilize one single capture, a complete grid or a capture set generated by GRATIS. In the case of integrating a grid, parallelization can be used to speed up the computation of the different initial conditions, which are independent from each other.

When the Q-law described in Section 7.5 is used, a minimization problem needs to be solved at each iteration. As stated before, an expression of Q as a function of the thrust angles and the state of the spacecraft was obtained analytically using *MATLAB*'s Symbolic Toolbox, avoiding the computation of numerical differences for each function evaluation. The minimization problem is solved using *MATLAB*'s *fminsearch*, which uses a Nelder-Mead simplex direct search method to find the minimum of unconstrained multi-variable functions. A description of the method, which does not use numerical or analytical gradients, can be found in [36].

8

VERIFICATION AND RESULTS

8.1. INTRODUCTION

This Chapter will first present a verification of the methodology above and the *AREO* tool in Section 8.2. Section 8.3 will show the stabilization of a specific capture using the different control laws outlined in the previous Chapter. The effect of the different spacecraft dynamics that can be employed will also be explored in Section 8.4. Section 8.5 will present a parametric study of several variables affecting the trajectory stabilization problem. Finally, the results of the stabilization of the capture sets generated in Chapter 4 will be shown in Section 8.6.

8.2. VERIFICATION

Since the integration is performed in a different reference frame as the one used in Part III, a verification of the propagation of the orbit in the IAU-Mars@Epoch and Spacecraft Range-Azimuth-Elevation (SRAE) frames will be made. The same initial conditions in the RTN@Epoch frame will be propagated using GRATIS and *AREO*. The results should be very similar, with an expected small numerical error due to the several frame transformations involved and the computation of the fictitious forces described in Section 7.4.

A capture trajectory with the initial conditions outlined in Table 8.1 is integrated for one year with both tools. In both cases, an ephemeris model is employed that includes the gravitational perturbation of the Sun and all planetary bodies in the Solar System, as well as SRP and NSG up to degree and order 5.

The difference between the results obtained with GRATIS and *AREO* is shown in Fig. 8.1. The error is in the order of a few kilometers, which will be considered acceptable for the purpose of this preliminary mission design.

8.3. CONTROL LAWS

This Section will explore the stabilization of one capture trajectory using all control laws described in Section 7.5, with the purpose of showing how they affect the trajectory of the spacecraft. The initial conditions of the

Table 8.1: Initial conditions used for the verification of the propagation of the spacecraft orbit with the *AREO* tool.

Orbital parameter	**Value**
Eccentricity	$e_0 = 0.98$
Longitude of the ascending node	$\Omega_0 = 0°$
Inclination	$i_0 = 22.5°$
Argument of periapsis	$\omega_0 = 326°$
Radius of periapsis	$r_{p_0} = 4346$ km
Mean anomaly	$M_0 = 0°$
Initial epoch	$t_0 = 08/\text{May}/2024$ 12:36:08.640 UTC

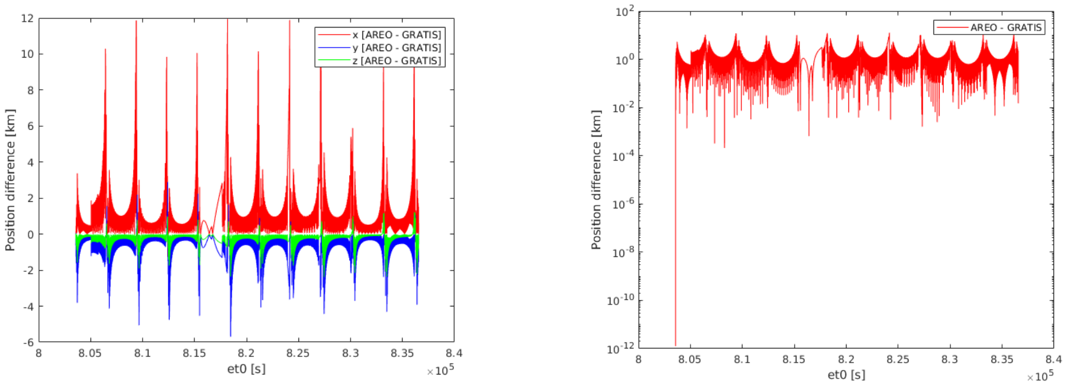

(a) Position error per component (absolute scale).

(b) Norm of the position error (logarithmic scale).

Figure 8.1: Difference between the position of the spacecraft in its capture trajectory when propagated using GRATIS and *AREO*. The initial conditions of the capture are introduced in Table 8.1.

capture will be those used in the previous Section, outlined in Table 8.1. All simulations will use a dynamical model with gravitational perturbations of all planetary systems in the Solar System and the Sun, SRP and Mars' NSG up to order and degree 5. They all use the low-thrust engine specifications outlined in Chapter 10.

Fig. 8.2 shows the propagation for 1,000 days of the capture with the initial conditions introduced in Table 8.1. It can be seen how the spacecraft remains bounded around Mars during the whole integration period but following a very eccentric non-Keplerian trajectory.

As described in Section 7.5, the first control law considered a constant bang-bang thrust profile that aims to reach a very small value of the osculating eccentricity, here set to be $e_t = 0.05$. Fig. 8.3 shows the resulting trajectory when implementing this control. The spacecraft reaches a 0.05 eccentricity after approximately 116 days and 130 grams of propellant used, taking approximately three revolutions around Mars. However, the semi-major axis of the resulting circular orbit is very large, approximately 8 times larger than an areostationary orbit. Hence, this very simple control law does indeed not reach the desired target orbit but serves as a first cornerstone when studying the stabilization of the capture. It should be noted how as expected the spacecraft applies a prograde thrust (in red) when close to its apoapsis in order to raise the periapsis, and a retrograde thrust (in blue) when close to its periapsis in order to lower the apoapsis.

Fig. 8.4 shows the trajectory obtained when applying the second control law. This is basically a further iteration of the first control law that now implements a reduction of the semi-major axis. By not thrusting when the radius of perigee is at its desired value (that of an areostationary orbit, 20,428 kilometers), both the target

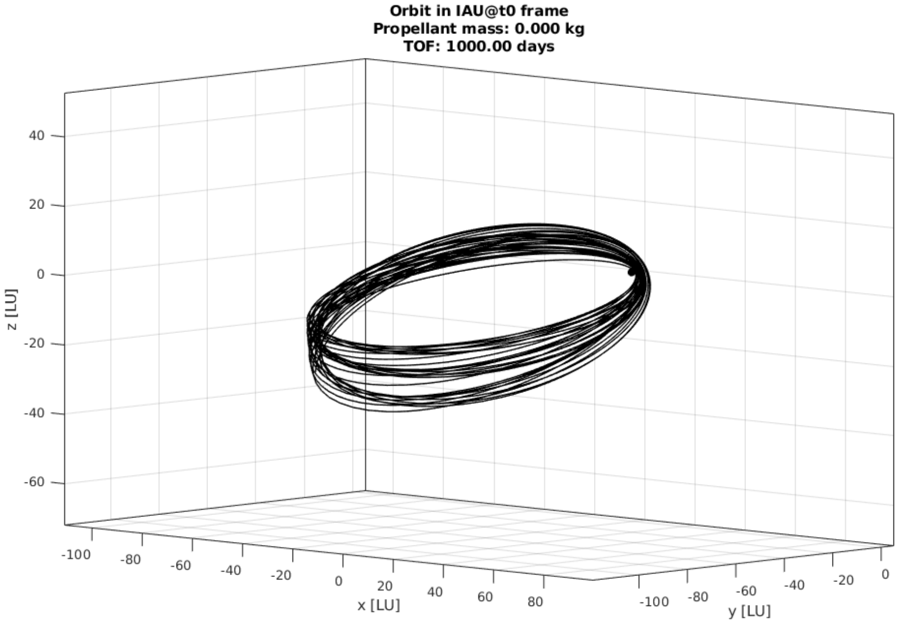

Figure 8.2: Trajectory in the IAU-Mars@Epoch reference frame of the capture that will be used to study the stabilization using different control laws.

eccentricity and semi-major axis will be reached. This indeed leads to a much longer time of flight (670 days) and larger fuel consumption (324 grams), and a very large number of revolutions around the planet. A very significant part of the trajectory is spent with the spacecraft not thrusting at all, which will prove efficient from a fuel consumption point of view but will lead to very long transfer times.

For this reason, Fig. 8.5 implements a more direct approach to reach the target semi-major axis and eccentricity. This control law will be split into three different stages as stated in Section 7.5. First, the same thrust logic and trajectory as the one used in control law 1 is employed. However, once the target eccentricity is reached, the spacecraft spirals down with constant retrograde thrust until the target semi-major axis. This leads to a small raise in eccentricity, which is corrected in a final third stage following the thrust logic implemented in control law 2. This process can be clearly seen in Fig. 8.5b), where the dashed red lines represent the different stages of the stabilization. This strategy leads to a higher fuel consumption (414 grams) than control law 2, but a much shorter time of flight (372.5 days).

Finally, control law 4 is the already described Q-law. This is the only thrust logic that targets a certain inclination (in this case 0°) apart from semi-major axis and eccentricity. The Q-law will employ the following values for the parameters described in Section 7.5:

- Penalty function scalar $k = 1$
- Minimum radius of periapsis $r_{p_{min}} = 1.01$ LU
- Penalty function weight $W_P = 1$
- Semi-major axis weight $W_a = 10$
- Eccentricity weight $W_e = 3$
- Inclination weight $W_i = 1$

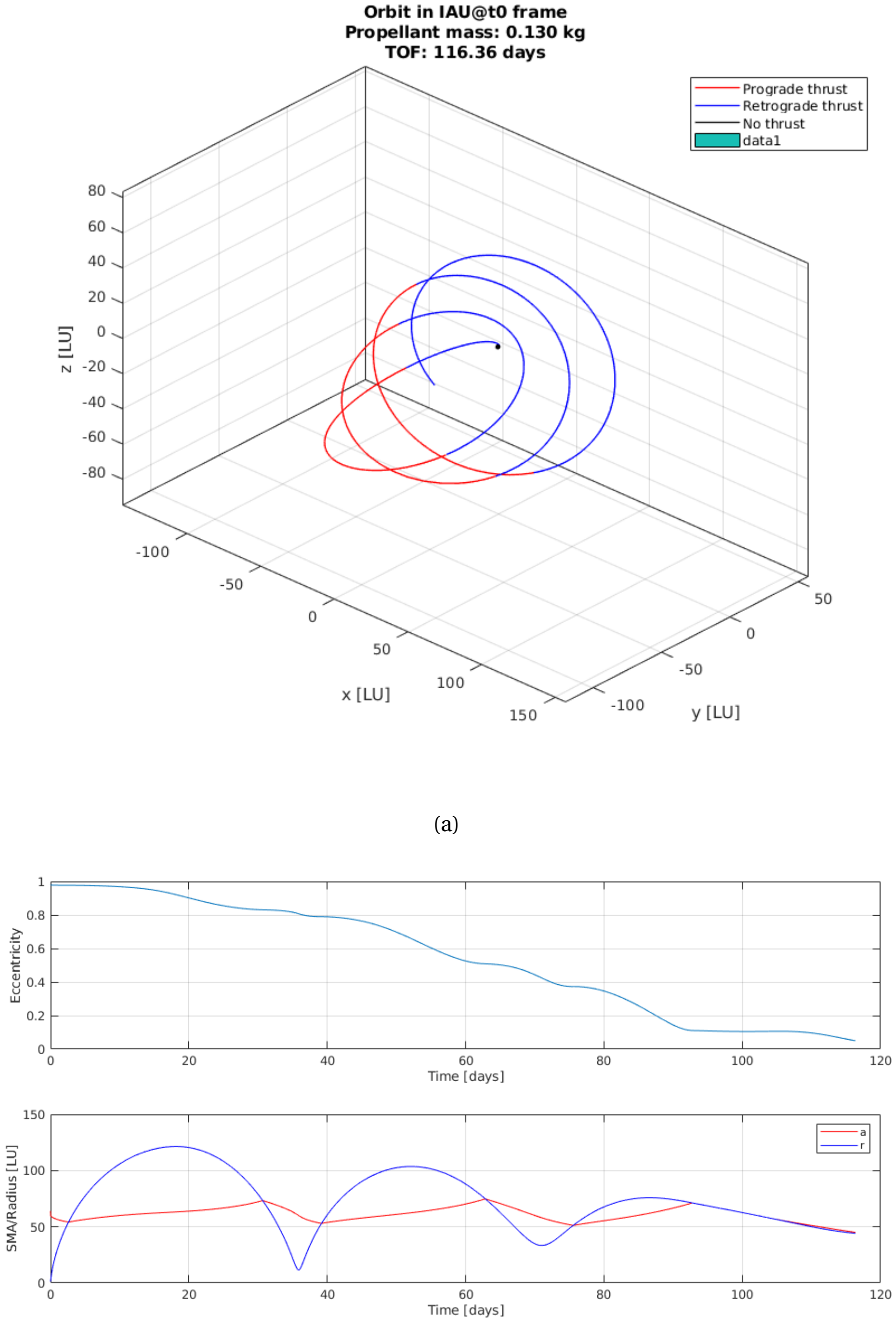

(a)

(b)

Figure 8.3: a) Orbit and b) evolution of the eccentricity and semi-major axis of the stabilized trajectory using control law 1.

These values will be used for all transfers implementing the Q-law studied in this Chapter.

Fig. 8.6 shows the resulting orbit when using the Q-law to stabilize the capture, along with the evolution of the orbital elements. It is clearly seen how the inclination is quickly corrected while the spacecraft is still far away from Mars, and a continuous spiral down towards the areostationary orbit lowers the values of both the eccentricity and semi-major axis simultaneously. The Q-law uses only slightly more fuel (474 grams) and time of flight (425 days) than control law 3, which is remarkable considering an important orbital plane change is required to correct the inclination.

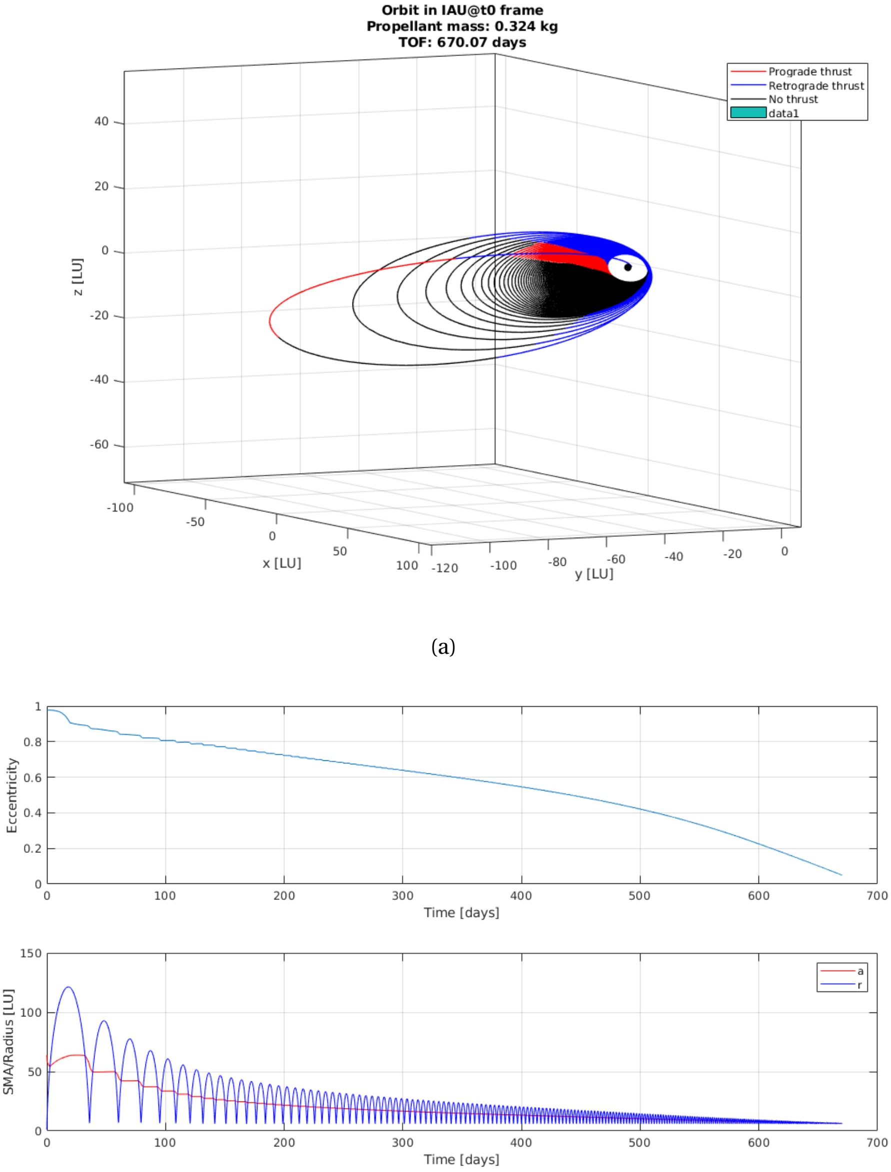

(a)

(b)

Figure 8.4: a) Orbit and b) evolution of the eccentricity and semi-major axis of the stabilized trajectory using control law 2.

8.4. EFFECT OF THE DYNAMICS

The effect of the dynamics model employed in the stage of the mission will be studied by simulating the stabilization of the capture used in the previous two Sections (see Table 8.1) with several different models. In particular, the four models (CRTBP, ERTBP and two ephemeris models with and without SRP and NSG) described in Section 4.3, and a simple Two-Body Problem simulating just the spacecraft and Mars. The Q-law will be used as the control law for all simulations in this Section.

Fig. 8.7 shows a comparison of each alternative model with the one used in the previous Section, i.e. an ephemeris model including all planetary bodies and SRP and NSG. On the other hand, Table 8.2 shows parameters describing the resulting stabilized trajectories. Some conclusions can be drown from these results.

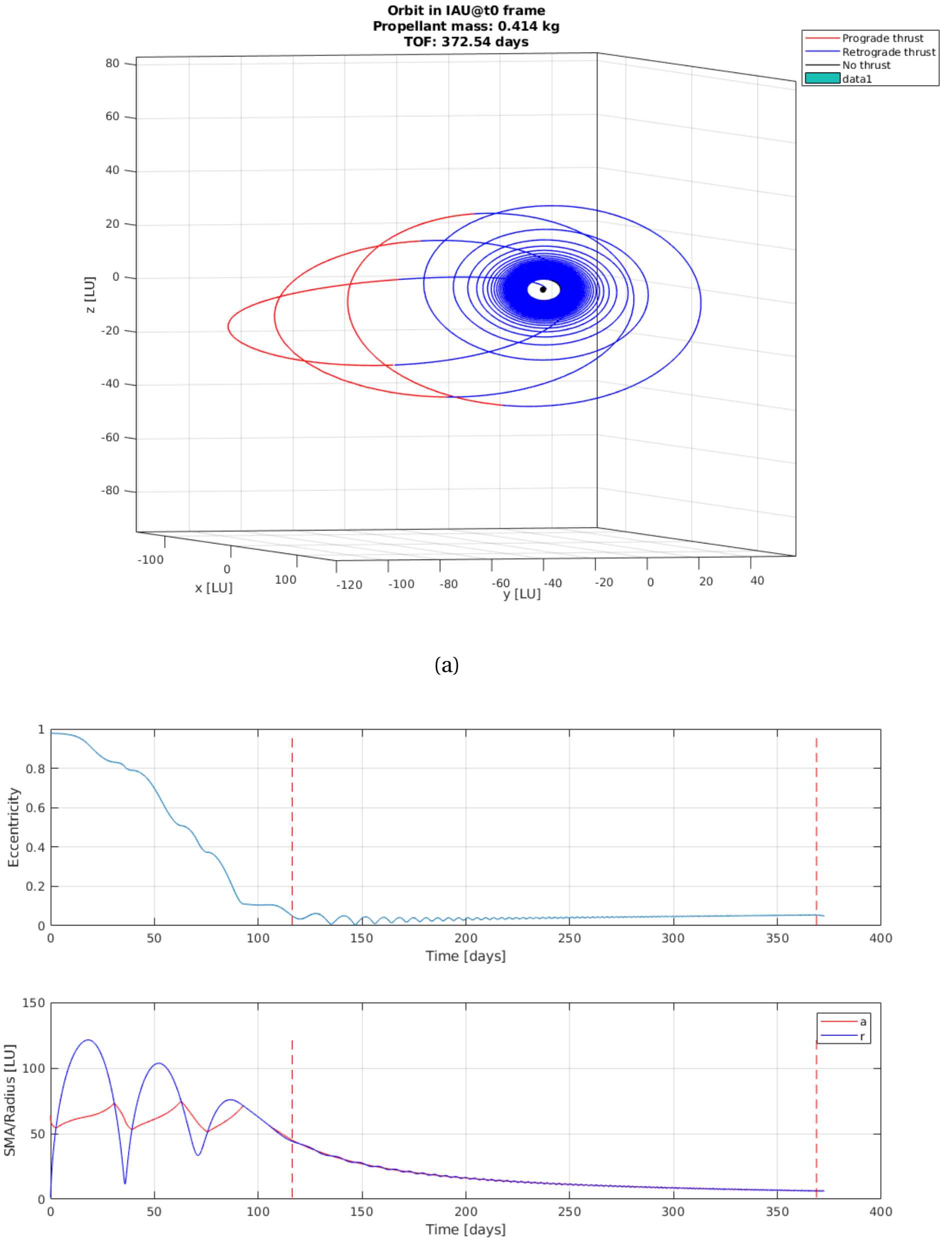

(a)

(b)

Figure 8.5: a) Orbit and b) evolution of the eccentricity and semi-major axis of the stabilized trajectory using control law 3.

First, the changes are not very large, at least when compared with those that existed in Chapter 4 for instance. In fact, the differences are almost negligible except for the most complex ephemeris model. This can be explained because the spacecraft spends a very significant part of the stabilization trajectory at a small distance from Mars, where the NSG of the planet becomes a very important perturbation. At least for this specific capture, it seems that it is also a perturbation that favors the stabilization making it faster. Taking into account that even the two-body model is very similar, one could argue that the presence of other gravitational bodies including the Sun represents a considerably smaller perturbation. However, the computational time is almost independent of the model used, suggesting that the integration of the dynamics represents a small part of the computational expenses, which are most likely driven by the optimization performed at every step

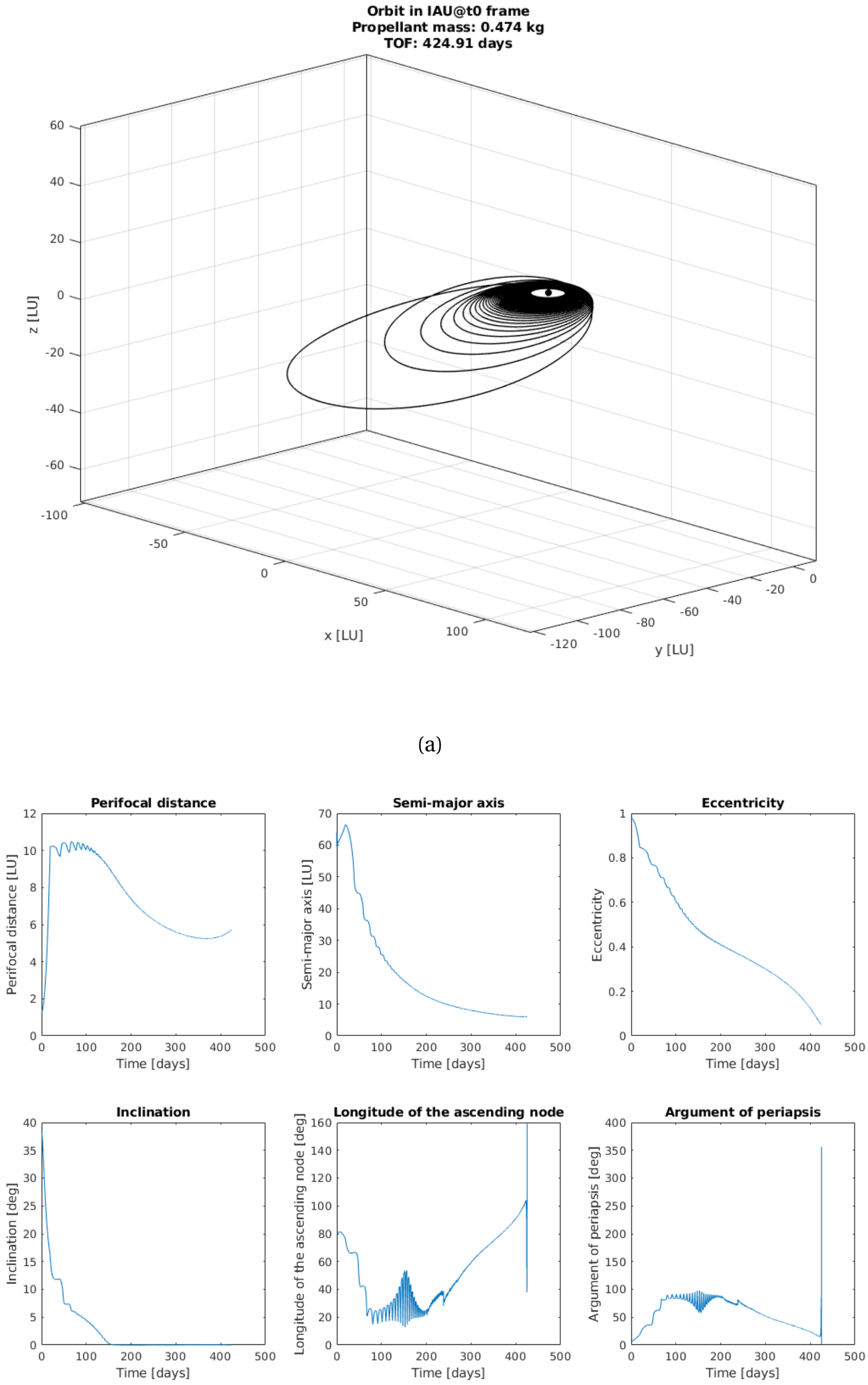

(a)

(b)

Figure 8.6: a) Orbit and b) evolution of the orbital elements of the stabilized trajectory using control law 4.

of the Q-law control algorithm. For this reason, and in order to be consistent with the ballistic stage of the mission studied in Part III and make use of the NSG of Mars, the most complex ephemeris model will be used for the stabilization of the captures in the following Sections.

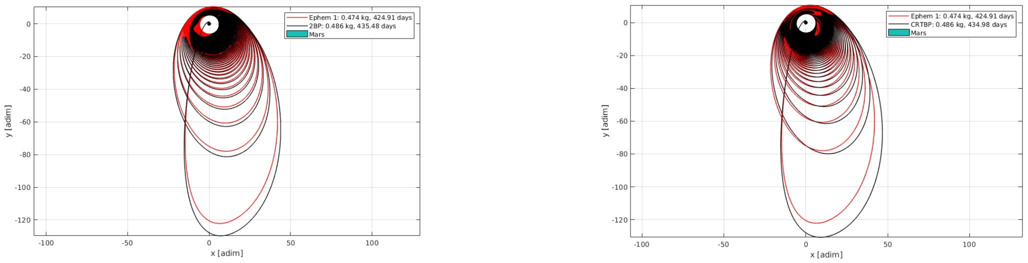

(a) Two-Body Problem (b) CRTBP

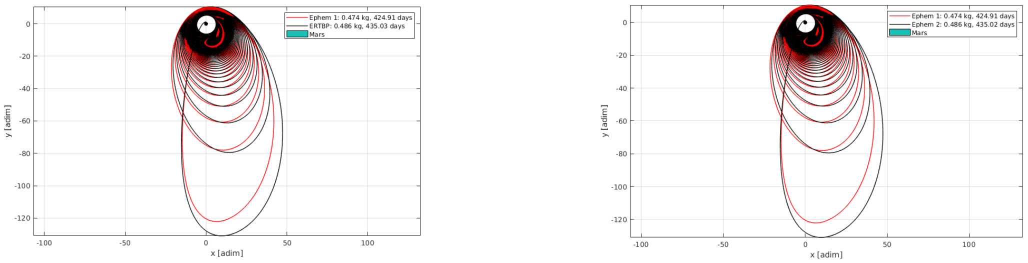

(c) ERTBP (d) Ephemeris Model 1

Figure 8.7: Trajectory of the stabilized capture using the Q-law and different dynamical models, compared with the complete ephemeris model (in red).

Table 8.2: Characteristics of the stabilized trajectory obtained with the five different dynamical models employed.

Model	**TOF [days]**	**Fuel mass [g]**	**Comp. Time [s]**
Two-Body	435.48 days	486 g	106.11 s
CRTBP	434.98 days	486 g	108.17 s
ERTBP	435.02 days	486 g	103.48 s
Ephem. 1	435.02 days	486 g	100.1 s
Ephem. 2	424.91 days	474 g	94.6 s

8.5. PARAMETRIC STUDY

In this Section a parametric study will be conducted to determine the influence of certain parameters in the resulting stabilized trajectories. Again, the Q-law will be employed with a complete ephemeris model including SRP and NSG. For each parameter studied, the variation of the time of flight of the transfer will be studied with respect to the reference value used in the previous Sections. Although the reference values will not be changed for generating the stabilization study of the capture sets in Section 8.6, it is interesting to know the effect that varying these parameters would have on the problem.

Fig. 8.8 shows the effect of the initial spacecraft mass on the time of flight. As could be expected, a lower spacecraft mass leads to much faster transfers, and vice versa. The effect is very important, with around 25 days saved for every kilogram that is taken off the spacecraft. This gives an idea of the importance of the mass budget in a spacecraft, particularly in a small satellite like a CubeSat.

The specifications of the spacecraft low-thrust engine are also a determining factor in the characteristics of the transfer. The effect of the specific impulse and thrust magnitude is studied on both the time of flight and fuel consumption and shown in Figs. 8.9 and 8.10. A larger thrust leads indeed to a much faster transfer, with two to three months saved for a 20% larger thrust, as well as slightly less fuel consumption. The specific

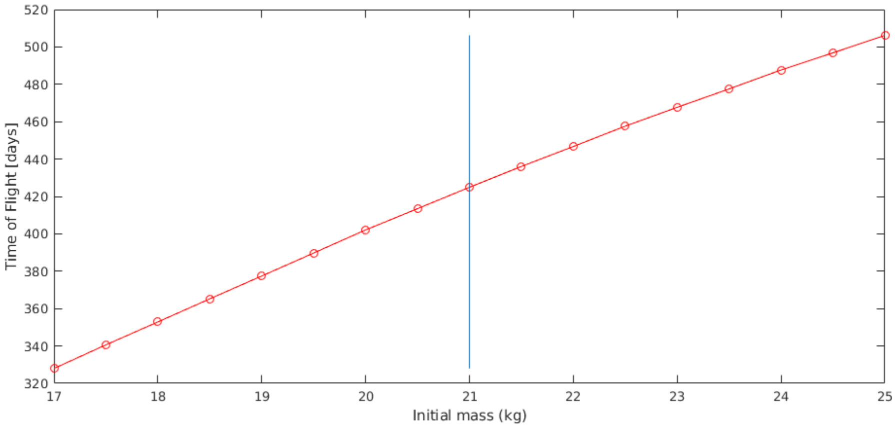

Figure 8.8: Variation of the time of flight of the capture for different values of the initial spacecraft mass. The reference value is shown with a blue line.

impulse has a very small effect on the time of flight, but can lead to great savings in terms of propellant use.

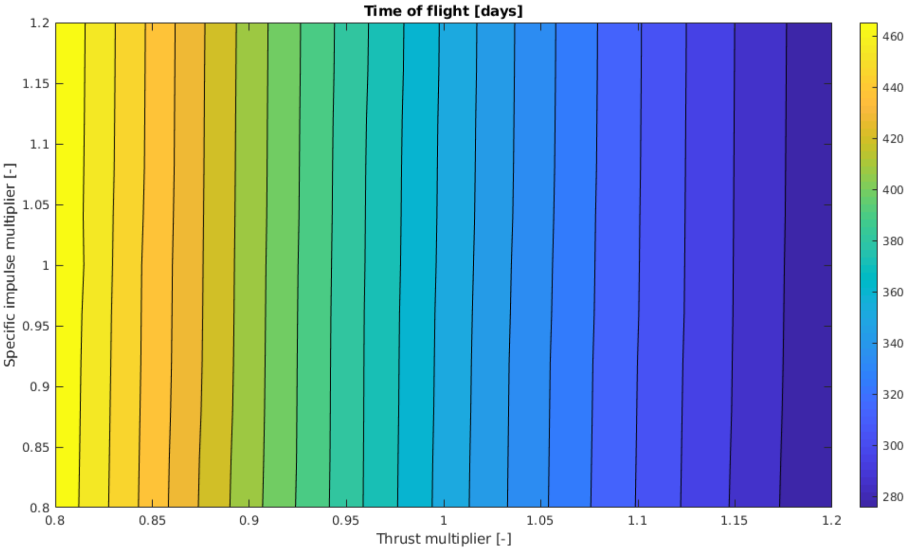

Figure 8.9: Variation of the time of flight of the capture for different values of the specific impulse and thrust magnitude of the spacecraft's low-thrust engine, referenced to their nominal values.

It is also interesting to study the influence of the target orbital parameters. Fig. 8.11 shows the effect of the target eccentricity. As expected, a longer transfer is required to reach smaller eccentricities and orbits closer to a true circular orbit. The difference in time of flight is however not very large, of only a few days, hence a value of 0.05 is a reasonable value to target in a preliminary mission study.

Similarly, targeting an orbit closer to the planet's surface also leads to much longer transfers, as shown in Fig. 8.12, approximately 50 days for an orbit 3,000 kilometers lower. An areostationary orbit, despite being well deep in Mars' gravity field, is still a considerably high orbit, what makes it particularly suitable for a mission design involving ballistic capture and low-thrust stabilization.

A specially important parameter to study that was already introduced before is the magnitude of the possible high-thrust maneuver applied at the first periapsis of the trajectory. According to Fig. 8.13, a very small ΔV

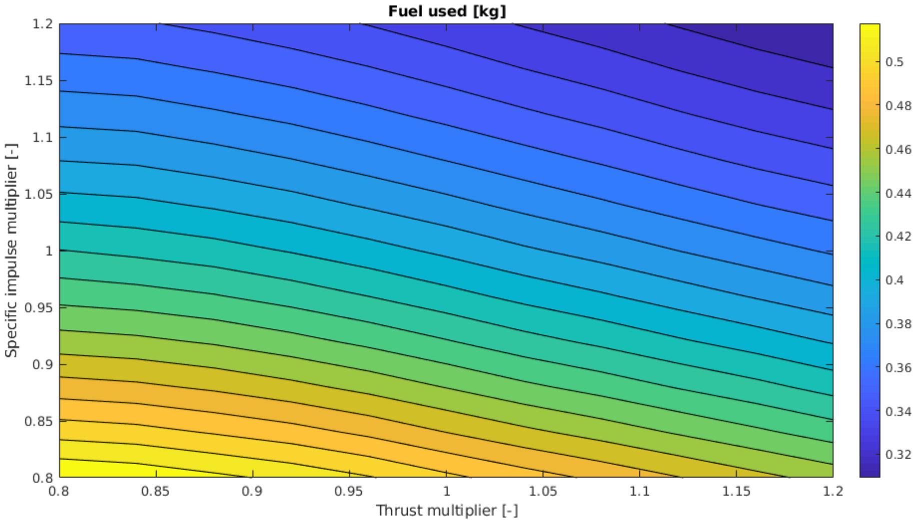

Figure 8.10: Variation of the fuel consumption of the capture for different values of the specific impulse and thrust magnitude of the spacecraft's low-thrust engine, referenced to their nominal values.

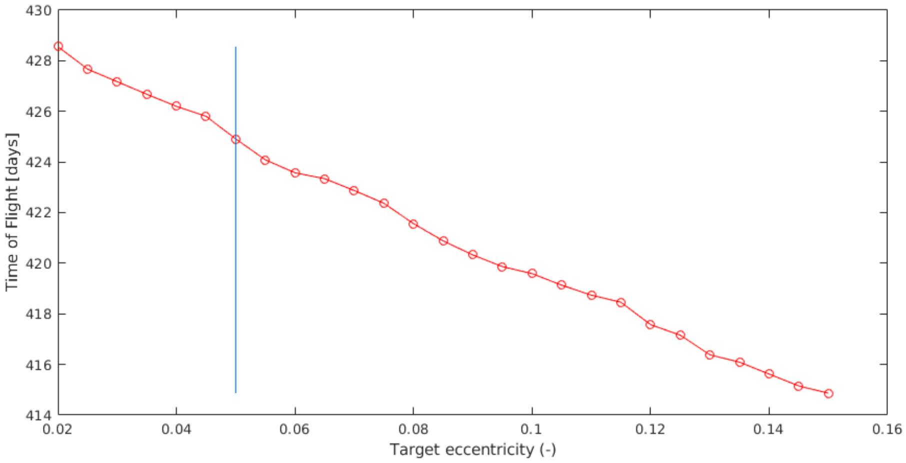

Figure 8.11: Variation of the time of flight of the capture for different values of the target eccentricity. The reference value is shown with a blue line.

of just 5 meters per second can already reduce the time of flight in around one month. Apart from a small bump in the 10 meters per second region, higher ΔV's lead indeed to larger time savings, although with diminishing returns. For 40 meters per second, the time of flight is two months shorter than for the nominal case for a relatively small chemical burn. Fig. 8.14 shows the resulting transfer for 40 meters per second and its comparison with the one with no finite burn. The trajectory is much more contained around Mars, with an initial eccentricity of around 0.95 instead of the original 0.98. This leads to the aforementioned 66 days shaved off the time of flight, and a corresponding saving of 73 grams of low-thrust propellant.

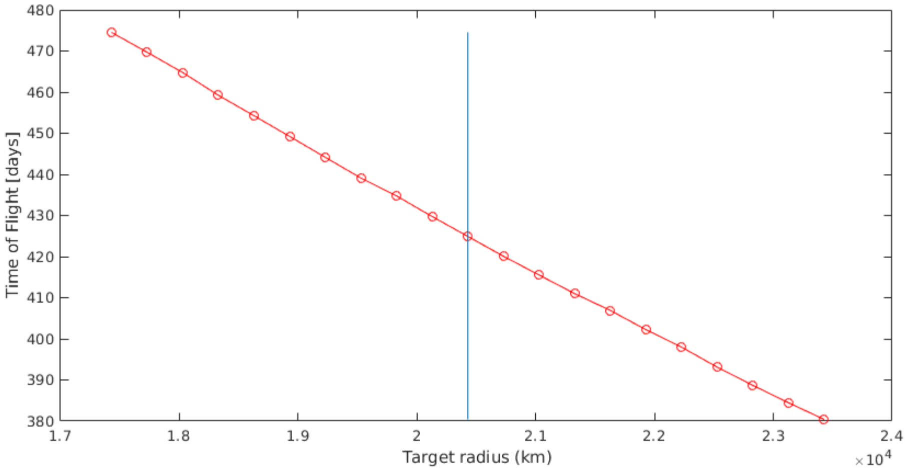

Figure 8.12: Variation of the time of flight of the capture for different values of the target semi-major axis. The reference value is shown with a blue line.

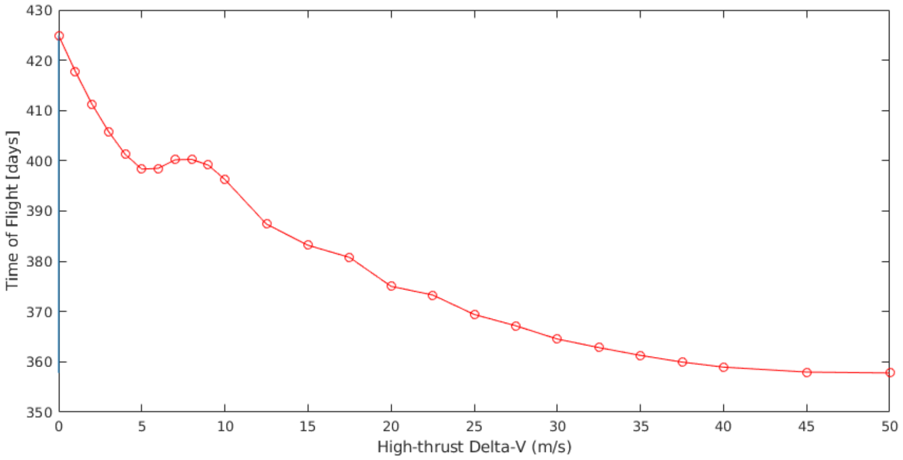

Figure 8.13: Variation of the time of flight of the capture for different values of the high-thrust ΔV applied at the first periapsis. The reference value is shown with a blue line.

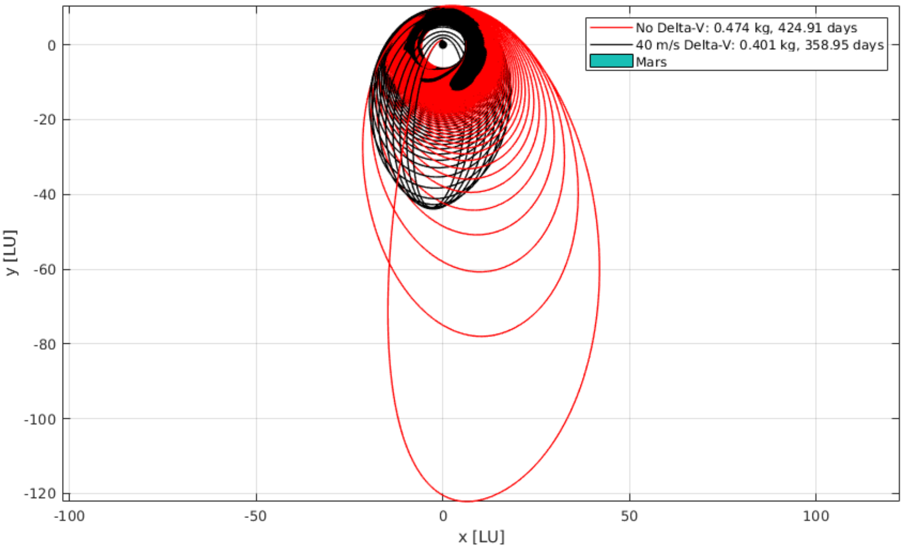

Figure 8.14: Comparison of the stabilized trajectory with no ΔV (in black) and with a ΔV of 40 meters per second (in red), in the IAU-Mars@Epoch.

8.6. STABILIZATION OF THE CAPTURE SETS

In this Section the stabilization of the capture sets generated in Section 4.4 will be studied. Similar to what was done in Chapter 10, all the captures belonging to the set that approach Mars from L_1 will be stabilized to determine which ones lead to a shorter time of flight or lower fuel consumption. In this case, when using control law 4, the time-optimal and fuel-optimal solutions will always coincide, since the engine is always on in the implementation of the Q-law employed. However, and as already pointed out in Section 4.4, it is important to take into account the duration of the ballistic stage from the first entry into the SOI of Mars until the first periapsis where the high-thrust maneuver takes place and the low-thrust control law starts functioning. For this reason, the performance metric employed to characterize the captures will be the total time of flight of the combined ballistic and stabilization phases.

Table 8.3 shows the characteristics of the stabilization trajectories obtained for the different capture sets generated in Section 4.4. Fig. 8.15 shows the capture set colored by the total time of flight as defined above and the capture in this set with the lowest time of flight for the first epoch considered, 08/May/2024.

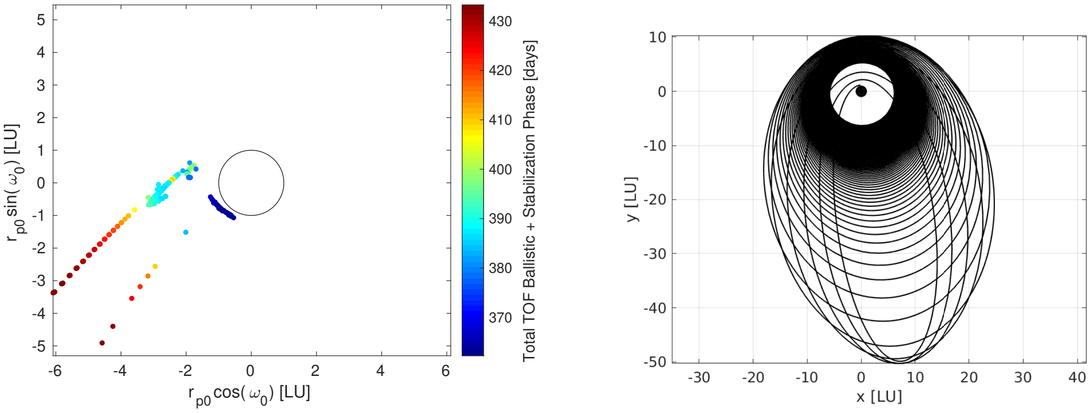

(a)

(b)

Figure 8.15: a) Capture set, colored by time of flight for stabilization, and b) trajectory in the IAU-Mars@Epoch reference frame of the capture with lowest time of flight, for initial epoch 08/May/2024.

Similar to what was done in Chapter 4, the same results are now also shown for the rest of epochs considered in the survey. In particular, Figs. 8.16 and 8.17 show the capture sets, while Figs. 8.18 and 8.19 show the orbit in set with lowest time of flight for the stabilization phase.

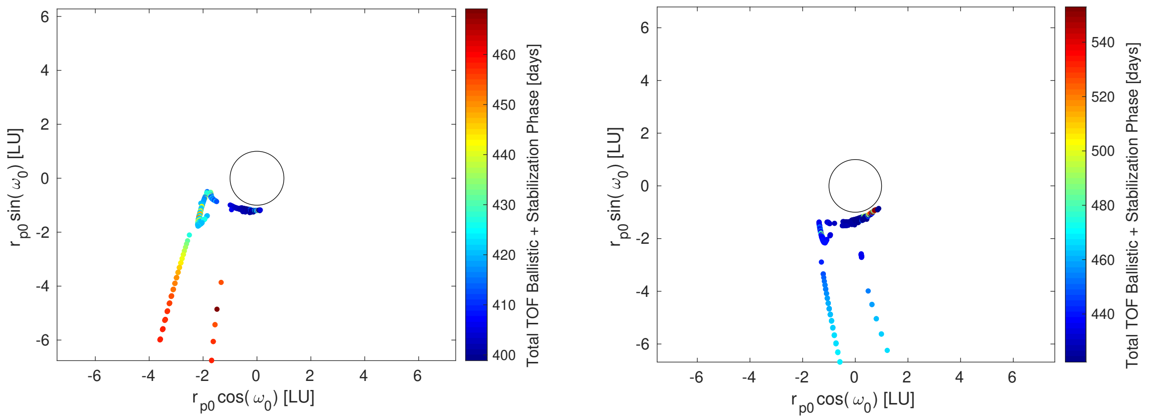

(a) 27/Jun/2024 (b) 16/Aug/2024

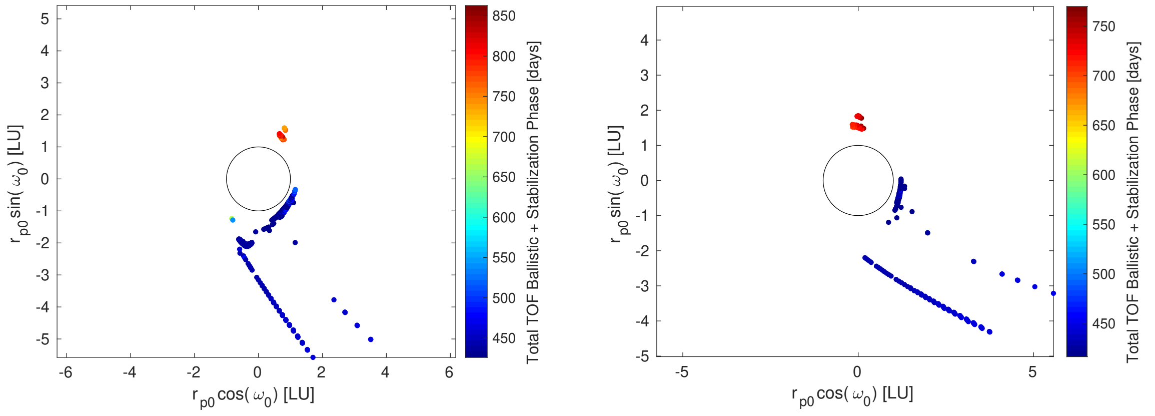

(c) 05/Oct/2024 (d) 24/Nov/2024

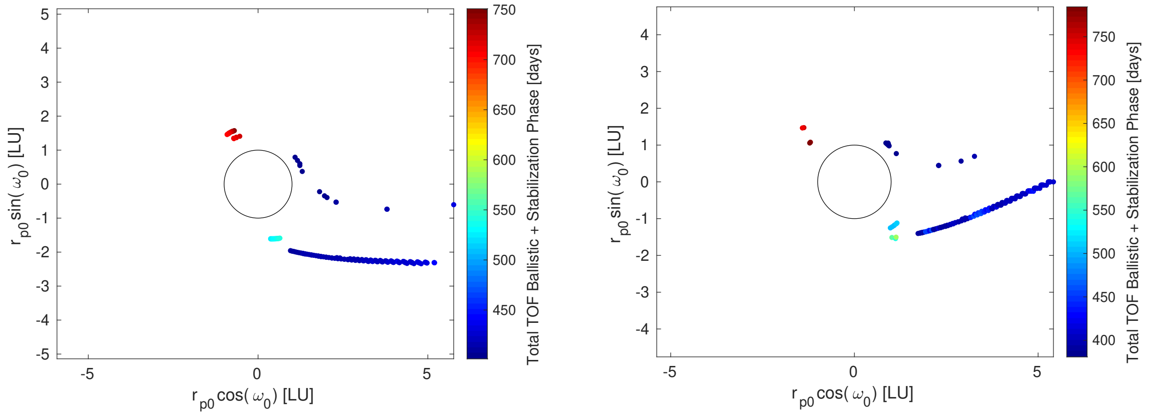

(e) 13/Jan/2025 (f) 04/Mar/2025

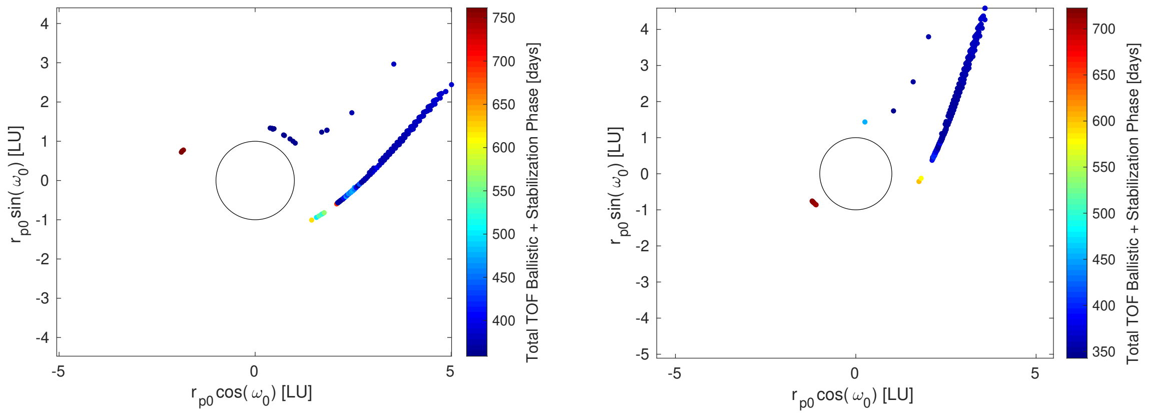

(g) 23/Apr/2025 (h) 12/Jun/2025

Figure 8.16: Capture sets C^1_{-6} at Mars as obtained in Section 4.4, color coded by the total time of flight necessary to stabilize the captures into an areostationary orbit. Only captures coming from L_1 are considered, the black circle with radius 1 DU represents the surface of Mars. [Continues on next page]

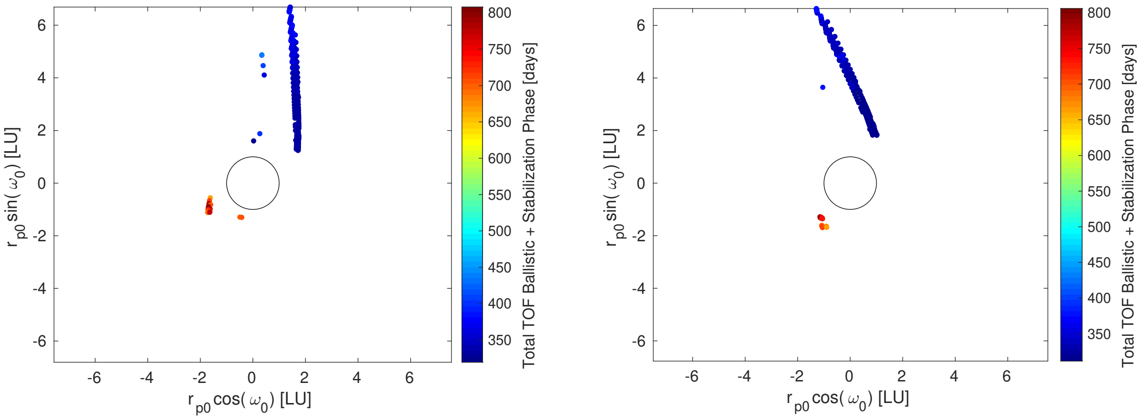

(a) 01/Aug/2025

(b) 20/Sep/2025

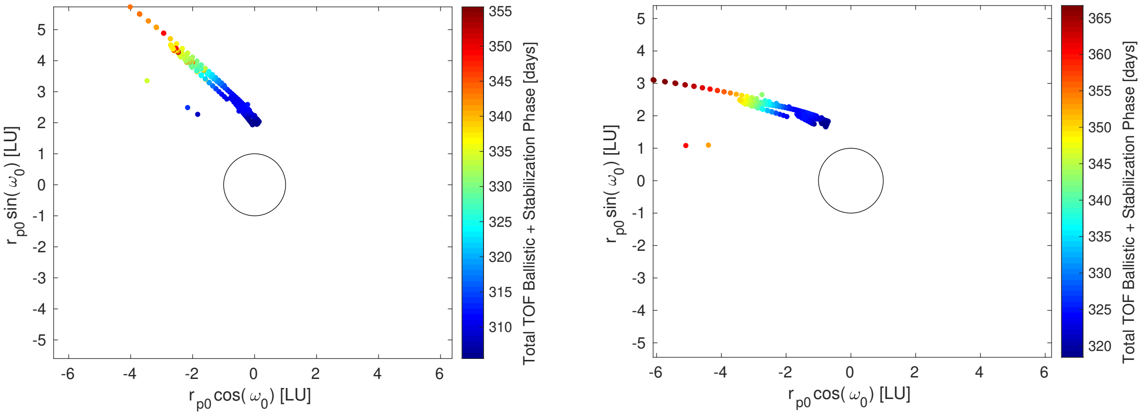

(c) 09/Nov/2025

(d) 29/Dec/2025

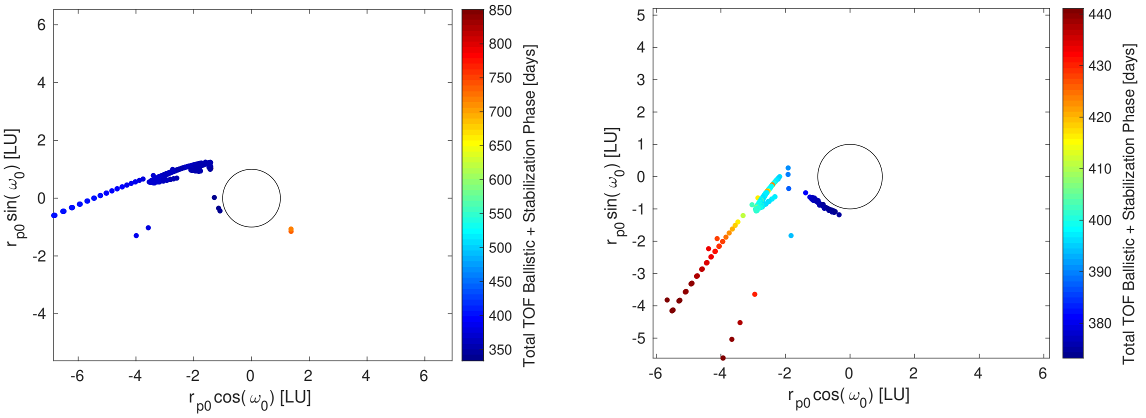

(e) 17/Feb/2026

(f) 08/Apr/2026

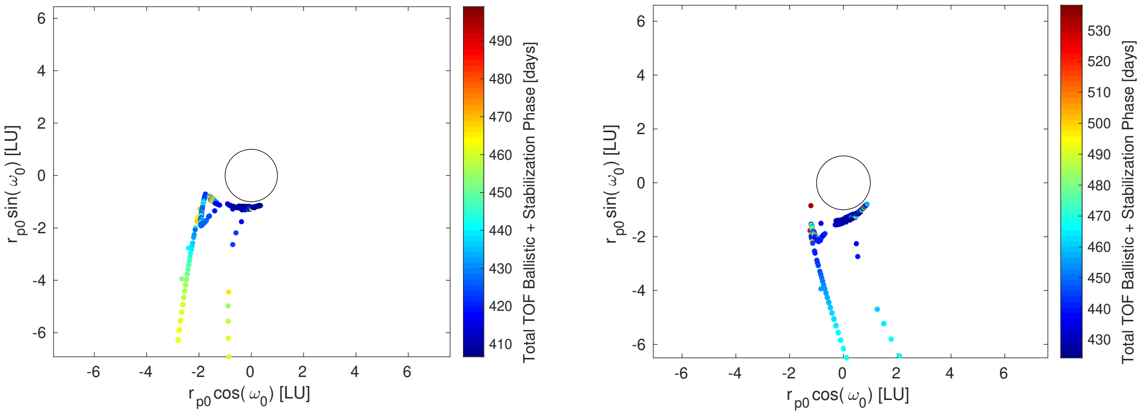

(g) 28/May/2026

(h) 17/Jul/2026

Figure 8.17: Capture sets C^{1}_{-6} at Mars as obtained in Section 4.4, color coded by the total time of flight necessary to stabilize the captures into an areostationary orbit. Only captures coming from L_1 are considered, the black circle with radius 1 DU represents the surface of Mars. [Continues from previous page]

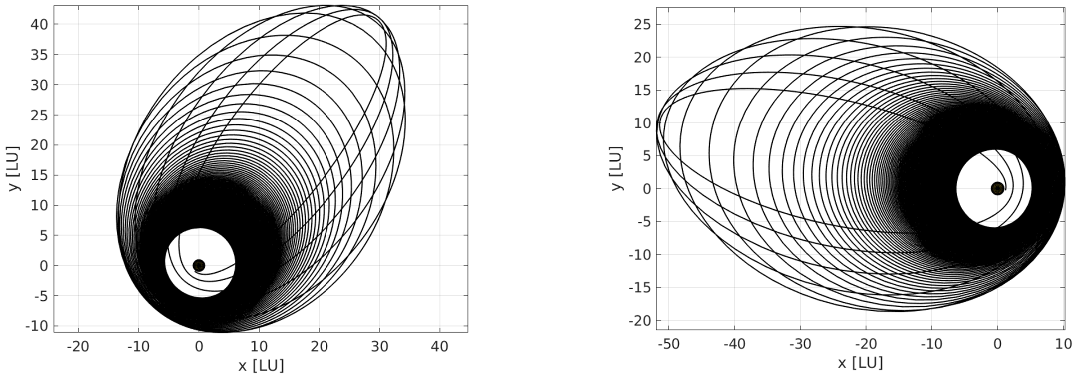

(a) 27/Jun/2024 (b) 16/Aug/2024

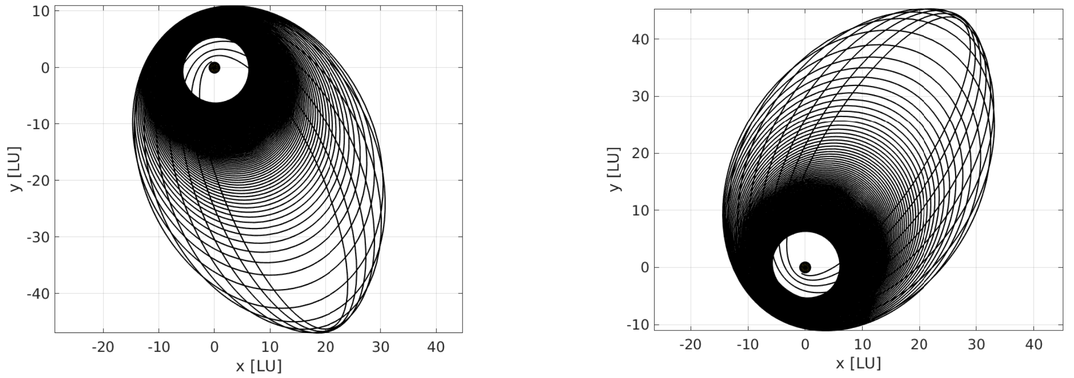

(c) 05/Oct/2024 (d) 24/Nov/2024

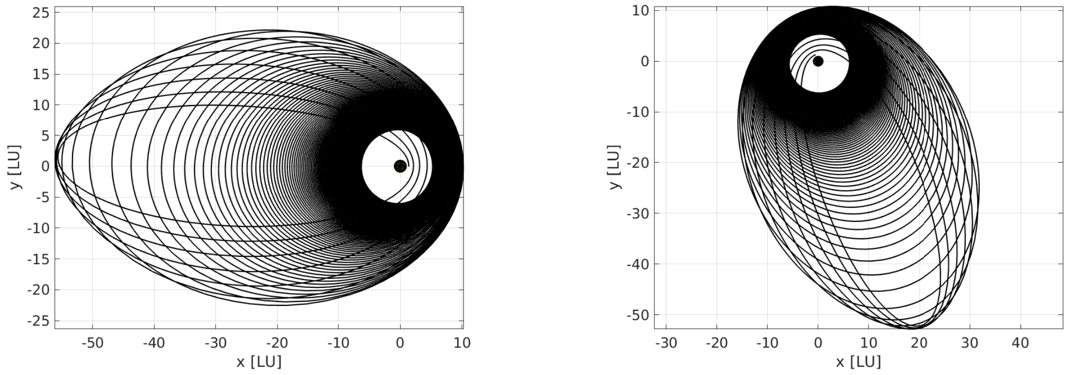

(e) 13/Jan/2025 (f) 04/Mar/2025

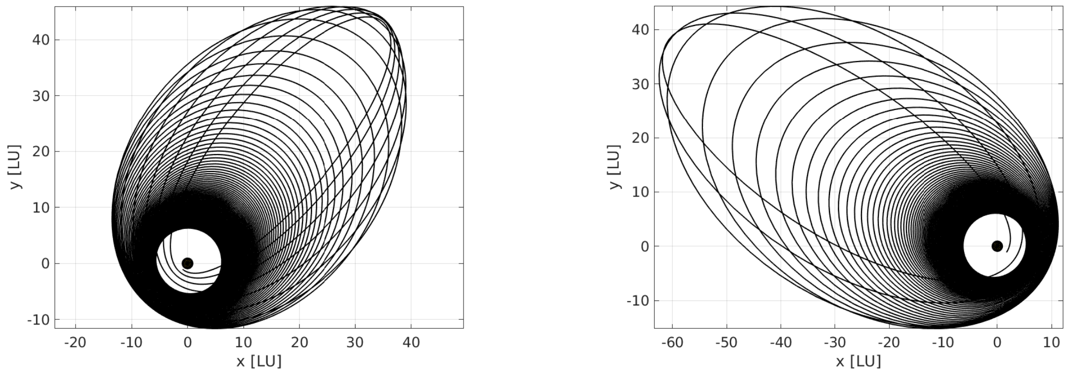

(g) 23/Apr/2025 (h) 12/Jun/2025

Figure 8.18: Trajectory in the IAU-Mars@Epoch reference frame of the capture with lowest total time of flight for stabilization into an areostationary orbits, of the capture sets in Fig. 4.7, for the specified epochs. [Continues on next page]

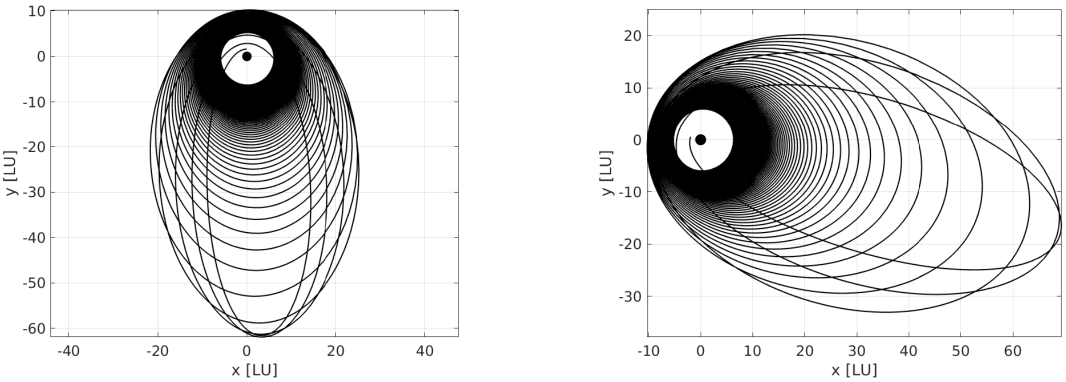

(a) 01/Aug/2025

(b) 20/Sep/2025

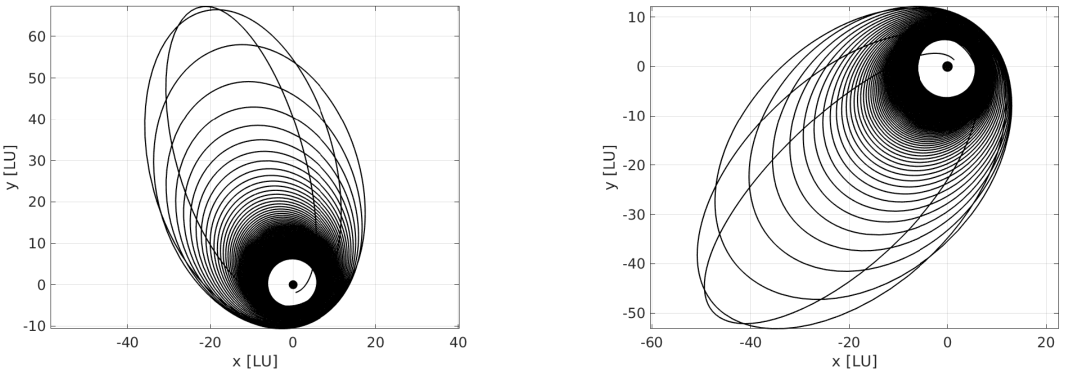

(c) 09/Nov/2025

(d) 29/Dec/2025

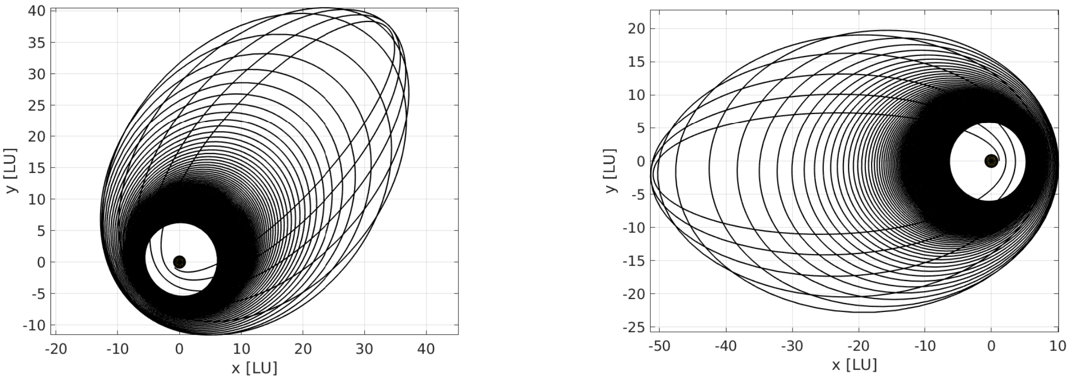

(e) 17/Feb/2026

(f) 08/Apr/2026

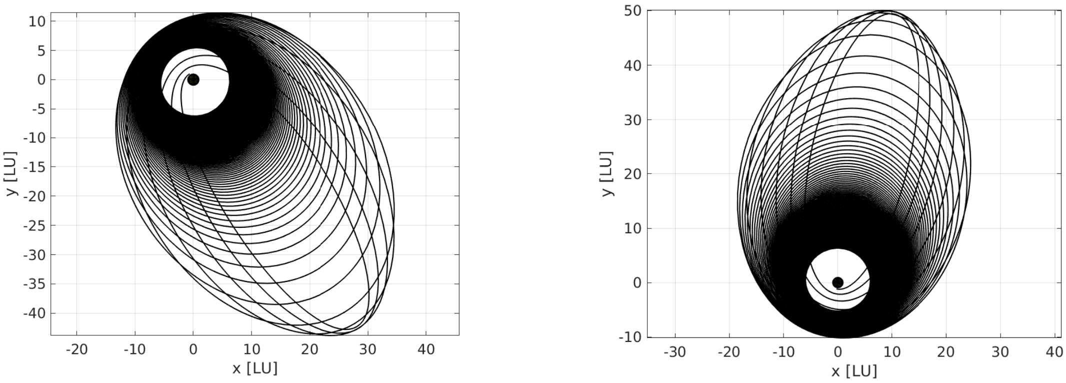

(g) 28/May/2026

(h) 17/Jul/2026

Figure 8.19: Trajectory in the IAU-Mars@Epoch reference frame of the capture with lowest total time of flight for stabilization into an areostationary orbits, of the capture sets in Fig. 4.7, for the specified epochs. [Continues from previous page]

Table 8.3: Characteristics of the stabilization of the C^{1}_{-6} captures generated for different epochs.

Epoch	e_0	i_0 [°]	Ω_0 [°]	M_0 [°]	N_C	$N_{C_{L_1}}$	**Total TOF**	**Stab. TOF**	**Fuel [g]**	ω_0[°]	r_{p_0} [km]
08/May/2024	0.99	25.195°	108.79°	0°	685	347	362.23 days	346.37 days	386.61 g	233°	3996 km
27/Jun/2024	0.99	25.195°	77.32°	0°	727	364	398.85 days	383.02 days	427.62 g	273°	4021 km
16/Aug/2024	0.99	25.195°	47.31°	0°	829	426	422.31 days	406.74 days	454.09 g	292°	4171 km
05/Oct/2024	0.99	25.195°	19.52°	0°	880	447	426.07 days	410.24 days	458.02 g	323°	4021 km
24/Nov/2024	0.99	25.195°	354.00°	0°	503	258	416.34 days	400.68 days	447.33 g	351°	4121 km
13/Jan/2025	0.99	25.195°	330.32°	0°	483	244	401.29 days	386.27 days	431.25 g	16°	4596 km
04/Mar/2025	0.99	25.195°	307.86°	0°	534	268	380.85 days	365.88 days	408.44 g	34°	4671 km
23/Apr/2025	0.99	25.195°	285.97°	0°	659	329	358.85 days	343.82 days	383.76 g	58°	4646 km
12/Jun/2025	0.99	25.195°	263.99°	0°	830	414	342.71 days	329.06 days	367.22 g	59°	6896 km
01/Aug/2025	0.99	25.195°	241.27°	0°	1386	677	319.42 days	305.10 days	340.44 g	89°	5446 km
20/Sep/2025	0.99	25.195°	217.16°	0°	1762	864	311.73 days	297.94 days	332.42 g	65°	6846 km
09/Nov/2025	0.99	25.195°	191.07°	0°	1493	740	305.51 days	291.70 days	325.45 g	93°	6771 km
29/Dec/2025	0.99	25.195°	162.66°	0°	1270	632	318.44 days	304.49 days	339.75 g	115°	6471 km
17/Feb/2026	0.99	25.195°	132.14°	0°	1033	508	333.21 days	317.37 days	354.16 g	202°	3996 km
08/Apr/2026	0.99	25.195°	100.51°	0°	665	327	373.23 days	357.41 days	398.97 g	241°	4021 km
28/May/2026	0.99	25.195°	69.30°	0°	849	463	406.66 days	390.80 days	436.31 g	267°	4021 km
17/Jul/2026	0.99	25.195°	39.82°	0°	814	416	424.15 days	408.38 days	455.93 g	306°	4046 km

- e_0, i_0, Ω_0, M_0: Initial eccentricity, inclination, longitude of the ascending node and mean anomaly.
- N_C: Total number of captures in the capture set.
- $N_{C_{L_1}}$: Number of captures approaching Mars from L_1.
- **Total TOF**: Minimum Total Time of Flight for stabilization (including ballistic phase) for captures coming from L_1.
- **Stab. TOF**: Time of flight of the stabilization phase of the capture with minimum total TOF.
- **Fuel mass**: Fuel mass for the capture with minimum total TOF.
- ω_0, r_{p_0}: Argument of periapsis and radius of periapsis of the capture with minimum total time of flight.

Fig. 8.20 shows the evolution over time of the time of flight of the stabilization as well as the total time of flight including the ballistic phase. A cyclical nature over the course of Mars orbit around the Sun can clearly be seen, with a minimum TOF occurring in late 2015, when Mars has just passed its aphelion around the Sun. Curiously enough, this evolution is almost the opposite of the minimum stability index seen in Fig. 4.11.

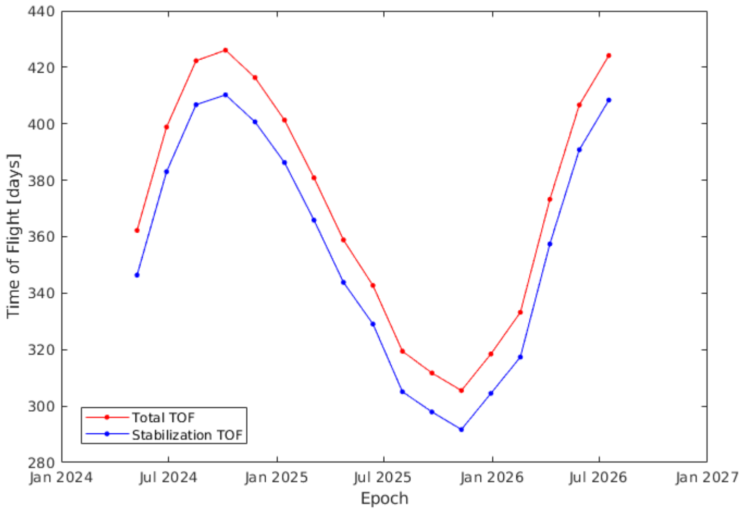

Figure 8.20: Evolution of the stabilization and total time of flight over the different epochs considered.

VI

HELIOCENTRIC LOW-THRUST TRANSFER

9

METHODOLOGY

9.1. INTRODUCTION

The present Chapter will present the methodology employed to target the capture sets generated in Chapter 4 from Earth using low-thrust propulsion. Section 9.2 will describe the problem statement, mainly the assumptions made with regard to the spacecraft, in particular the characteristics of the engine. Section 9.3 will introduce the reference frames used to study this stage of the mission. The dynamics of the problem and the equations of motion, first element necessary to define the Optimal Control problem, are presented in Section 9.4. Section 9.5 will present the remaining elements of the optimization problem, i.e. the path and boundary constraints and the performance index or indexes employed. Finally, Section 9.6 will introduce how to transcribe the problem using Nonlinear Programming (NLP) theory, and Section 9.7 will outline some aspects regarding the computational implementation of this methodology and the tool employed to obtain the results of Chapter 10.

9.2. PROBLEM STATEMENT

Section 3.2 already described some of the characteristics of the mission and potential satellite design of a 16U CubeSat traveling to an areostationary orbit around Mars. A cross-sectional surface area of $0.52\,\mathrm{m}^2$ will be employed again. The estimated total wet mass for MARIO, including a 20% system margin, is 29.9 kg. It will be assumed that 6.6 kg of chemical propellant are employed to escape Earth, an approximate number for the fuel consumption when using a bi-propellant thruster in Chapter 6. Hence, the initial mass for the heliocentric leg of the trajectory will be considered to be 23.3 kg. The characteristics of the low-thrust engine will be those already used for the stabilization stage and described in Section 7.2.

It is also necessary to specify some aspects regarding the design of the trajectory itself. The initial conditions at the time of departure from the SOI of the Earth, t_d, will be:

- The position of the spacecraft will be that of the Earth plus the radius of its Sphere of Influence (SOI), R_{SOI_E}, displaced in the direction opposite to the Sun.
- The velocity of the spacecraft will be that of the Earth with respect to the Sun plus any hyperbolic excess

velocity from the escape from Earth. The same value that was used in Chapter 6 will be used here, that is, $v_\infty = 100\,\mathrm{m/s}$. For simplicity, it will be assumed that this velocity is located in the orbital plane of the Earth and points in the same direction as the velocity of the Earth with respect to the Sun.

9.3. REFERENCE FRAMES

Two different reference frames will be used simultaneously in the integration of the equations of motion during the heliocentric phase. It is important when working with optimal control problems to have state and control variables that change slowly. For this reason, the position and velocity of the spacecraft will be expressed in two different frames.

The position will employ the Heliocentric Earth Orbital frame at Epoch (HEO@Epoch) $(\boldsymbol{e_x}, \boldsymbol{e_y}, \boldsymbol{e_z})$, a non-rotating frame centered at the Sun equivalent to the RTN@Epoch. The x-axis $\boldsymbol{e_x}$ will point towards the Earth aligned with the Sun-Earth line, and $\boldsymbol{e_z}$ is aligned with the Earth's angular momentum. The position will be expressed in this frame using spherical coordinates, (r, θ, ϕ). Fig. 9.1 shows the definition of this frame and the spherical coordinates above.

Similar to what was done in Section 7.3, velocity will use the Spacecraft Range-Azimuth-Elevation (SRAE) $(\boldsymbol{e_r}, \boldsymbol{e_\theta}, \boldsymbol{e_\phi})$, which is a rotating frame centered at the spacecraft. Its definition is also shown in Fig. 9.1, where it can be seen that two rotations around the two angles defined in the spherical coordinates above (θ and ϕ) are employed to obtain the reference frame. The thrust vector will also be expressed in this frame, employing the spherical coordinates (T, α, β) shown in Fig. 9.1.

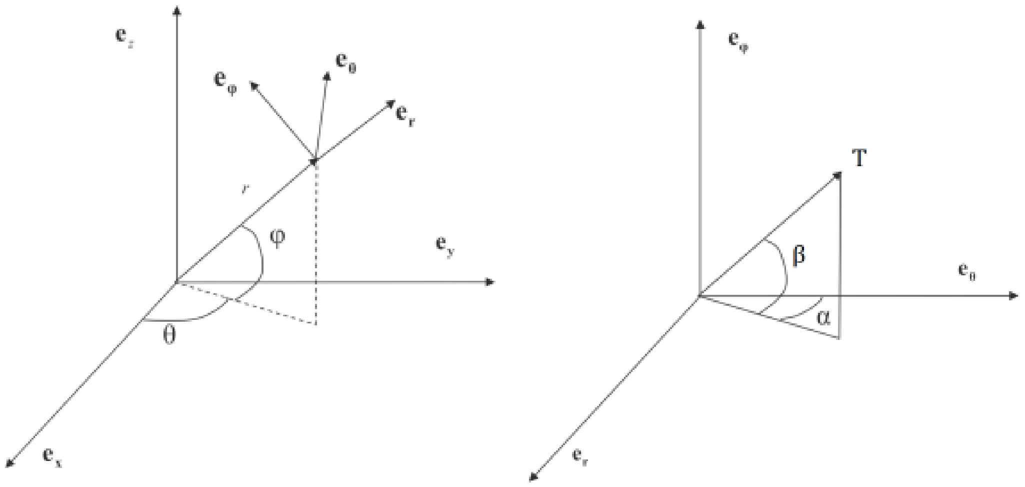

Figure 9.1: Orientation of Heliocentric Earth Orbital frame at Epoch (HEO@Epoch) and SRAE and definition of the spherical coordinates in HEO@Epoch (left), and definition of the spherical coordinates of the thrust in SRAE (right) [37].

9.4. SPACECRAFT DYNAMICS AND EQUATIONS OF MOTION

The dynamics model of the system, defined by a set of equations of motion, will be the first element that will form the optimal control problem. Unlike in Section 3.4, where Mars was the central body, the spacecraft will now be outside of the SOI of both the Earth and Mars, and hence the Sun is the most logical choice as the central body to be used.

Another important difference with respect to the case of ballistic capture is that dynamical perturbations with respect to the Two-Body Problem or the CRTBP are now not the main driver behind the motion of the spacecraft, given that low-thrust propulsion is used to control the trajectory. With that in mind, a simple Two-Body Problem will be employed for most simulations, but the results will be compared with a detailed Restricted n-Body Problem (RnBP).

The Optimal Control Problem will include seven state variables, $(r, \theta, \phi, v_r, v_\theta, v_\phi, m)$ and three control variables, (T, α, β). The equations of motion that express the evolution of the state variables are as follow [37]:

$$\frac{\mathrm{d}}{\mathrm{d}t}\begin{Bmatrix} r \\ \theta \\ \phi \end{Bmatrix} = \begin{Bmatrix} v_r \\ \frac{v_\theta}{r\cos\phi} \\ \frac{v_\phi}{r} \end{Bmatrix} \tag{9.1}$$

for the position, and

$$\frac{\mathrm{d}}{\mathrm{d}t}\begin{Bmatrix} v_r \\ v_\theta \\ v_\phi \end{Bmatrix} = P\boldsymbol{f_{2B}} + S\begin{Bmatrix} v_r \\ v_\theta \\ v_\phi \end{Bmatrix} + \boldsymbol{f_T} = \begin{Bmatrix} -\frac{GM_S}{r^2} \\ 0 \\ 0 \end{Bmatrix} + \begin{Bmatrix} \frac{v_\theta^2+v_\phi^2}{r} \\ \frac{v_\theta(v_\phi\tan\phi - v_r)}{r} \\ -\frac{v_r v_\phi + v_\theta^2\tan\phi}{r} \end{Bmatrix} + \boldsymbol{f_T} \tag{9.2}$$

for the velocity. In this equation, $\boldsymbol{f_{2B}}$ represents the Two-Body gravitational attraction in a non-rotating reference frame and the second term accounts for the rotation of the spacecraft-centered reference frame, while $\boldsymbol{f_T}$ is indeed the force per unit mass provided by the low-thrust engine. Matrices P and S were already introduced in the study of the stabilization phase, and their expressions can be seen in Eqs. (7.3) and (7.5), respectively.

If third-body perturbations and SRP are introduced, Equation (9.2) will become

$$\frac{\mathrm{d}}{\mathrm{d}t}\begin{Bmatrix} v_r \\ v_\theta \\ v_\phi \end{Bmatrix} = P(\boldsymbol{f_{2B}} + \boldsymbol{f_{TB}} + \boldsymbol{f_{SRP}}) + S\begin{Bmatrix} v_r \\ v_\theta \\ v_\phi \end{Bmatrix} + \boldsymbol{f_T} \tag{9.3}$$

The thrust force per unit mass will in any case be computed as:

$$\boldsymbol{f_T} = \frac{T}{m}\begin{Bmatrix} \sin\alpha\cos\beta \\ \cos\alpha\cos\beta \\ \sin\beta \end{Bmatrix} \tag{9.4}$$

where α and β are the azimuth and elevation of the thrust, respectively, in the spherical coordinates defined in Fig. 9.1.

The only equation missing to compute the evolution of the state variables of the problem is the variation of the spacecraft mass. This can be expressed as follows:

$$\frac{\mathrm{d}m}{\mathrm{d}t} = -\frac{T}{I_{sp}g_0} \tag{9.5}$$

where $g_0 = 9.80665\ m/s^2$ is the gravitational acceleration on the surface of the Earth.

Equation 9.5 along with Equations 9.1 and 9.2 or 9.3 will complete the set of equations of motion of the system.

9.5. CONSTRAINTS AND PERFORMANCE INDEX OF THE OPTIMAL CONTROL PROBLEM

Once the equations of motion and dynamical model have been established in the previous Section, three elements are missing to construct the Optimal Control Problem, i.e. the path and boundary constraints and the performance index.

As outlined in Section 2.3, boundary constraints express the initial and final state of the system and represent the task description of the problem. The initial state has already been assumed in Section 9.2, with a set initial mass, position and velocity at time of departure t_d. These initial conditions are contained in the following expression:

$$\Psi_d(\boldsymbol{x}(t_d), t_d) \equiv \left\{ \begin{array}{c} t_d - (t_0 - \Delta t_{TOF}) \\ r(t_d) - (r_E(t_d) + R_{SOI_E}) \\ \theta(t_d) \\ \phi(t_d) \\ v_r(t_d) - v_{r_E}(t_d) \\ v_\theta(t_d) - (v_{\theta_E}(t_d) + v_\infty) \\ v_\phi(t_d) \\ m(t_d) - m_{wet} \end{array} \right\} = \mathbf{0} \tag{9.6}$$

where:

- The first component represents the departure time being equal to the epoch of the first periapsis at Mars, t_0, minus the total Time of Flight (TOF) of the heliocentric transfer.
- The following three correspond to the initial position of the spacecraft, which is that of the Earth plus the radius of the SOI in the direction opposite from the Sun. Note that both θ and ϕ are zero given the definition of the reference frame used.
- The following three represent the initial velocity of the spacecraft, which is the same as that of the Earth with respect to the Sun plus the aforementioned excess velocity v_∞. Again, the component v_ϕ is zero given the definition of HEO@Epoch.
- Finally, the last component represents the initial mass of the spacecraft, which was already established in Section 9.2.

On the other hand, final boundary constraints will consider a free final epoch for the transfer, t_f, which corresponds to the time when the spacecraft reaches a state that leads to ballistic capture around Mars and should not be confused with t_0. Because t_f is free to be optimized, the final conditions are expressed with respect to a spline constructed from the backwards propagation of the captures as described in Chapter 4. The following expressions contain the final conditions of the problem:

$$\Psi_f(\boldsymbol{x}(t_f), t_f) \equiv \left\{ \begin{array}{c} r(t_f) - r_c(t_f) \\ \theta(t_f) - (\theta_c(t_f) + 2\pi\Delta n) \\ \phi(t_f) - \phi_c(t_f) \\ v_r(t_f) - v_{r_c}(t_f) \\ v_\theta(t_f) - v_{\theta_c}(t_f) \\ v_\phi(t_f) - v_{\phi_c}(t_f) \end{array} \right\} = \mathbf{0} \tag{9.7}$$

where all components represent that the final position and velocity of the spacecraft are those of the captured state at the same epoch t_f. In practice, all values with subscript c will be computed using the aforementioned spline describing the backwards propagation of the capture. Δn will determine the number of extra revolutions that the spacecraft performs in the transfer.

Apart from Equation 9.7, the final mass of the spacecraft $m(t_f)$ will be free, and an extra boundary constraint, in this case an inequality, is needed:

$$\Psi_t(t_f) = t_f - t_\infty \leq 0 \tag{9.8}$$

which simply means that the epoch t_f is restricted by the epoch at which the spacecraft enters Mars SOI for the first time, t_∞.

The path constraints are those that are enforced along the whole trajectory, and are expressed as inequalities including the state and control variables:

$$\boldsymbol{G}(\boldsymbol{x}(t), \boldsymbol{u}(t)) \equiv \left\{ \begin{matrix} T(t) - 1.24\ \text{mN} \\ T(t) - T^*(r) \\ \alpha(t) - \pi \\ -\pi - \alpha(t) \\ \beta(t) - \pi/2 \\ -\pi/2 - \beta(t) \\ 0.1 r_d - r(t) \\ m(t) - m_{wet} \\ 1\ kg - m(t) \end{matrix} \right\} \leq \boldsymbol{0} \tag{9.9}$$

where:

- The first two constraints limit the maximum thrust available to the engine.
- The following four represent simple bounds for the thrust angles α and β.
- A constraint for the radius prevents the spacecraft from going very close towards the Sun which is indeed undesirable when targeting Mars.
- Finally, two boundaries are enforced for the spacecraft mass, both these and the one for r are included to help with convergence of the optimizer.

The last element required to define the Optimal Control Problem is the performance index. Two different ones will be considered: $J = -m_f$ for the fuel-optimal problem, and $J = t_f$ for the time-optimal problem. The way these are defined, the optimal solutions found will always have zero or maximum thrust, which in turn means that the spacecraft will always use the maximum specific impulse [25]. It should be noted that the time-optimal problem is in reality minimizing the TOF of the powered leg of the trajectory, since it includes the moment the spacecraft reaches the ballistic capture spline (t_f) instead of the first periapsis around Mars (t_0).

9.6. TRANSCRIBED NLP PROBLEM

This Section will introduce the direct collocation used to transcribe the Optimal Control Problem described in the previous Section into an NLP problem. The time interval of the transfer will be discretized into N nodes, the control variables will be interpolated between two nodes and the state variables will be made continuous by employing defect constraints $\boldsymbol{\zeta}$.

$$t_d = t_1 < t_2 < \cdots < t_N = t_f \qquad \boldsymbol{u}(t_k) \equiv \boldsymbol{u_k} \qquad \boldsymbol{x}(t_k) \equiv \boldsymbol{x_k} \tag{9.10}$$

$$t_k \le t \le t_{k+1} \qquad \boldsymbol{u}(t) \equiv \boldsymbol{u_k} + \frac{t - t_k}{t_{k+1} - t_k}(\boldsymbol{u_{k+1}} - \boldsymbol{u_k}) \qquad \boldsymbol{\zeta_k}(\boldsymbol{x_k}, \boldsymbol{x_{k+1}}, \boldsymbol{u_k}, \boldsymbol{u_{k+1}}, t_k, t_{k+1}) = \boldsymbol{0} \tag{9.11}$$

Once a number of nodes is fixed, the equations of the NLP problem can be defined. The defect constraints will use the Hermite-Simpson method:

$$\boldsymbol{\zeta_k} \equiv \boldsymbol{x_{k+1}} - \boldsymbol{x_k} - \frac{h_k}{6}(\boldsymbol{F_k} + 4\boldsymbol{F_c} + \boldsymbol{F_{k+1}}) \tag{9.12}$$

$$\boldsymbol{F_k} \equiv \boldsymbol{F}(\boldsymbol{x_k}, \boldsymbol{u_k}, t_k) \qquad \boldsymbol{F_c} \equiv \boldsymbol{F}(\boldsymbol{x_c}, \boldsymbol{u_c}, tc) \qquad \boldsymbol{F_{k+1}} \equiv \boldsymbol{F}(\boldsymbol{x_{k+1}}, \boldsymbol{u_{k+1}}, t_{k+1}) \tag{9.13}$$

$$\boldsymbol{x_c} \equiv \frac{1}{2}(\boldsymbol{x_k} + \boldsymbol{x_{k+1}}) + \frac{h}{8}(\boldsymbol{F_k} - \boldsymbol{F_{k+1}}) \qquad t_c \equiv t_k + \frac{h}{2} \qquad h \equiv t_{k+1} - t_k \tag{9.14}$$

$$\boldsymbol{u_c} \equiv \boldsymbol{u}(t_c) = \frac{1}{2}(\boldsymbol{u_k} + \boldsymbol{u_{k+1}}) \tag{9.15}$$

9.7. COMPUTATIONAL IMPLEMENTATION

Similar to the GRATIS tool employed in Chapter 4, another *MATLAB* tool developed in [25] and updated in several works since will be used in this Chapter. DIRETTO employs as stated above a Hermite-Simpson method to derive the defect constraints and construct an NLP problem that can be solved with the popular optimization interior-point method solver IPOPT [1]. The number of nodes used to define the NLP problem will be $N = 400$ for all simulations in this work. An interior point algorithm is particularly suitable for large, sparse problems. Gradients are provided for both the objective function and all the constraints. When analytical derivatives cannot be provided, numerical differences are constructed to be supplied to the optimizer. For all optimization runs in this work, the following tolerances will be enforced:

- Step tolerance: 10^{-6}
- Constraints tolerance: 10^{-12}
- First-order optimality and function value tolerance: 10^{-6}

When one of these tolerances reaches the threshold, the optimization is finished. On the other hand, a maximum value of 5,000 iterations and 500,000 function evaluations will be enforced.

As in Part III, scaling parameters will be used to make all variables dimensionless. In this case, the scaling variables will be:

- **Length Unit:** $LU = 1$ AU
- **Standard Gravitational Parameter Unit:** $\frac{LU^3}{TU^2} = \mu_S$
- **Time Unit:** $TU = \sqrt{\frac{LU^3}{\mu_S}}$ (approximately 58.1 days)
- **Mass Unit:** $MU = m_0$ (initial mass of the spacecraft)

---

[1] `https://projects.coin-or.org/Ipopt`

10

VERIFICATION AND RESULTS

10.1. INTRODUCTION

In this Chapter, the results of the study of the heliocentric phase will be shown. Section 10.2 will present a verification of the methodology and tools outlined in the previous Chapter. Section 10.3 will show how the captures selected in Chapter 8 are targeted with fuel-optimal transfers for different times of flight. Section 10.4 will extend the model of the transfers to a real solar system ephemeris model instead of two-body dynamics. Finally, Section 10.5 will explore the effect of varying the hyperbolic excess velocity at the SOI of the Earth.

10.2. VERIFICATION

The direct transcription and NLP solution methodology behind DIRETTO and the tool itself have already been verified on existing literature employing the tool [10, 25]. For that reason, the verification procedure here will be limited to the solution of a specific case using a different number of nodes for the definition of the NLP problem.

A transfer from Earth to a ballistic capture spline at Mars will be solved with two-body dynamics and an engine with constant thrust and specific impulse (equal to the maximum values defined in Section 9.2). In particular, the capture selected in 8.6 for epoch $t_{01} + 400$ days (12/Jun/2025) will be targeted with a time of flight of 1,400 days. For reference, this transfer will be known as (c) in the following Sections and will be studied in detail.

This transfer is here targeted using a different number of nodes for the direct transcription into an NLP problem. Values lower and larger than the nominal value of $N = 400$ will be used. The results are shown in Table 10.1. The trajectories and control history are not shown for brevity because they are basically identical regardless of the number of nodes. The plots for the nominal value of N can be seen in Fig. 10.5 and 10.6. For larger values of N, the fuel consumption is slightly lower, but the accuracy is already very good when using 400 nodes. Increasing this number to 1,600 only brings an improvement of 0.03 grams, or 0.0005% of the fuel used for the transfer. For this reason, and because the computational time seems to increase drastically for larger values of N, the nominal value will be considered appropriate. Besides, this brief experiment shows that the methodology and tool employed are as could be expected independent of N, even for relatively small numbers like 100 nodes.

Table 10.1: Verification of the optimization of a heliocentric transfer to a capture in Mars with arrival epoch $t_{01}+400$ days and time of flight of 1400 days, employing different values of the number of nodes.

Number of nodes	**Fuel [kg]**	**Transfer time [days]**	**Comp. time [s]**
100	5.36009 kg	1370.90 days	4.77 s
200	5.35947 kg	1370.97 days	5.72 s
400 (nominal)	5.35934 kg	1371.04 days	17.8 s
800	5.35932 kg	1371.13 days	239.8 s
1600	5.35931 kg	1371.08 days	280.0 s

10.3. TARGETING THE CAPTURES AT MARS

Fuel-optimal transfers will be constructed to target all captures selected in Chapter 8 at their corresponding arrival times t_0. Considering a discretization of several values for the time of flight, a grid of departure and arrival dates can be constructed showing the fuel-optimal transfers available from Earth to the capture states at Mars. The same grid for the arrival date employed in Chapters 4 and 8 will be used now. The time of flight of the heliocentric transfer, defined as the time since the spacecraft leaves the SOI of the Earth t_d until it reaches the first periapsis at Mars, t_0. Epoch t_f marks the time when the spacecraft reaches the spline defining the capture trajectory and the low-thrust control is not necessary anymore. The spacecraft will reach the periapsis from that point ballistically. It should be noted that for all simulations performed in this Section the dynamics of the Two-Body Problem will be employed.

Fig. 10.1 shows the propellant consumption of the heliocentric transfer, $\Delta m = m(t_d) - m(t_f)$, for the complete grid of arrival epochs and total time of flight. The minimum fuel consumption is reached for the last epoch, $t_{01}+800$ days (17/Jul/2026), and a time of flight of 2100 days. The fuel consumption is then 4.14 kg. However, most of the plot actually shows a very similar required propellant mass.

The white region in Fig. 10.1 represents combinations of t_0 and TOF that lead to unfeasible transfers. Given the rather coarse discretization used (50 days for both variables), the limit of the unfeasible region could in fact be obtained by finding time-optimal transfers for each specific arrival date [10]. There are two fuel-optimal transfers with a time of flight of only 1200 days, with $t_0 = t_{01} + 100$ days (16/Aug/2024) and $t_0 = t_{01} + 150$ days (05/Oct/2024).

The fuel consumption only rises significantly when the time of flight is very close to the optimal, particularly for certain epochs close to t_{01}. Low-thrust propulsion is very efficient and flexible and barely depends on the relative positioning of the Earth and Mars as long as there is enough time for the control to adjust. Only when very fast transfers close to the minimum feasible TOF are sought the fuel consumption increases significantly.

Fig. 10.2 shows the final value of the angle θ over the grid. This plot shows two discontinuities clearly seen by the accumulation of contour lines and a rapid change of the value of $\theta(t_f)$. These two discontinuities are very important because they represent a region of the $\{t_0, \text{TOF}\}$ space where the spacecraft either speeds up to reach Mars in one revolution less or slows down to reach it in one more. In fact, if the problem is thought of as cyclical with the synodic period of Earth and Mars (which is particularly true when using two-body dynamics), it can be seen how the two discontinuities are in fact a continuation of each other and at the same time of the feasibility boundary starting to the right of $t_{01} + 150$ days (05/Oct/2024).

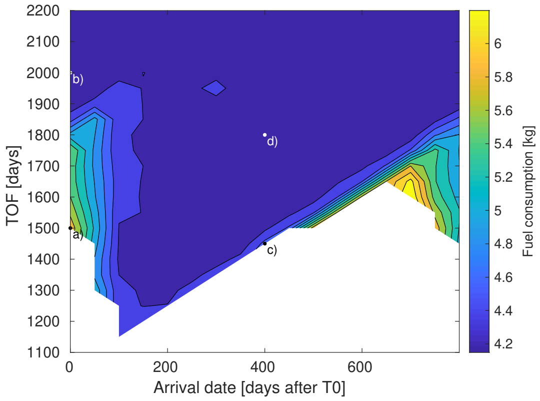

Figure 10.1: Propellant consumption for fuel-optimal heliocentric transfers to ballistic capture at Mars, as a function of the arrival date and the total time of flight.

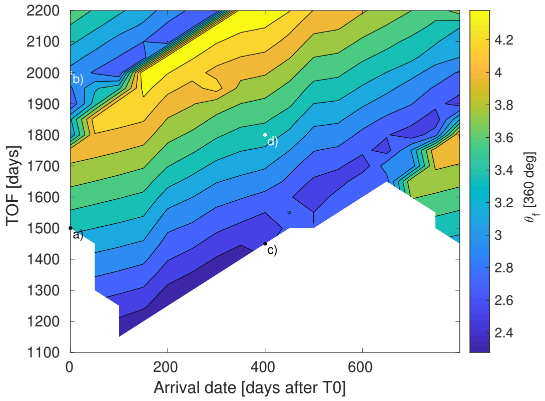

Figure 10.2: $\theta(t_f)$ for fuel-optimal heliocentric transfers to ballistic capture at Mars, as a function of the arrival date and the total time of flight.

Fig. 10.3 shows the value of $\Delta r = r(t_f) - r(t_d)$, that is, the distance traveled by the spacecraft in the radial direction. The plot is somewhat chaotic, but certain trends can be seen. The higher values are reached around $t_{01} + 400$ days (12/Jun/2025), what makes sense since that corresponds to the aphelion of Mars around the Sun. Conversely, lowest values are found around Mars perihelion at $t_{01} + 0/800$ days. Although the position of Mars seems to be the main driver of Δr, the initial position of the Earth (which has an orbital eccentricity much lower than Mars) and the location of the ballistic capture state targeted with respect to the planet will introduce significant variations. There does not seem to be a relation between this parameter and the fuel consumption when compared with Fig. 10.1.

Finally, Fig. 10.4 shows the ballistic time of flight of the transfer, $t_0 - t_f$. As could be expected, transfers close to the feasibility limits have very small ballistic TOF's, since the transfer is very close to a time-optimal one and the thrust control is active for the most part of the trajectory. In general, the ballistic TOF is quite small, and the spacecraft is performing a transfer that is almost a rendez-vous with the planet, not spending much time flying ballistically along the capture trajectory.

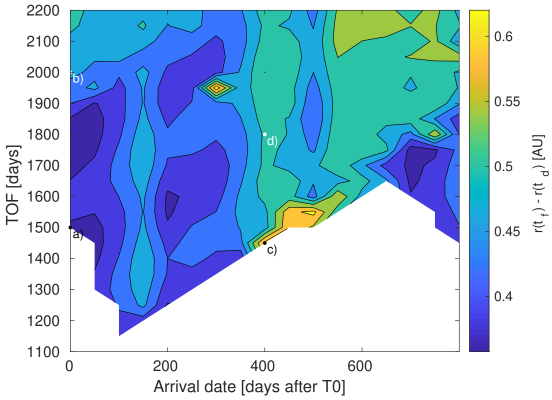

Figure 10.3: $\Delta r = r(t_f) - r(t_d)$ for fuel-optimal heliocentric transfers to ballistic capture at Mars, as a function of the arrival date and the total time of flight.

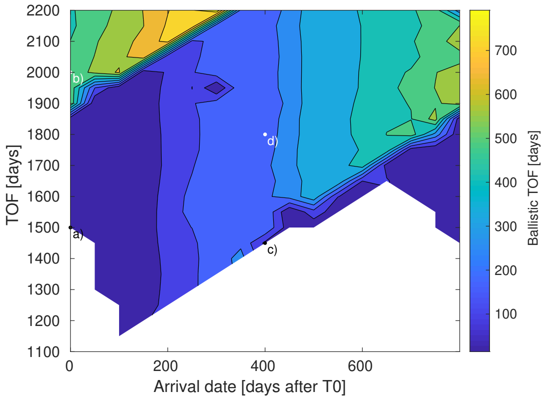

Figure 10.4: Ballistic time of flight for fuel-optimal heliocentric transfers to ballistic capture at Mars, as a function of the arrival date and the total time of flight.

Figs. 10.1 to 10.4 show four labeled points (a), (b), (c) and (d) which correspond to pairs $\{t_0 - t_{01}, \mathrm{TOF}\}$ equal to $\{0, 1500\}$, $\{0, 2000\}$, $\{400, 1450\}$ and $\{400, 1800\}$, respectively. Fig. 10.5 shows the optimized trajectories of these data points. As expected, for longer time of flights the spacecraft spends a very important part of the trajectory coasting with the thrusters off. It is also interesting to see the last ballistic stage in yellow before reaching Mars. Orbits (a) and (c) travel only briefly along the ballistic capture while trajectories (b) and (d) turn off their engines long before reaching the vicinity of Mars. Fig. 10.6 shows the control history of these transfers until the point where they turn off their engines.

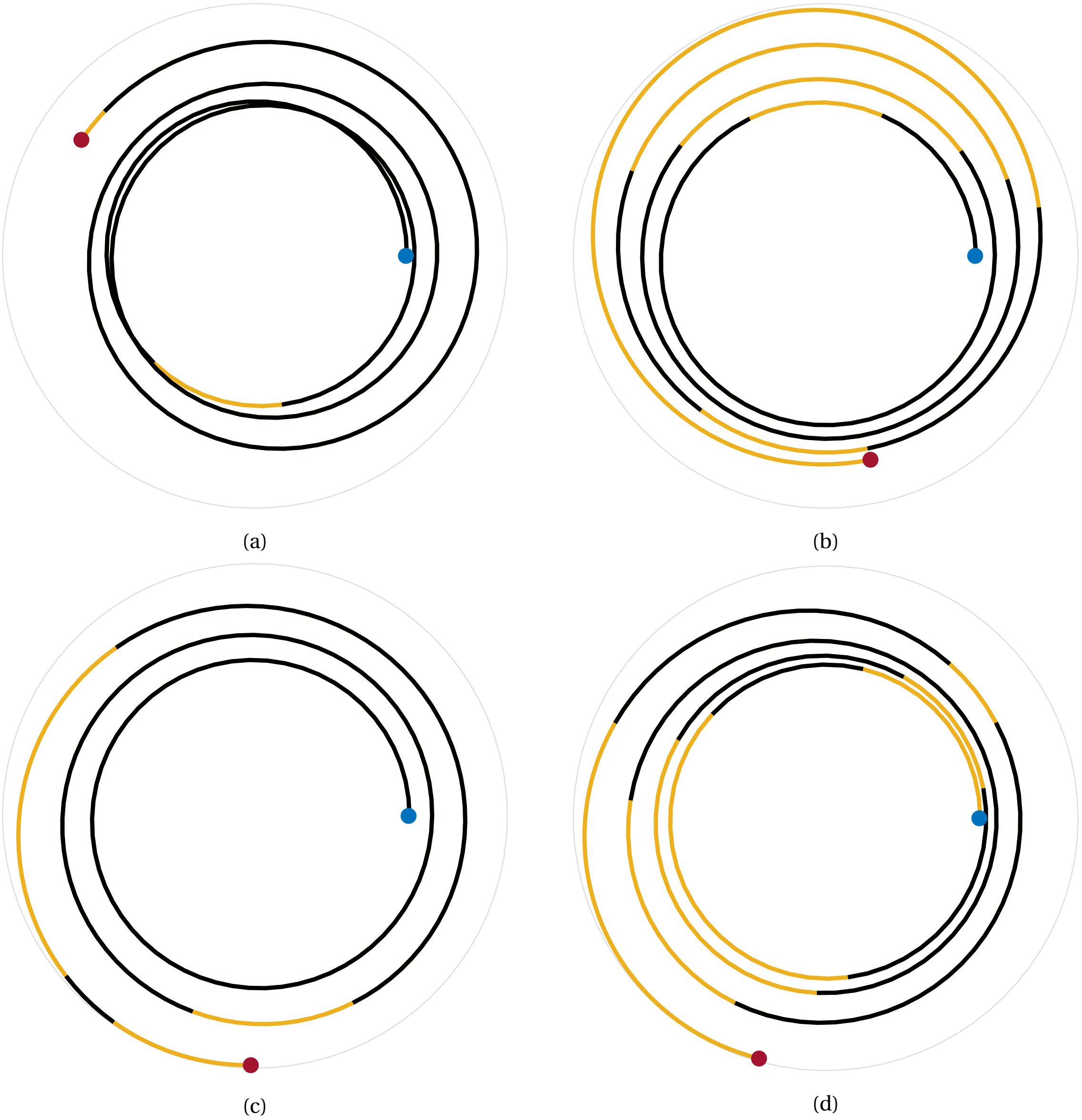

Figure 10.5: Examples of fuel-optimal heliocentric transfers to ballistic captures at Mars, corresponding to the labeled points in Figs. 10.1 to 10.4. The blue and red circles represent the initial position of the Earth and the final position of Mars, respectively. The trajectory is colored black or yellow if the low-thrust control is on or off, respectively.

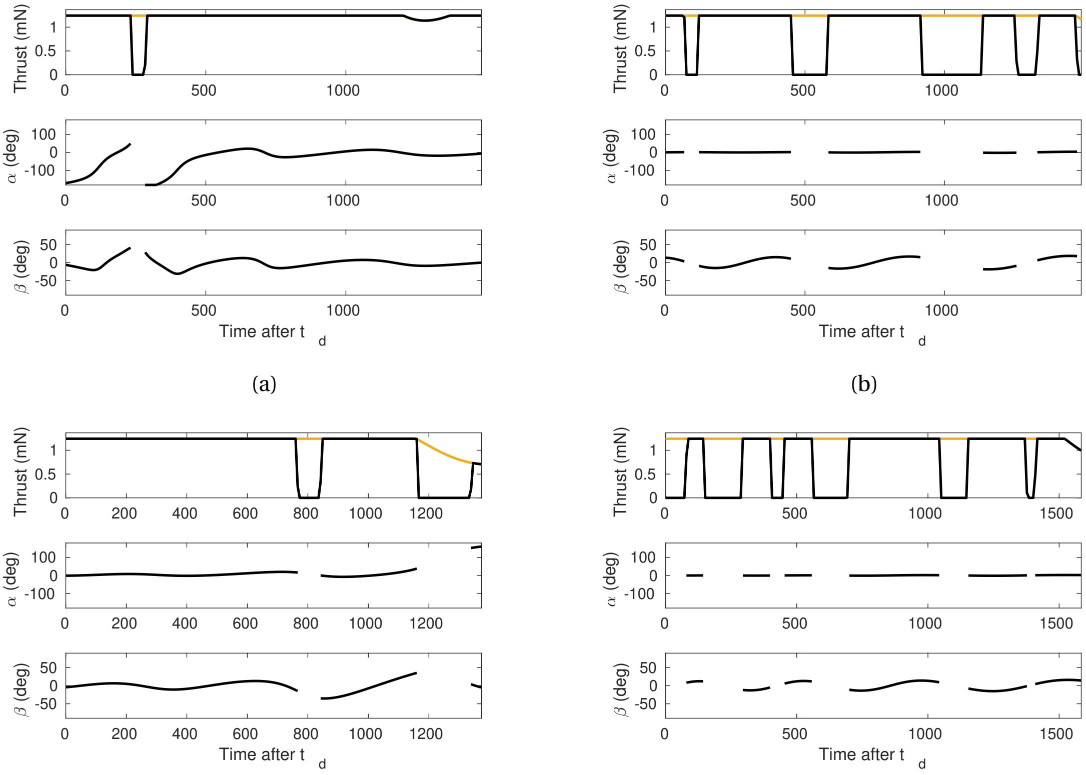

(a)

(b)

(c)

(d)

Figure 10.6: Control history of the fuel-optimal heliocentric transfers shown in Fig. 10.5. The history of the thrust level and thrust angles is shown. The yellow line marks the maximum available thrust.

10.4. REAL SOLAR SYSTEM DYNAMICS

All simulations in this Chapter so far have employed two-body dynamics. As said in Section 9.4, employing more advanced dynamical models in this stage of the mission is a priori not as important because the engine thrust is always going to be the main driver of the trajectory. However, it is interesting to see the effect of using a more complex model, in this case an RnBP ephemeris model including all the planets of the Solar System and Solar Radiation Pressure (SRP). The transfer labeled (d) in Section 10.3, that is, the one with arrival epoch t_{01}+400 days (12/Jun/2025) and time of flight of 1800 days, will be refined with these more complex dynamics.

Fig. 10.7 shows the trajectory and control history of this transfer when using the ephemeris model mentioned. The control is similar but a bit different from that on Fig. 10.5d). The fuel mass required is also slightly larger than for the case with only two-body dynamics, of 4.37 kg instead of 4.31 kg, or a 1.4% more. The optimization of this transfer took however several hours when using the ephemeris model as opposed to a few minutes when using two-body dynamics. For that reason, and because the differences are as shown above are relatively small, the two-body model is deemed sufficient for this early stage of the mission design.

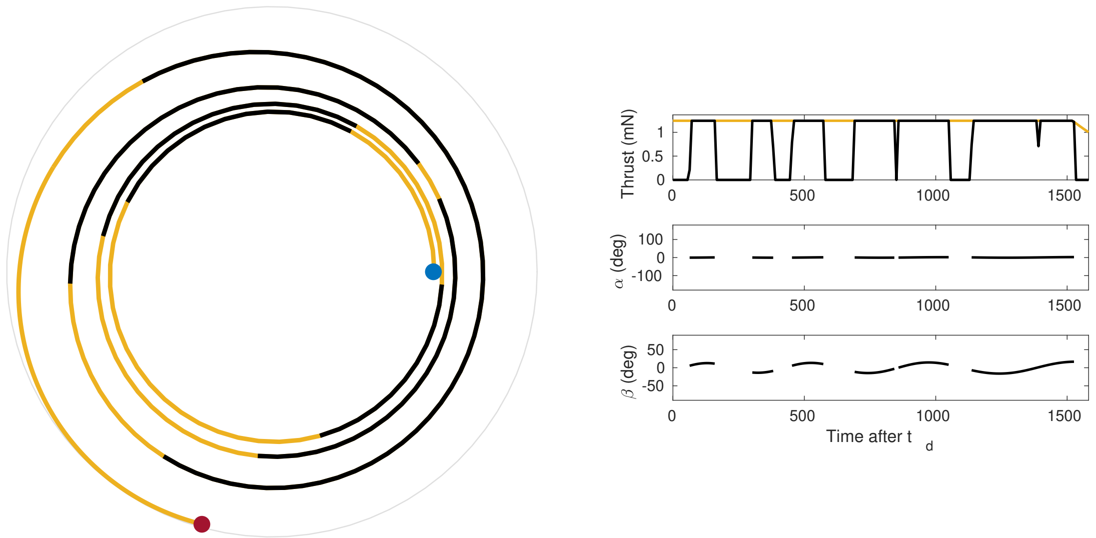

Figure 10.7: Heliocentric transfer to a ballistic capture at Mars, for arrival epoch t_{01} + 400 days and time of flight of 1400 days, studied with an ephemeris model with gravitational perturbation of all bodies in the solar system and SRP. The blue and red circles represent the initial position of the Earth and the final position of Mars, respectively. The trajectory is colored black or yellow if the low-thrust control is on or off, respectively.

10.5. EFFECT OF THE HYPERBOLIC EXCESS VELOCITY AT EARTH

The excess velocity the spacecraft leaves the SOI with can have a very important effect on the heliocentric transfer towards Mars. An in-depth trade-off between the use of high-thrust propulsion around Earth and low-thrust propulsion in deep space will not be conducted, but a more aggressive escape strategy from Earth that leads to a larger v_∞ can make the transfer faster and cheaper in terms of low-thrust fuel consumption.

All simulations in this Chapter so far have considered an excess velocity of v_∞ = 100 m/s. Here, the case with arrival epoch t_{01} + 400 days and time of flight of 1450 days, labeled (c) in the previous Sections, will be studied for other values of the excess velocity, both lower and higher. Figs. 10.8 and 10.9 show the trajectory and control history of transfers for this pair of arrival date and time of flight with different values of excess velocity, namely 0, 300 and 1,000 meters per second. The nominal value is also included for reference.

As expected, the fuel consumption decreases significantly as the initial excess velocity is increased. It can also be seen how the coasting phases when the spacecraft is not using its engine become longer as the initial velocity is increased. It should be noted that when v_∞ is increased, times of flight that were not feasible before now become so, extending the region of feasibility of the transfers and enabling faster transfers to Mars.

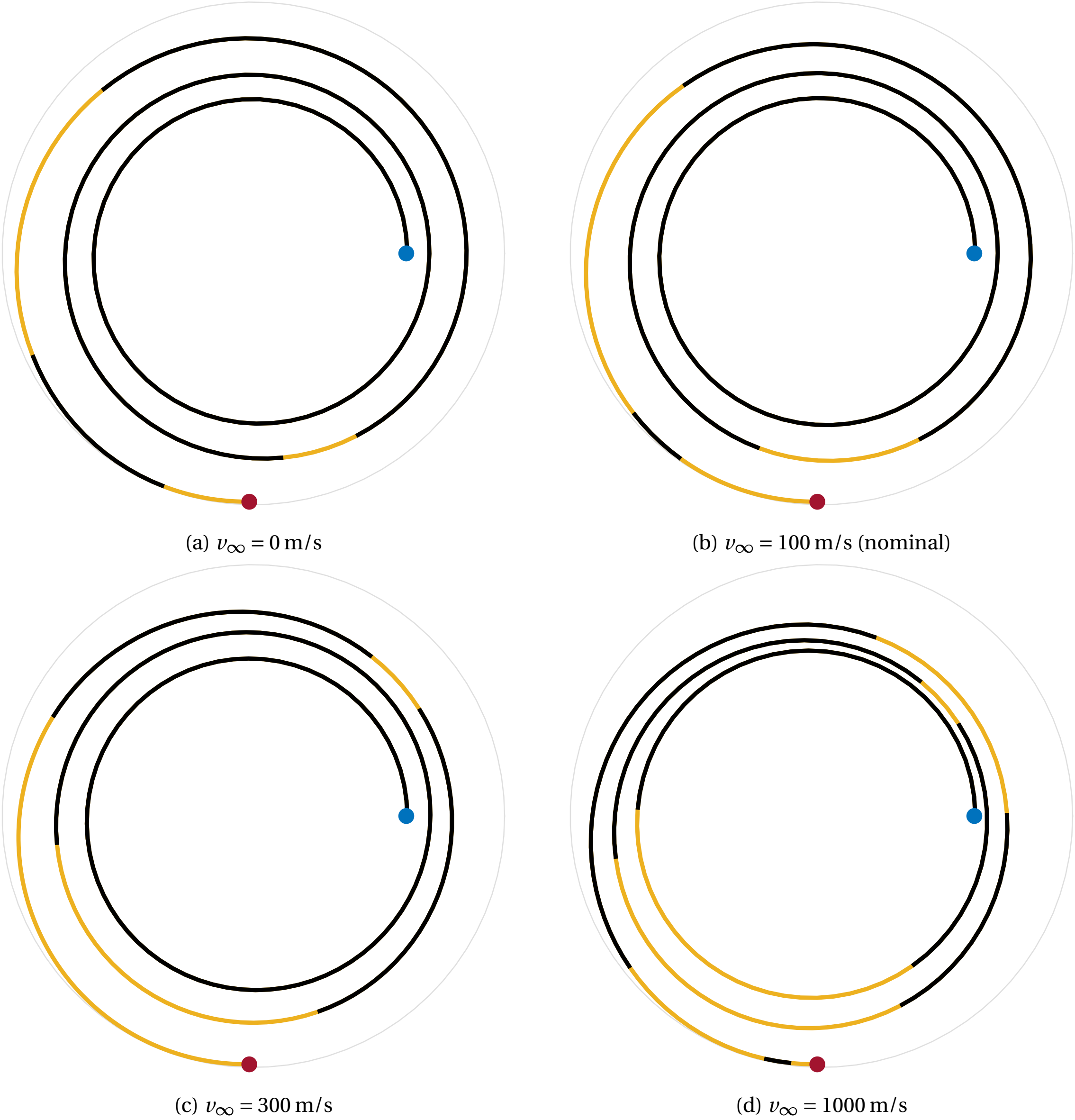
(a) $v_\infty = 0\,\mathrm{m/s}$

(b) $v_\infty = 100\,\mathrm{m/s}$ (nominal)

(c) $v_\infty = 300\,\mathrm{m/s}$

(d) $v_\infty = 1000\,\mathrm{m/s}$

Figure 10.8: Examples of fuel-optimal heliocentric transfers to ballistic captures at Mars, for arrival epoch $t_{01} + 400$ days and time of flight of 1400 days, and with larger excess velocities at the SOI of the Earth. The blue and red circles represent the initial position of the Earth and the final position of Mars, respectively. The trajectory is colored black or yellow if the low-thrust control is on or off, respectively.

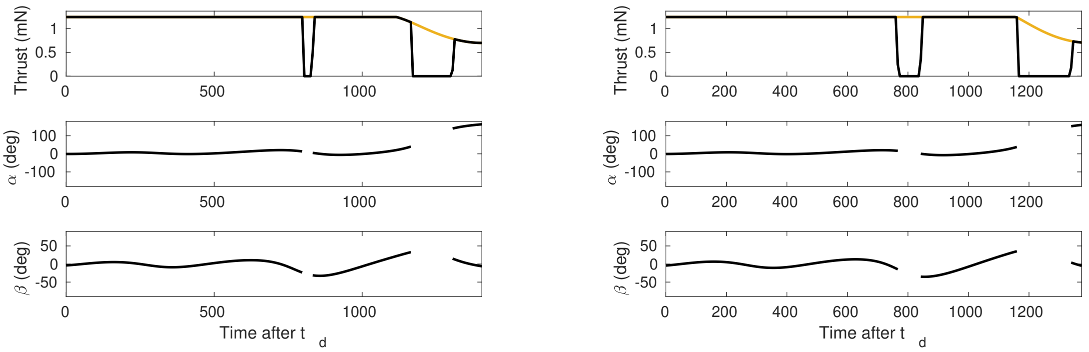

(a) $v_\infty = 0\,\mathrm{m/s}$

(b) $v_\infty = 100\,\mathrm{m/s}$ (nominal)

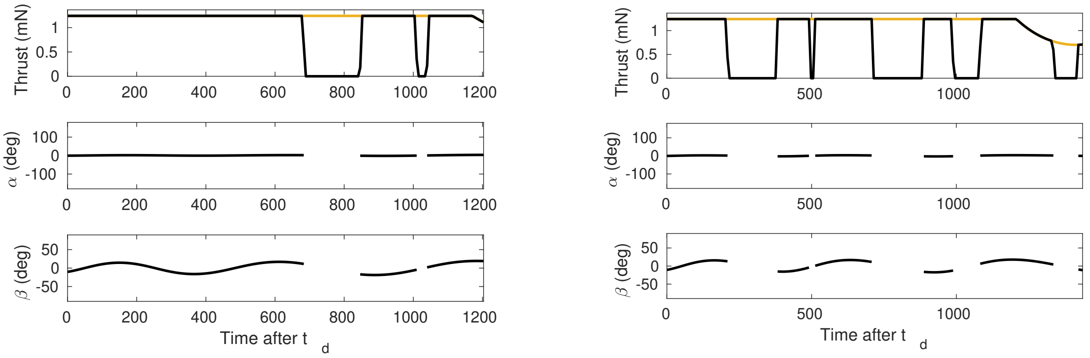

(c) $v_\infty = 300\,\mathrm{m/s}$

(d) $v_\infty = 1000\,\mathrm{m/s}$

Figure 10.9: Control history of the fuel-optimal heliocentric transfers shown in Fig. 10.8. The history of the thrust level and thrust angles is shown. The yellow line marks the maximum available thrust.

Table 10.2: Fuel consumption and transfer time of heliocentric transfers with arrival epoch $t_{01} + 400$ days and time of flight of 1450 days, for different values of the excess velocity at the SOI of the Earth.

Excess velocity [m/s]	Fuel consumption [kg]	Transfer time [days]
0 m/s	5.109 kg	1404.38 days
100 m/s	4.630 kg	1373.84 days
300 m/s	4.165 kg	1203.08 days
1000 m/s	3.740 kg	1436.35 days

VII

CONCLUSIONS AND RECOMMENDATIONS

11

CONCLUSIONS AND RECOMMENDATIONS

11.1. CONCLUSIONS

All the previous Chapters have described in detail the different stages of the trajectory of an interplanetary mission from an Earth-bound orbit to a stable science orbit around Mars. The escape from Earth using high-thrust propulsion was studied in Part IV. There it was established that gravity losses are small when dividing the escape maneuver into several finite burns around perigee. Even when this number of burns is small (e.g. 7 burns of 1,000 seconds each), the gravity losses are only about 2.4%. Using the bi-propellant thruster described in that Chapter, the propellant consumption to reach the Sphere of Influence (SOI) of the Earth with an excess velocity of v_∞ = 100 m/s is approximately 6.7 kg, and the time of flight will be around one month. This phase of the mission employs a very significant amount of propellant but is relatively quick, given the characteristics of chemical propulsion. This is necessary because of the importance of avoiding long stays in the vicinity of the Earth where passages through the Van Allen belts can harm the spacecraft due to radiation.

Before studying the deep-space cruise from Earth to Mars, the trajectory of the spacecraft in the vicinity of the Red Planet was studied first. In particular, ballistic capture sets were constructed for a range of epochs in Part III. The grid of initial conditions was selected such that they were contained in the equatorial plane of Mars, what should a priori make the stabilization into an areostationary orbit easier. The evolution of the capture sets for the different epochs, and of some parameters describing them, was also studied. Results from previous literature, such as the dependence of the capture ratio and stability index on the position of Mars in its eccentric orbit around the Sun, were confirmed.

Once hundreds of capture trajectories were obtained for each epoch, all of them were stabilized into an areostationary orbit. First, a brief high-thrust burn at the first periapsis at Mars stabilizes the orbit and decreases slightly its very high eccentricity. Then, a low-thrust control employing a so-called Q-Law control law is used to target the semi-major axis, eccentricity and inclination of an areostationary orbit. For each epoch, the capture from the set that offers a lower total time of flight is selected. This TOF includes the ballistic capture trajectory from the first entrance into the SOI of Mars until the first periapsis and then the time required by the control law to stabilize the spacecraft's orbit. Although the results vary for the different epochs, the fastest capture usually requires from 300 to approximately 420 days to achieve stabilization, and a fuel consumption between 320 and 460 grams. This does not include the approximately 280 grams of chemical propellant used in the first periapsis burn. It should be noted that the initial mass at the beginning of this stage was estimated to be 21 kilograms. This figure is actually an over estimation after the results obtained in Chapters 6 and 10 for the escape and heliocentric stages respectively. A more accurate figure could be 19 kilograms. The parametric study conducted in Section 8.5 shows that this change could shave off around 50 days and a corresponding 70 grams of propellant in the stabilization of the capture. The values obtained can therefore be considered conservative.

The capture that offers a faster stabilization was then targeted from Earth with a low-thrust heliocentric transfer in Part VI. A grid on arrival date and time of flight is constructed with fuel-optimal transfers targeting the splines that define the capture state at Mars. The fuel mass required by the transfer is almost constant regardless of the departure and arrival dates, and approximately equal to 4.2 kilograms. This is not true when the spacecraft performs a fast transfer close to the time-optimal trajectory. In those cases, the fuel consumption can rise up to 6.2 kilograms. The minimum TOF for the transfer depends on the arrival date and the relative positioning of the Earth and Mars. During the whole synodic period studied, the fastest transfer found had a TOF of 1,200 days. As explored in Section 10.5, following a more aggressive escape from Earth that reaches a larger hyperbolic velocity at the SOI can lead to faster hyperbolic transfers. In general, the heliocentric transfers end up targeting the capture state very close to Mars, especially for transfers with small times of flight. For that reason, the problem does not deviate much from a traditional rendez-vous with the planet, and the characteristics of the transfer will be similar.

This means that, when compared with a traditional mission design that could lead to a fly-by around Mars, the proposed approach can offer extra revolutions around the planet at a zero or very small cost. A mission that does not consider regularization into a stable orbit can benefit of staying in the vicinity of Mars for several long revolutions, and a mission leading into a stable science orbit can have the safety net of staying bounded to the planet in case problems with the stabilization arise. Besides, and as shown above, the cost of stabilizing the orbit in terms of fuel consumption are relatively small when compared with the escape from Earth or the heliocentric transfer.

Although the characteristics of the transfer will indeed depend on the departure and arrival date, as well as the selection of specific transfer characteristics (particularly for the escape and heliocentric phases), a general estimation of the total time of flight and fuel mass required for the complete mission is shown in Table 11.1. The time of flight has in general been considered the main driver of the mission design, because the small size of a CubeSat and the over-the-counter components typically used make it particularly susceptible to radiation damage and other harsh conditions of outer space. In that sense, missions will be at least four years long for the problem statement considered in this analysis. Again, a more efficient engine or a more aggressive high-thrust escape strategy could decrease this total mission duration.

On the other hand, the fuel required will be around 7 and 5 kilograms for the high-thrust and low-thrust engines, respectively. Considering the initial mass of the spacecraft is estimated to be 30 kilograms (including safety margins), the amount of fuel required is very significant as could be expected but a priori feasible for a CubeSat design.

In any case, the present document aimed to describe in a high-level, early mission design stage point of view, the characteristics and feasibility of an end-to-end mission from an Earth-bound orbit to a stable science orbit around Mars, using ballistic capture and dual chemical-electric propulsion. It has been shown how targeting a ballistic capture state can provide more flexibility to the mission and enable a relatively inexpensive

Table 11.1: Summary of the time of flight and propellant consumption for each stage of the mission, as described and estimated throughout this report.

Mission phase	Time of flight	Fuel Mass
Escape from Earth	1-3 months	6.6 - 7.7 kg (HT)
Heliocentric transfer	40-60 months	4.2 - 6 kg (LT)
Ballistic capture[1]	2-3 weeks	None
Stabilization at Mars	10-14 months	600 - 740 g (280 HT, 320-480 LT)
TOTAL	52 - 78 months 4.3 - 6.5 years	**High thrust:** 6.9 - 8 kg **Low thrust:** 4.5 - 6.5 kg

opportunity for stabilization into a science orbit around the Red Planet.

11.2. RECOMMENDATIONS

The present Section will aim to offer suggestions for further analysis and study of the topic. Examples of this could be:

- A more detailed study of the capture sets and the influence of the initial conditions (particularly longitude of ascending node and inclination) on the subsequent stabilization into a science orbit.
- The use of a more complex dynamical model or escape strategy specification for the study of the escape from Earth.
- A more in-depth study of the influence of the excess velocity and the conditions of the spacecraft at the SOI of the Earth on the heliocentric transfer towards Mars. This could include targeting a specific escape direction to accommodate the spacecraft for the heliocentric transfer.
- Related to that, a more detailed trade-off between chemical and electric propulsion (in the Earth escape and heliocentric phases, respectively) in order to reach Mars faster and/or cheaper.
- The use of an optimization technique in the stabilization of the captures, similar to what is done for the heliocentric stage, instead of a pre-determined control law like the Q-law employed here.
- The analysis of engine specifications and spacecraft design that could enable a mission design like the one explored in this report. This could also include a study of how a CubeSat could sustain the radiation damage of a long interplanetary mission like this.
- A sanity check of the connection points between the different stages of the mission. This is particularly important given that different dynamical models and centers of integration have been used. Some sort of multiple shooting scheme could be used to guarantee the continuity of the trajectory between the different phases.
- A study of the control required to actually fly the designed trajectory and correct any possible deviations. Again this is very important given the sensitivity of the dynamics particularly in the heavily perturbed ballistic stage. This could also include studying the control necessary to maintain a CubeSat in a stable Mars-centered orbit like an areostationary one.

---

[1] Until high-thrust maneuver at first periapsis at Mars.

- An analysis of what other types of orbits around Mars could be targeted with this approach. Orbits closer to the surface should be harder to reach but their feasibility could still be studied.
- Indeed, the extension of this mission design approach to other interplanetary targets within the Solar System.

BIBLIOGRAPHY

[1] B. Drake, S. J. Hoffman, and D. Beaty, *Human exploration of Mars, Design Reference Architecture 5.0,* in *IEEE Aerospace Conference Proceedings* (2010) pp. 1 – 24.

[2] T. N. Titus, H. H. Kieffer, and P. R. Christensen, *Exposed water ice discovered near the south pole of Mars,* Science **299**, 1048 (2003).

[3] J. Schoolcraft, A. T. Klesh, and T. Werne, *MarCO: Interplanetary Mission Development On a CubeSat Scale,* in *SpaceOps 2016 Conference* (2016).

[4] A. Sanz Casado, *Preliminary Systems Design of a Stand-Alone Interplanetary Cubesat to Mars*, Master's thesis, Politecnico di Milano/Universidad Carlos III de Madrid (2017).

[5] E. A. Belbruno and J. K. Miller, *Sun-perturbed Earth-to-Moon transfers with Ballistic Capture,* Journal of Guidance, Control and Dynamics **16**, 770 (1993).

[6] S. Hatch, M.-K. Chung, J. Kangas, S. Long, R. Roncoli, and T. Sweetser, *Trans-Lunar Cruise Trajectory Design of GRAIL (Gravity Recovery and Interior Laboratory) Mission,* in *AIAA/AAS Astrodynamics Specialist Conference* (2010).

[7] F. Topputo and E. Belbruno, *Earth-Mars Transfers with Ballistic Captures,* Celestial Mechanics and Dynamical Astronomy **121**, 329 (2015).

[8] F. Topputo, M. Vasile, and F. Bernelli-Zazzera, *Low Energy Interplanetary Transfers Exploiting Invariant Manifolds of the Restricted Three-Body Problem,* Journal of the Astronautical Sciences **53**, 353 (2005).

[9] P. Moral, S. Centuori, and M. Sanjurjo-Rivo, *Ballistic Captures and Transfer Opportunities for a Mission to Mars,* in *68th International Astronautical Congress (IAC)* (2017).

[10] G. Cruz Chambel de Aguiar, *Earth-Mars low-thrust transfers with ballistic capture and real-solar-system dinamics*, Master's thesis, Delft University of Technology (2017).

[11] J. J. Silva and P. Romero, *Optimal longitudes determination for the station keeping of areostationary satellites,* Planetary and Space Science **87**, 14 (2013).

[12] W. S. Koon, M. W. Lo, J. E. Marsden, and S. D. Ross, *Low Energy Transfer to the Moon,* Celestial Mechanics and Dynamical Astronomy **81**, 63 (2001).

[13] W. S. Koon, M. W. Lo, J. E. Marsden, and S. D. Ross, *Heteroclinic connections between periodic orbits and resonance transitions in celestial mechanics,* Chaos: An Interdisciplinary Journal of Nonlinear Science **10**, 427 (2000).

[14] G. Mingotti, F. Topputo, and F. Bernelli-Zazzera, *Earth–Mars transfers with ballistic escape and low-thrust capture,* Celestial Mechanics and Dynamical Astronomy **110**, 169 (2011).

[15] N. Hyeraci and F. Topputo, *Method to Design Ballistic Capture in the Elliptic Restricted Three-Body Problem,* Journal of Guidance Control Dynamics **33**, 1814 (2010).

[16] E. Belbruno, *Capture Dynamics and Chaotic Motions in Celestial Mechanics*, 1st ed. (Princeton University Press, United Kingdom, 2004).

[17] Z.-F. Luo, F. Topputo, F. Bernelli-Zazzera, and G.-J. Tang, *Constructing ballistic capture orbits in the real Solar System model,* Celestial Mechanics and Dynamical Astronomy **120**, 433 (2014).

[18] C. Circi and P. Teofilatto, *Effect of Planetary Eccentricity on Ballistic Capture in the Solar System,* Celestial Mechanics and Dynamical Astronomy **93**, 69 (2005).

[19] Z.-F. Luo and F. Topputo, *Analysis of ballistic capture in Sun-planet models,* Advances in Space Research **56**, 1030 (2015).

[20] Z. Makó and F. Szenkovits, *Capture in the circular and elliptic restricted three-body problem,* Celestial Mechanics and Dynamical Astronomy **90**, 51 (2004).

[21] Z.-F. Luo and F. Topputo, *Capability of satellite-aided ballistic capture,* Communications in Nonlinear Science and Numerical Simulations **48**, 211 (2017).

[22] H. Visser, *Aircraft Performance Optimization* (TU Delft, Delft, The Netherlands, 2014).

[23] J. T. Betts, *Survey of Numerical Methods for Trajectory Optimization,* Journal of Guidance Control Dynamics **21**, 193 (1998).

[24] A. V. Rao, *A survey of numerical methods for optimal control,* Advances in the Astronautical Sciences **135**, 497 (2009).

[25] F. Topputo and C. Zhang, *Survey of direct transcription for low-thrust space trajectory optimization with applications,* in *Abstract and Applied Analysis*, Vol. 2014 (Hindawi, 2014).

[26] K. F. Wakker, *Fundamentals of Astrodynamics* (TU Delft, Delft, The Netherlands, 2015).

[27] S. Kemble, *Interplanetary Mission Analysis and Design* (Springer, 2006).

[28] M. J. L. Turner, *Rocket and Spacecraft Propulsion: Principles, Practice and New Developments*, 3rd ed. (Springer, 2009).

[29] W. M. Folkner, J. G. Williams, D. H. Boggs, R. S. Park, and P. Kuchynka, *The planetary and lunar ephemerides de430 and de431,* Interplanetary Network Progress Report **196**, 1 (2014).

[30] R. Russell, *Survey of Spacecraft Trajectory Design in Strongly Perturbed Environments,* Journal of Guidance Control Dynamics **35**, 705 (2012).

[31] R. Barrio and S. Serrano, *Performance of perturbation methods on orbit prediction,* Mathematical and Computer Modelling **48**, 594 (2008).

[32] K. Mani, F. Topputo, and A. Cervone, *Chemical Propulsion System Design for a 16U Interplanetary CubeSat,* in *69th International Astronautical Congress (IAC 2018)* (2018) pp. 1–15.

[33] D. A. Vallado, *Fundamentals of Astrodynamics and Applications* (Microcosm Press, 2007).

[34] F. Soler Lanagrán, *Low-Thrust Heliocentric Transfer with Ballistic Capture and Orbit Circularization for a Standalone Mars CubeSat*, Master's thesis, Politecnico di Milano (2018).

[35] A. E. Petropoulos, *Refinements to the Q-law for low-thrust orbit transfers, 15th AAS/AIAA Space Flight Mechanics Conference*, (2005).

[36] J. C. Lagarias, J. A. Reeds, M. H. Wright, and M. H. Wright, *Convergence Properties of the Nelder-Mead Simplex Method in Low Dimensions,* SIAM Journal of Optimization **9**, 112 (1998).

[37] C. L. Ranieri, *Indirect Optimization of Interplanetary Trajectories Including Spiral Dynamics*, Ph.D. thesis, The University of Texas at Austin (2007).